Experimental Study of Liquid Fuel Spray Combustion

Westlye, Fredrik Ree

Publication date:
2016

Document Version
Publisher's PDF, also known as Version of record

Experimental Study of Liquid Fuel Spray Combustion

By

Fredrik Ree Westlye

Ph. D. Thesis

Department of Mechanical Engineering
Technical University of Denmark
DK-2800, Kgs. Lyngby
Denmark

Kgs. Lyngby June 2016

Summary

This PhD dissertation was carried out at the Technical University of Denmark in the Department of Mechanical Engineering and has been supervised by Associate Professor Anders Ivarsson and co-supervised by Professor Jesper Schramm. The project has been a part of the RADIADE project funded by the Danish Council for Strategic Research. Other supporters of the project have been MAN Diesel & Turbo A/S, DTU Mechanical Engineering, DTU Chemical Engineering, Sandia National Laboratories USA, Norwegian University of Science & Technology (NTNU) and University of Nottingham, Malaysia Campus.

The continuing stringency of emission regulations for marine diesel engines forces a deeper understanding of the complex physical processes occurring inside the engine cylinder. A deeper understanding can lead to higher accuracy of predictive numerical models, thereby enabling evaluation of multiple engine design parameter variations which would otherwise be extremely costly and difficult to evaluate experimentally. The aim of this work is to provide a wide range of reliable experimental data of which to validate current Computational Fluid Dynamic models employing complex physics such as evaporation of atomized liquid sprays, turbulent heat and mass transport, reaction kinetics, soot formation and radiant heat transfer. These computational models are to some degree based on true physics, but simplified empirical models are unavoidable. Complex experiments are needed in order to accurately measure the specific physical quantities needed in CFD validation of these types of flames. This work is a testament to that fact.

The first part of this thesis is an extensive study of optical combustion diagnostics applied to complex transient spray flames in a high temperature and pressure environment. The physiochemical properties and electromagnetic interactions in flames, of which various optical combustion diagnostics are based, have been reviewed. Key diagnostics have been presented with practical examples of their application which, together with a comprehensive review of fuel spray flames, form the motivations for the selection of diagnostics to apply in measuring key quantities in complex spray flames. In addition, the extinction imaging technique has been refined to optimize applicability in the optically harsh ambient environments into which the sprays are injected. Well defined back illumination characteristics, dimensioned according to the collection optics, removes artifacts caused by steep gradients in the refractive index while promoting high temporal resolution capabilities.

The second part of this thesis consists of a comprehensive experimental campaign of fuel spray and combustion characteristics from cavitating and non-cavitating large bore injectors. The injectors have been specifically machined to isolate the effects of in-nozzle cavitation on the resulting spray and combusting characteristics. Experiments were carried out in an optically accessible constant volume combustion vessel, generating a controlled ambient environment into which the fuel sprays were injected, achieving a high degree of reproducibility. Measurements of liquid and vapor boundaries, determining key spray characteristics, were made using extinction and schlieren imaging respectively. Flame lift-off, ignition delay and soot volume fraction was measured, determining key combustion characteristics, using OH^* chemiluminescence-, natural flame luminosity- and extinction imaging respectively.

The enhanced spray break-up induced by cavitation does not seem to have a radical effect when the fuel is injected into a high pressure and temperature environment. Rather, the break-up length is shortened such that the spray/jet obtains a fully developed flow closer to the nozzle, consequently shifting the flow and combustion characteristics with it.

Considerations regarding the optical setup, optical elements, corrections for camera non-idealities and post processing methods have been developed and refined in this work to measure the optical thickness of the soot in the transient spray flames as accurately as possible. The soot cloud from these wide bore injectors was so optically thick that it appeared opaque to the camera at higher ambient temperatures. The soot volume fraction could, however, be determined in the initial formation regions up to an optical thickness of around 4, with a higher degree of certainty than prior applications of extinction imaging of soot.

CFD modeled soot fields, showing good agreement with measurements, were translated to optical thickness revealing that these flames can potentially have an optical thickness up to 50 at 635 nm in the later stages of soot formation.

Resumé

Denne ph.d.-afhandling er udført på Danmarks Tekniske Universitet på Institut for Mekanisk Teknologi under vejledning af lektor Anders Ivarsson og med professor Jesper Schramm som medvejleder. Projektet har været en del af RADIADE projektet med finansiering fra det danske Strategiske Forskningsråd. RADIADE projektet er et forskningssamarbejde mellem MAN Diesel & Turbo A/S, DTU Mekanik, DTU Kemiteknik, Sandia National Laboratories (USA), Norges Teknisk-Naturvidenskabelige Universitet (NTNU) og University of Nottingham (Malaysia Campus).

De skærpede emissionskrav for marine dieselmotorer skaber behov for en dybere forståelse af de komplekse fysiske processer i motorens forbrændingskammer. En øget indsigt i processerne vil bidrage til større nøjagtighed af numeriske motormodeller, der muliggør optimering af en motors designparametre, der ellers er ekstremt dyr og vanskelig at foretage eksperimentelt. Målet med dette ph.d.-projekt er at udvide databasen af pålidelige eksperimentelle målinger egnet til validering og kalibrering af CFD modeller med kompleks fysik, såsom forstøvning og fordampning af brændstofspray, turbulent stoftransport, reaktionskinetik, soddannelse og varmestråling. Disse beregningsmodeller er til en hvis grad baseret på grundlæggende fysik, men nødvendige simplifikationer medfører, at en høj grad af empiri ikke kan undværes. Komplicerede laboratorieforsøg er en nødvendighed for nøjagtig bestemmelse af de fysiske værdier, der kræves til kalibrering af relevante CFD modeller. Denne kendsgerning fremgår tydelighed af ph.d.-projekts resultater.

Den første del af afhandlingen er en omfattende undersøgelse af optiske målemetoder til anvendelse i komplekse sprayflammer i omgivelser med høj temperatur og tryk. Der redegøres for flammers fysiske og kemiske egenskaber, samt de elektromagnetiske interaktioner som de optiske målemetoder er baseret på. De vigtigste målemetoder præsenteres med eksempler på praktisk anvendelse, der, sammen med en omfattende gennemgang af de relevante sprayflammer, benyttes til at indsnævre udvalget af egnede målemetoder til de relevante sprayflammer. Derudover er den optiske målemetode kaldet "extinction imaging" blevet videreudviklet, så den er valid under optisk vanskelige betingelser med brændstofspray. Videreudviklingen består i at optimere baggrundslysets karakteristik samt afstemme kameraoptikken derefter. Målemetoden fjerner målefejl forårsaget af stejle gradienter af brydningsindekset gennem spray og sprayflammer samt fremmer høj tidsopløste målinger.

Den anden del af afhandlingen omhandler en omfattende målekampagne på spray og forbrændings egenskaber fra kaviterende og ikke-kaviterende indsprøjtningsdyser. De to dyser er særligt designede med henblik på at isolere virkningerne af kavitation på den resulterende spray og forbrænding. Eksperimenterne blev udført i et konstant volumen forbrændingskammer med optisk adgang. I kammeret skabes et miljø svarende til kompressionsforholdene i en Dieselmotor, men med en høj grad af reproducerbarhed og kontrol, hvori brændstoffet bliver indsprøjtet. Udbredelse af brændstoffets væske- og dampfase er bestemmende for en sprayflammes egenskaber og blev målt for spray uden forbrænding med hhv. "extinction imaging" og "schlieren imaging". For spray med forbrænding blev flammens løftehøjde, tændingsforsinkelse og sodkoncentration, der er afgørende for en dieselmotors drift, målt på hhv. OH^* chemiluminescence, bredspektret flamme stråling og "extinction imaging".

Undersøgelsen viser, at kavitation har en betydelig indflydelse på sprayens break-up zone, men udenfor break-up zonen har kavitation næsten ingen indvirkning under de aktuelle betingelser. Den klare tendens er, at break-up zonens længde forkortes, således at sprayen opnår en fuldt udviklet strømning tættere på dysen. Betragtes udelukkende sprayens strømnings- og forbrændingsegenskaber udenfor break-up zonen er de stort set identiske, men placeringen er forskudt svarende til break-up længdens ændring.

Den optiske opstilling, optiske komponenter, kamerakorrektioner og procedurer for databehandling, altså alle leddene i målekæden til bestemmelse af sods optiske tykkelse i transiente spray flammer, er i særlig grad blevet udviklet eller raffineret med henblik på at øge nøjagtigheden. Sodskyen fra de anvendte dyser var så optisk tyk, at den syntes ugennemtrængelig for lys ved højere gastemperaturer. Sodkoncentrationen kunne dog afbildes med hidtil uset nøjagtighed i de tidlige stadier af soddannelse, hvor sodens optiske tykkelse lå under ca. 4.

En CFD model blev kalibreret for at opnå god overensstemmelse med målinger i de tidlige stadier af soddannelsen. Beregnede sodkoncentrationer blev oversat til optiske tykkelse, der viser, at de aktuelle flammer potentielt kan have en optisk tykkelse på op til 50 ved 635 nm i de sene stadier af soddannelsen.

Table of contents

Nomenclature

T	Temperature, [K]
p	Pressure, [Pa]
V	Volume, [m^3]
R	Gas constant, 8.314 [$J \cdot K^{-1} \cdot mol^{-1}$]
n	Number of molecules, [mol], refractive index [−] or number density, [m^{-3}]
M	Molecular mass, [$kg \cdot mol^{-1}$]
Z	Compressibility factor, [−]
x	Concertation by volume, [−]
t	Time, [s]
m	Mass, [kg]
$\dot{m}$	Mass flow, [$kg \cdot s^{-1}$]
U	Velocity, [$m \cdot s^{-1}$]
μ	Dynamic viscosity, [$kg \cdot s^{-1} \cdot m^{-1}$]
γ	Surface tension, [$N \cdot m$]
d	Diameter, [m]
r	Radius, [m]
S	Spray tip penetration, [m]
c_p	Specific heat capacity constant pressure, [$J \cdot K^{-1}$]
h	Enthalpy, [$J \cdot kg^{-1}$]
h_{fg}	Latent heat of vaporization, [$J \cdot g$]
C_a	Area contraction coefficient, [−]
C_d	Discharge coefficient, [−]
c_0	Speed of light in a vacuum, ~3E8 [$m \cdot s^{-1}$]
c	Speed of light, c_0/n, [$m \cdot s^{-1}$]
h_P	Planck's constant, $6.626E-34$ [$J \cdot s$]
k_B	Boltzmann constant, $1.38E-23$ [$J \cdot K^{-1}$]
ϵ	Emissivity, [−]
κ	Attenuation coefficient, [m^{-1}]
$\tilde{m}$	Complex refractive index, n + ki [−]
L	Optical path length, [m]
σ	Cross-section, [cm^2] or standard deviation, [−]
α_{sa}	Scattering to absorption ration, $\sigma_{sca}^{agg}/\sigma_{abs}^{agg}$, [−]
ω_0	Single scattering albedo, $\sigma_{sca}/\sigma_{ext}$, [−]
K_x	Extinction, absorption or scattering coefficient (soot), [m^{-1}]
k_e	Dimensionless extinction coefficient (soot), [−]
d_p	Primary particle diameter, [nm]
N	Number of monomer particles per aggregate
R_g	Radius of gyration, [nm]
f_v	Soot volume fraction, [ppm]
α	Dispersion exponent, [−]
Φ	Radiant flux, [W]
Ω	Solid angle, [sr]
A	Area, [m^2]
L	Radiance, [$W \cdot m^{-2} \cdot sr^{-1}$]
E	Irradiance, [$W \cdot m^{-2}$]
I	Intensity or radiant intensity, [cnts] or [$W \cdot sr^{-1}$]
λ	Wavelength, [nm]
ν	Wavenumber, [cm^{-1}]
τ	Transmission, [−]

Introduction

As the title depicts, the focus of this thesis regards the combustion of liquid fuel. To the layman, this may sound like a narrow topic of research. To a professional however, this description is extremely broad, merging a wide range of disciplines. When the topic of research has been practiced for almost a century, an extensive foundation of knowledge must be attained in order to familiarize oneself with the state of the art before unexplored aspects of the topic can be identified and pursued. For this reason it is never clear what challenges and revelations will be met along the way. A research study evolves through trial and error and, for a novice researcher, with the researcher's maturity within the field. The end product may then differ radically from what was anticipated from the beginning of the project.

This work has been under the umbrella project RADIADE [1], researching radiation in flames with regards to internal combustion engines. The major part of the experimental work has been carried out in collaboration with Sandia National Laboratories and the experimental campaign has been part of the Engine Combustion Network [2].

The continuing stringency of emission regulations for marine diesel engines forces a deeper understanding of the complex physical processes occurring inside the engine cylinder. A deeper understanding can lead to higher accuracy of predictive numerical models, thereby enabling evaluation of multiple engine design parameter variations which would otherwise be extremely costly and difficult to evaluate experimentally. The aim of RADIADE is to enhance the computational capabilities of current Computational Fluid Dynamic models with regards radiant heat transfer. Models involving spray combustion need to accurately predict the fuel spray characteristics in addition to reaction kinetics and radiation models. These computational models are based on true physics and empirical data and are validated against experimental data. Complex experimental design is needed in order to accurately measure specific physical quantities used in CFD validation of these types of flames.

The engine combustion network, or ECN as it is commonly referred to in the community, is a framework for international collaboration between experimentalists and computational modelers within the research field of engine combustion research. A major part of this work has been in collaboration with Sandia National Laboratories focusing on experimental investigation of liquid fuel sprays. The work has been a part of ECN and entailed development of an optical diagnostic for extinction imaging and measurements of fuel sprays with the aim of isolating the effect of in-nozzle cavitation. The experimental facilities at Sandia National Laboratories have been used in the majority of the experimental work and the publications have been in collaboration with Sandia.

To generate fuel spray flames resembling the combustion event occurring in a Diesel engine, the extreme in-cylinder environments need to be reproduced. This is often done in a constant volume combustion vessel able to generate controlled boundary conditions for the combustion event with a high degree of reproducibility.

Sophisticated optical measurement techniques have been increasingly applied in flame diagnostics over the recent years. These methods have the advantage of being non-intrusive to the flame and are able to achieve high temporal and spatial resolution. These methods rely on complex physiochemical flame properties and physical interactions between specific components within the flame and electromagnetic radiation. Extensive knowledge of these processes is required of the experimentalist in order to interpret results and to identify the limitations and uncertainties of the various experimental techniques.

The thesis is outlined such that a foundation of flame physics relevant to the functionality of key optical combustion diagnostic techniques is built, both theoretically and applied. A thorough review of spray type flames completes the foundation aimed at giving the reader insight into the choice of experimental methods and interpretation of experimental data. From here the description of the extensive experimental campaign conducted in this work begins. Details of optical arrangements, processing procedures and the interpretation of the results complete this work.

Physics of radiation and absorption

The topic of radiation has been studied for centuries within a range of applications. Vast amounts of information can be deducted from spectral emission and absorption of radiation and was in the early years mostly used by astronomers and astrophysicists. It isn't until later year (past few decades) where radiation has been applied to heat transfer applications [3]. Radiation from flames consists of radiation from gases and soot particles. To quantify radiative heat transfer in flames, knowledge of temperature, gaseous species and soot concentrations are needed. Extensive knowledge of the physics involved is required to be able to measure and model these quantities. The following serves as a short review/introduction to the physics which models and sophisticated measurement techniques are based upon.

Radiation and absorption of a Black body

A black body is an idealized physical body that is a perfect absorber and perfect emitter. A perfect absorber absorbs all wavelengths of radiation and a perfect emitter emits as much or more energy at all wavelengths than any other body. Radiation is emitted isotropically in all directions and depends solely on the temperature of the body according to Planck's law. The wavelength of maximum Planck radiation shifts toward shorter wavelengths at higher temperatures according to Wien's displacement law. The total radiant flux also increases with temperature according to Stefan-Boltzmann's law. This can be seen in Figure 1 along with the equations.

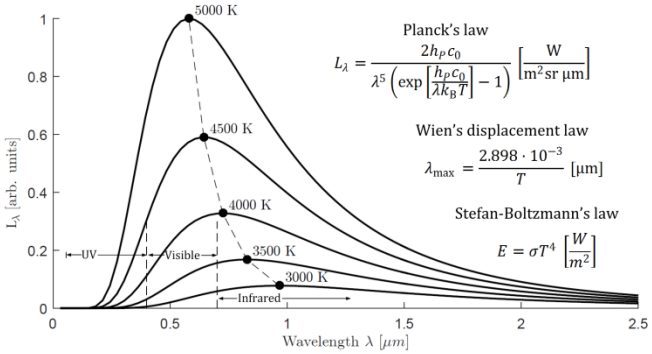

Figure 1: *Black body spectral radiance according to Planck's law at different temperatures. The wavelength of maximum radiance follows Wien's displacement law is indicated by the dots. The total irradiance follows Stefan-Boltzmann's law.*

The emissivity of a body can be thought of as the efficiency at which the body emits thermal radiation relative to a black body at the same temperature. A black body has then an emissivity equal to 1 at all wavelengths. Bodies whose emissivity is constant at all wavelengths but lower than one are referred to as gray bodies.

The sun is considered to be an approximate ideal black body emitter. The effective temperature of the sun can be approximated by Planck's law and has been determined to be roughly 5800 K. At this temperature the black body emission peaks at around the yellow-green part of the visible spectrum at 500 nm. The extraterrestrial solar radiation and the solar radiation observed through 1.5 air mass atmosphere can be seen in Figure 2 together with Planck radiation at 5777 K.

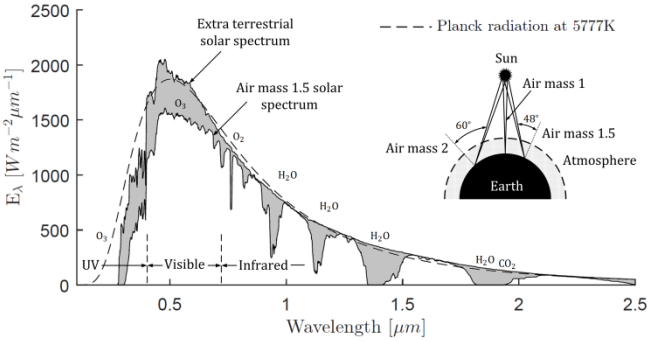

Figure 2: *Extraterrestrial solar radiation and the solar radiation observed on the surface of the earth through 1.5 air mass of atmosphere. Where the shaded regions show the radiation absorbed by various molecules suspended in the earth's atmosphere.* [4]. *Planck radiation at the approximate temperature of the sun is shown as a dashed line.*

The absorption of solar radiation by various molecules in the earth's atmosphere is indicated in Figure 2 which is important for environmental scientists. It can be seen that ozone is responsible for absorbing a large portion of the ultraviolet radiation emitted from the sun and that H_2O is the major absorber in the infrared. Soot is also considered to be an approximate blackbody. The visible yellow-red glow of a flame is heated soot particles emitting broad band black body radiation. Soot is therefore an important environmental pollutant for its broad absorbing properties. Soot suspended in the atmosphere can reduce cloud cover by heating of the environment. Also of concern is soot deposited on snow which lowers the reflectivity leading to rapid melting [5]. The opening of the northern sea route and north-west passage shipping routes have due to the melting of ice in the arctic is cause for great concern. Heavy ship traffic will cause significant increase of soot deposits on the ice, thereby significantly accelerating the melting of the arctic ice [6].

Radiation and absorption in gases

Interactions between molecular gases and electromagnetic radiation can have one of two outcomes. 1) Radiation can be absorbed, thereby altering the energetic state of the molecule or 2) radiation can be scattered, altering the direction of the incoming radiation. Absorption of radiation by a molecule results in a transition of the rotational, vibrational and/or electronic energy levels of the molecule. As illustrated in Figure 3, the rotational transitions require a relatively small amount of energy, giving rise to absorption/emission lines in the microwave range of the electromagnetic spectrum. Vibrational transitions require an intermediate amount of energy and reside therefore in the infrared, while electronic transitions require a large amount of energy with emission/absorption lines in the UV extending to the visible.

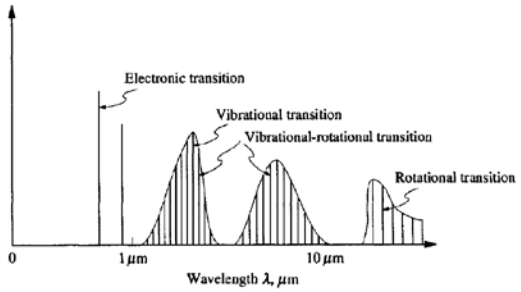

Figure 3: *Illustration of the designated spectral ranges of electronic, vibrational and rotational transitions in molecular gases. Taken from* **[3]**.

The Morse curves illustrated in Figure 4 show the discrete energy levels of the various transitions and indicate the minimum and maximum allowable intermolecular distance for any vibrational energy state. When vibrational energy becomes too high the molecule may dissociate.

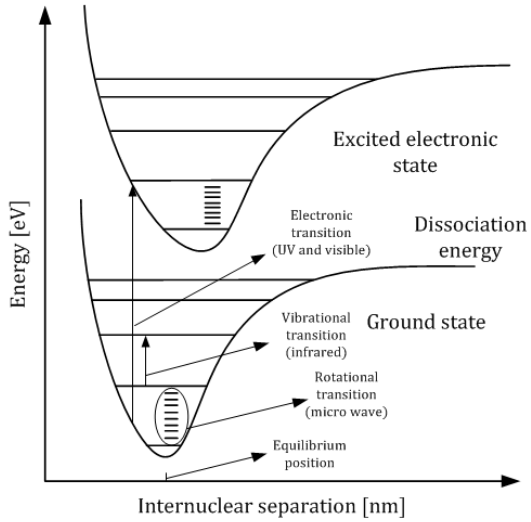

Figure 4: *Potential energy of a diatomic molecule as function of internuclear distance. Rotational, vibrational and electronic transitions are indicated along with their spectral location.*

Quantum mechanics states that these transitions occur at finite discrete wavelengths depicted by the atomic composition of the molecule. The wavelengths at which these transitions occur can be determined by using "rigid-rotor" and "harmonic-oscillator" models for rotational and vibrational transitions respectively. These are very simplified models but can calculate the wavelengths, or spectral lines, which are absorbed by the molecule to some degree of accuracy. Other more complicated models do exist [7,8]. The spectral emission/absorption lines are never purely monochromatic in reality and occur over small finite spectral range with a maximum at the wavelength derived by quantum mechanics. This is caused by different line broadening effects. "Natural broadening" occurs due to a distribution in the energy transition as no energy transition can occur with precisely the same amount of energy according to the Heisenberg uncertainty principle. "Collision broadening" is caused by molecular collisions as the name dictates. These two broadening mechanisms induce a Lorentzian line shape defined by Eq. (1).

$$\ell_{\mathrm{L}}(\nu) = \frac{b_{\mathrm{L}}}{\pi}\frac{1}{(\nu-\nu_0)^2+b_{\mathrm{L}}^2} \tag{1}$$

Where ν_0 is the line center wavelength and $\mathrm{b_L} = \frac{\mathrm{FWHM}}{2}$. The collision broadening of the line is determined from kinetic theory Eq. (2)

$$b_{\mathrm{C}} = b_{\mathrm{C0}}\frac{p}{p_0}\sqrt{\frac{T_0}{T}} \tag{2}$$

Where the 0 subscript denotes reference conditions. "Doppler broadening" is caused by the Doppler effect where a perceived wave of electromagnetic radiation may appear longer or shorter depending on relative movement between emitter and observer. This broadening effect induces a Gaussian line shape defined by Eq. (3).

$$\ell(\nu) = \frac{1}{b_{\mathrm{D}}\sqrt{\pi}}exp\left[-\left(\frac{\nu-\nu_0}{b_{\mathrm{D}}}\right)^2\right] \tag{3}$$

Where $\mathrm{b_D} = \frac{\mathrm{FWHM}}{2}$ as before and is defined by Eq. (4).

$$b_{\mathrm{D}} = \frac{\nu_0}{c_0}\sqrt{\frac{2k_{\mathrm{B}}T}{M}} \tag{4}$$

It can be seen that the collision broadening effects are proportional to $\frac{\mathrm{p}}{\sqrt{\mathrm{T}}}$ and Doppler broadening effects proportional to $\nu\sqrt{\mathrm{T}}$. In most cases collision broadening is the dominant broadening mechanism.
The strength of the absorption lines depend on the transition probability and the population of molecules in the lower energy state. As the line strength depends on the population of states, it is temperature dependent. The Boltzmann distribution of states can be used to determine the fraction of molecules populating discrete energetic states.

$$\frac{n_i}{n} = \frac{h_P c_0 B}{k_{\mathrm{B}}T}(2J+1)\exp\left[\frac{-BJ(J+1)h_{\mathrm{p}}c_0}{kT}\right] \tag{5}$$

Where n_i/n is the fraction of molecules in the discrete rotational energy state, J is the rotation quantum number and B is the rotational constant. An example of an arbitrary molecule's distribution as function of temperature can be seen in Figure 5.

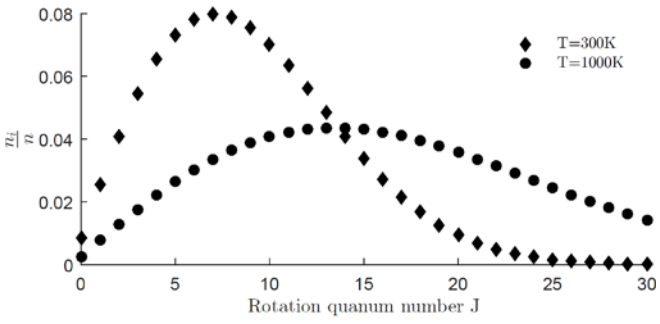

Figure 5: *Boltzmann distribution of an arbitrary molecule at different temperatures.*

As temperature increases, the population is distributed over a wider range of rotational states. Higher rotational energy states are populated at higher temperatures meaning that rotational absorption lines close to the band origin become weaker while the rotational lines further away from the band origin become more important.

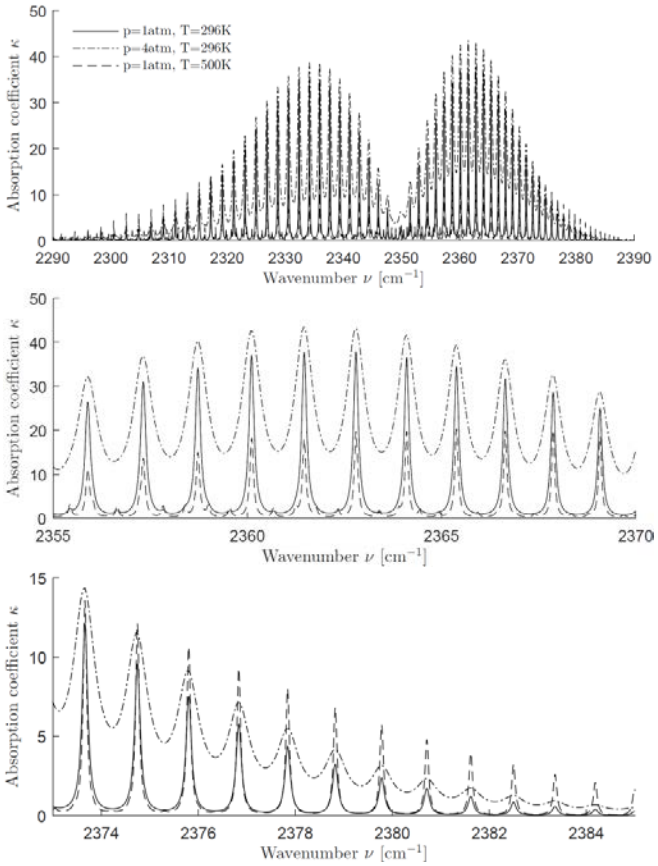

Figure 6: *Spectra of the full* 4.3 μm *band for CO_2 generated from HITEMP* [9] *(above). Zoom in of the R branch (middle). Zoom in of outer rotational lines (below).*

This can be seen in Figure 6 (middle) where the rotation lines at higher temperature are weaker close to the band origin and become higher further away from the band origin (below). Also seen is the "hot lines" appearing in between the rotational lines. "Hot lines" are sub-bands generated at high vibrational energies (high temperature). The pressure broadening effect is apparent causing the rotation lines to overlap.

The emissivity is defined as the ratio between the spectral radiance of a source and the spectral radiance of a black body at the same temperature. For gases at thermodynamic equilibrium, Kirchhoff's law of thermal radiation states that the emissivity is equal to the absorptivity of the gas. From this it becomes evident that the total emissivity then increases with pressure and decreases with temperature. The increase is solely a consequence of the collision broadening of the spectral lines and the decrease due to the broader population in the rotational energy states [10]. This can be seen in Figure 7.

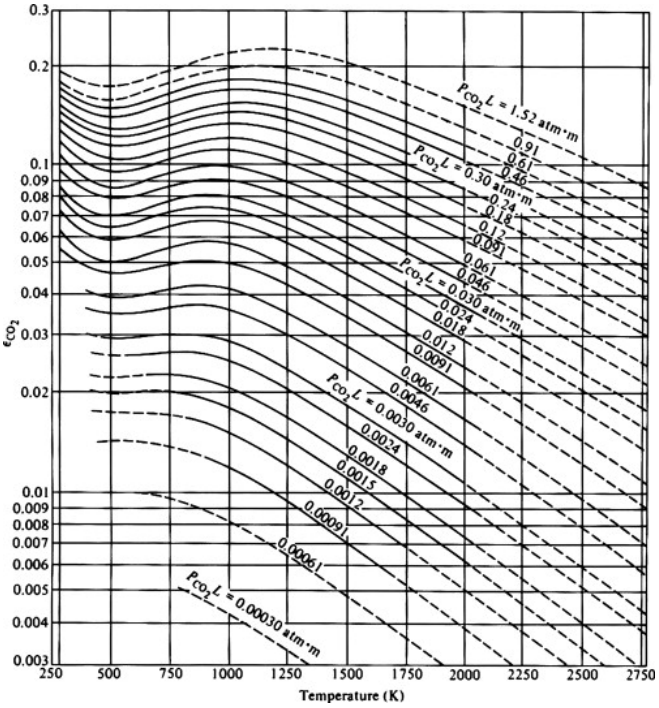

Figure 7: *Total emissivity of CO_2 at total gas pressure of 1 bar and 0 partial pressure, from Hottel and Sarofim* [10].

The well-known Beer-Lambert law states that the absorption of electromagnetic radiation by molecular gas follows the relation in Eq. (6).

$$\tau_\lambda = \frac{\Phi_\lambda}{\Phi_{0,\lambda}} = \exp(-\kappa_{\mathrm{abs},\lambda} L) \tag{6}$$

Where τ_λ is the spectral transmission of electromagnetic radiation through the probed media and $\kappa_{\mathrm{abs},\lambda}$ is the spectral absorption coefficient which is wavelength and species specific. For a system in thermodynamic equilibrium $\kappa_{abs,\lambda} = \epsilon_\lambda$. The absorption coefficient for an ideal gas is related to the absorption cross-section through Eq. (7).

$$\sigma_{\mathrm{abs},\lambda} = \kappa_{\mathrm{abs},\lambda} \frac{T k_{\mathrm{B}}}{x_i p} \tag{7}$$

Where i denotes the i^{th} species.

Turbid media

When electromagnetic radiation passes through a turbid, or particulate laden, media it is simultaneously absorbed and scattered. Scattering is the combined effects of reflection, refraction and diffraction. These interactions are illustrated in Figure 8.

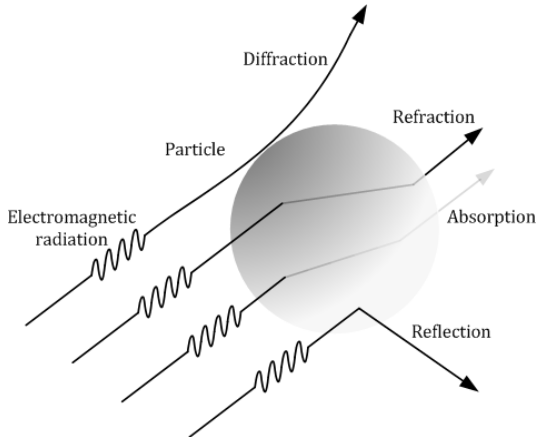

Figure 8: *Illustration of scattering and absorption interactions between particle and electromagnetic radiation.*

These interactions attenuate the light according to the well-known Beer-Lambert law Eq. (8).

$$\tau_\lambda = \frac{\Phi_\lambda}{\Phi_{0,\lambda}} = \exp(-\kappa_{\text{ext},\lambda} L) \tag{8}$$

Extinction is the combined attenuation from both absorption and scattering. The extinction coefficient is therefore the sum of the absorption ($\kappa_{\text{abs},\lambda}$) and scattering ($\kappa_{\text{sca},\lambda}$) coefficients, $\kappa_{\text{ext},\lambda} = \kappa_{\text{abs},\lambda} + \kappa_{\text{sca},\lambda}$. The scattering and absorption coefficients depend on the interaction between the turbid media and electromagnetic radiation and are described by a complex refractive index $\tilde{m}$ where the real part indicates the phase velocity relative to c_0 and the imaginary part refers to absorption through the medium.

The solution to Maxwell's equations for scattering of an electromagnetic wave by a homogenous sphere is known as the Mie solution, or Mie scattering [11]. Bohren and Huffman [12] provide complete solutions to Maxwell's equations for several scattering geometries and have been translated to FORTRAN computer code and later translated to several other computer languages. Scattering and absorption are usually discussed in terms of the effective cross-sections or efficiency factors which is the effective cross-sections divided by the geometric cross-section of the particle. The extinction efficiency is the sum of the scattering and absorption contributions to attenuation of light through the media. These contributions are depicted by the particle size relative to the wavelength of incident light (size parameter $x = \pi d/\lambda$) and optical properties of the particles (complex refractive index $\tilde{m}$).

Molecules and small particles, $x \ll 1$, scatter light toroidally, perpendicular to the dipole axis orientation. This scattering regime is commonly referred to as Rayleigh scattering. The Rayleigh scattering and absorption cross sections are defined as Eq. (9) and [10].

$$\sigma_{\text{sca}} = \frac{8\pi^5 d^6}{3\lambda^4} F(\tilde{m}) \tag{9}$$

$$\sigma_{\text{abs}} = \frac{\pi^2 d^3}{\lambda} E(\tilde{m}) \tag{10}$$

Where $F(\tilde{m})$ and $E(\tilde{m})$ are functions of the complex refractive index $\tilde{m} = n - ik$, Eq. (11) and (12).

$$F(\tilde{m}) = \frac{(n^2-k^2-1)^2+4n^2k^2}{(n^2-k^2+2)^2+4n^2k^2} = \left|\frac{\tilde{m}^2-1}{\tilde{m}^2+2}\right|^2 \tag{11}$$

$$E(\tilde{m}) = \frac{6nk}{(n^2-k^2+2)^2+4n^2k^2} = -\text{Im}\left(\frac{\tilde{m}^2-1}{\tilde{m}^2+2}\right) \tag{12}$$

It can be seen that the Rayleigh scattering cross section is proportional to the particle diameter to the power of 6 and the incident wavelength to the power of -4. A common example of Rayleigh scattering is the scattering of broad band solar radiation by atmospheric gases. As the scattering process is preferential to shorter wavelengths it consequently gives the sky its blue appearance during the day and reddish appearance during a sunset. Only the longer wavelengths of radiation will arrive to an observer through a longer path length of the earth's atmosphere as the shorter wavelengths have been scattered away Figure 9.

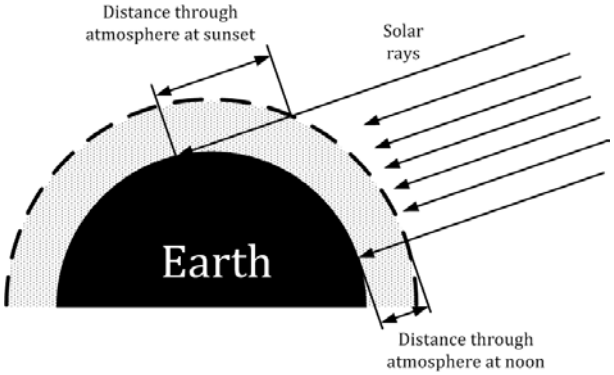

Figure 9: *Solar radiation path length through the earth's atmosphere.*

As Rayleigh scattering is elastic scattering, involving no energy exchange. An incident photon is absorbed, exciting the molecule/molecules to a virtual state, and relaxation to the initial state occurs by re-emitting the photon in a toroidal pattern at the same wavelength. Part of the scattering process is inelastic, involving energy exchange. This scattering process is called Raman scattering. Raman scattering can be split up into Stokes and anti-Stokes, where Stokes is relaxation to a higher vibrational state and anti-Stokes is relaxation to a lower vibrational state. The majority of the scattering process is elastic, which is why the Rayleigh scattering signal is orders of magnitude greater than the Raman signal. The Stokes signal is usually stronger than the anti-stokes signal as it depends on the population in the initial states. The population of states depicts that the upper energetic state is less populated, thus the Stokes transition will dominate.

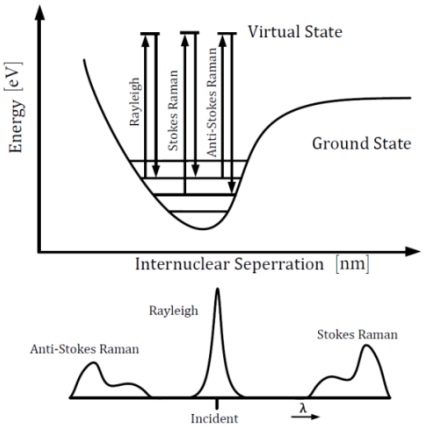

Figure 10: *Illustration of elastic and inelastic scattering processes in a Morse potential energy diagram.*

When the particles have a size comparable or larger than the wavelength of incident light, the scattering process enters into a different regime. This regime is usually referred to as the Mie regime and involves no energy exchange. In the Mie regime the scattering pattern, or phase function, becomes radically different as seen in Figure 11.

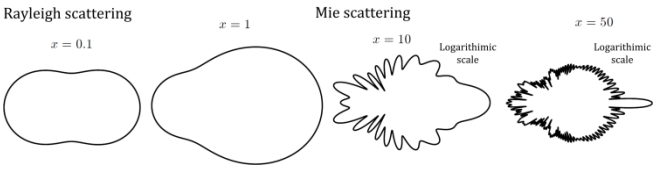

Figure 11: *Scattering phase functions for spherical particles of n-dodecane with refractive index $n = 1.422$, calculated with the Bohren and Huffman Mie code* [12] *for various size parameters.*

The Mie scattering cross section is proportional to d^2 (twice the geometrical cross section of the particle), thereby not as sensitive to the particle diameter as in the Rayleigh regime which is proportional to d^6. The Mie scattering cross section is however orders of magnitude greater than the Rayleigh cross section. These characteristics are shown in Figure 12 where the scattering cross-section has been calculated as function of the size parameter using the Mie code by Bohren and Huffman [12].

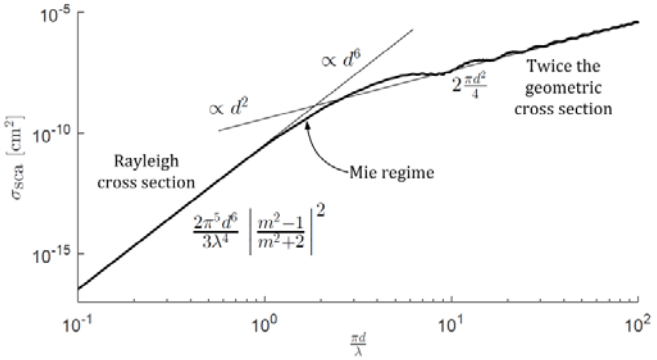

Figure 12: *Scattering cross section as function of size parameter, x, calculated using Mie code of Bohren and Huffman* [12] *assuming spherical particle of n-dodecane with refractive index $n = 1.422$ and incident light at 500 nm. The Rayleigh and twice the geometric mean cross sections are also indicated illustrating the transition from Rayleigh to Mie scattering regime.*

When the particles simultaneously absorb and scatter radiation (complex part of refractive index is >0) it makes more sense to evaluate the single-scattering albedo, ω_0, which is the ratio of the scattering cross-section to the extinction cross-section (Eq. (13)).

$$\omega_0 = {}^{\sigma_{\text{sca}}}/_{\sigma_{\text{ext}}} \qquad (13)$$

When the size parameter is $x \ll 1$ (Rayleigh limit), light extinction due to scattering is negligible compared to absorption.

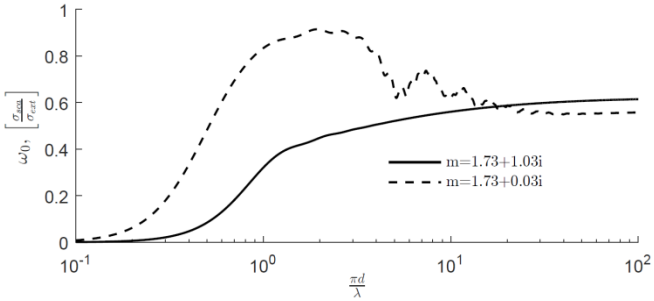

Figure 13: *Single-scattering albedo as function of size parameter, x, calculated using Mie code of Bohren and Huffman* **[12]** *assuming spherical particle of with refractive index $\tilde{m} = 1.73 - 1.03i$ and $\tilde{m} = 1.73 - 0.03i$ with incident light at 500 nm.*

When $x \sim 1$ however, extinction by scattering is significant as seen in Figure 13 where the single-scattering albedo is plotted as function of x for two refractive indexes.

Soot

Soot has been studied for decades and its complexities are still not fully understood. It is a product from combustion of hydrocarbons where the fuel burns in sub stoichiometric, or fuel rich, conditions. Hydrogen is continuously stripped from the fuel molecules creating soot precursor molecules, susceptible to form poly-aromatic rings that make up larger polycyclic aromatic hydrocarbons, or PAHs. These PAHs polymerize and form large strains of bound carbon which grow further into carbon particles as seen in Figure 14.

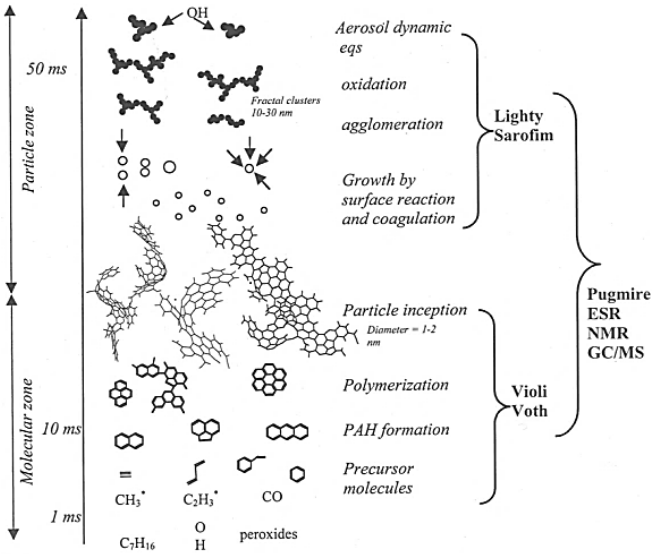

Figure 14: *The pathway to soot formation, taken from* [13].

Attenuation of light through a soot particle laden media occurs through the combined effect of scattering and absorption as mentioned above. The extinction coefficient in the context of soot is commonly written as K_{ext} and is the sum of the absorption, K_{abs}, and scattering, K_{sca}, contributions to attenuation (where K_{abs} and K_{sca} are the absorption and scattering coefficients respectively). If scattering can be neglected, the absorption coefficient (Eq. (14)) is equal to the Rayleigh absorption cross-section, σ_{abs}, multiplied by the number of suspended particles, N_{p}.

$$K_{\text{abs}} = -N_{\text{p}}\sigma_{\text{abs}} \tag{14}$$

K_{abs} can also be expressed in terms of the soot volume fraction f_v. Eq. (14) then becomes Eq. (15)

$$K_{\text{abs}} = -\frac{\pi 6}{\lambda} f_v E(\tilde{m}) \tag{15}$$

As Eq. (15) is valid only if scattering is insignificant, it is customary to express the absorption coefficient as Eq. (16).

$$K_{\text{abs}} = \frac{C f_v}{\lambda^{\alpha}} \tag{16}$$

Where C and α are empirical constants. The constant C is a function of the optical thickness. The term α is more commonly known as the dispersion exponent and, from early theories, was deemed to account for deviation from Rayleigh theory as a consequence of particle size. It was later found that this deviation was, to a higher degree, a consequence of spectral variations in the effective complex refractive index, proportional to the composition of the soot constituents for particles smaller than 60 nm [14], as seen in Figure 15.

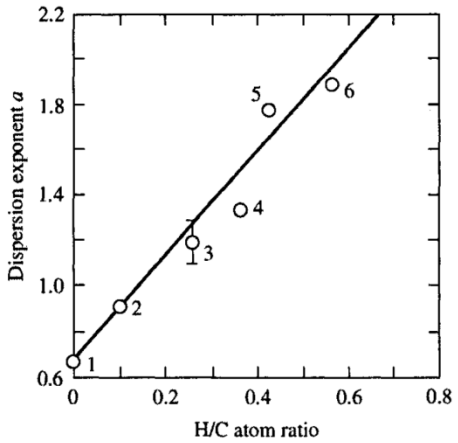

Figure 15: *Dispersion exponent of soot deposits as function of hydrogen to carbon ratio. 1 pure carbon, 2 acetylene/oxygen flame, 3 ethylene/oxygen flame, 4, 5, 6 ethylene/air flame. Taken from* **[14]**.

Nascent soot particles in the inception zone are small and contain more hydrogen which is continuously stripped and oxidized, altering the optical properties of the soot as it matures throughout the flame (Figure 14). This is often referred to as soot maturity, where fully mature particles are made up of amorphous carbon only [15]. The dispersion exponent can then be thought of as the deviation of the soot optical properties from amorphous carbon. The spectral dependence of the dispersion exponent can be expressed by Eq. (17).

$$\alpha = -\left(\frac{d\ln K_{\text{ext}}}{d\ln(1/\lambda)}\right) \tag{17}$$

Even though the refractive index is wavelength dependent and a specific value is connected to a specific wavelength, a single value $\tilde{m} = 1.57 - 0.56i$ has been widely used throughout the years [16,17,18,19]. The refractive index is vital in segregating scattering from absorption, using light scattering theory, in order to determine the true absorption coefficient.

The individual contributions from absorption and scattering to extinction are often determined using Mie theory [12]. The assumption is that the particles in the flame are spherical or spherical equivalent. The Mie solution calculates the extinction, absorption and scattering efficiency factors beyond the Rayleigh regime (Q_{ext}, Q_{abs} and Q_{sca} respectively). These efficiency factors are related to the soot volume fraction by Eq. (18).

$$K_{\text{x}} = \frac{3Q_{\text{x}}f_v}{4r} \tag{18}$$

The absorption coefficient can be determined by measuring the extinction coefficient and knowing, or assuming, optical properties and size distribution of the soot particles. The uncertainty of the wavelength specific refractive index is probably the biggest uncertainty of in-situ quantitative measurements of soot.

The real and imaginary parts of the refractive index are not independent of each other, but are related through the Kramers-Kronig (KK) relations. The KK relations are essentially the Hilbert transform, which are mathematical relations connecting the real and imaginary parts of a complex function. For Mie scatterers the scattering amplitude in the forward direction (S_0) is independent of polarization and is a complex function, Eq. (19), that obeys the KK relations [20].

$$Z(\lambda) = Z_r(\lambda) - Z_i(\lambda) = \frac{i[\text{S}_{0r}(\lambda) - S_{0i}(\lambda)]}{x} \tag{19}$$

The extinction efficiency is related to the real part of the scattering amplitude, and thereby the imaginary part of the complex function $Z(\lambda)$, through Eq. (20).

$$Q_{\text{ext}} = \frac{4\text{Re}(S_0)}{x^2} = -\frac{4Z_i(\lambda)}{x} \tag{20}$$

Studies to determine the in-situ wavelength dependence of the soot's optical properties have been done in the past [21,22,23,24]. These studies have been performed on laminar diffusion flame burners. Charalampopoulos and co-workers [22,21,23] measured the dynamic scattering and attenuation of light simultaneously for several wavelengths of incident light, in order to gain knowledge of the refractive index through the KK relations. Williams and Shaddix [24] measured the dimensionless extinction coefficient, k_{e}, via transmission measurements coupled with gravimetric sampling of in-flame soot onto a TEM (transmission electron microscope) grid. The dimensionless extinction coefficient is a term including the optical properties and size dependence of the soot at the specific wavelength and is related to the extinction coefficient through Eq. (21) and related to the optical properties and size of soot particles through Eq. (22).

$$k_{\text{e}} = \frac{K_{\text{ext}}\lambda}{f_v} \tag{21}$$

$$k_{\text{e}} = -(1 + \alpha_{\text{sa}})6\pi E(\tilde{m}) \tag{22}$$

The measured k_{e} coupled with Rayleigh Debye-Gans calculations of soot scattering, implied that the refractive index of soot is the vicinity of $\tilde{m} = 1.75 - 1.03i$ at 635 nm with fair certainty.

Scattering by fractal aggregates (Rayleigh Debye-Gans)

The scattering by soot particles needs to be estimated in order to achieve accurate predictions of soot volume fraction and size distribution. As shown in Figure 14, soot particles formed in flames agglomerate and generate long strains, or aggregates, of soot rather than individual spherical particles. This can also be seen in the TEM images of typical soot aggregates from atmospheric flames in Figure 16.

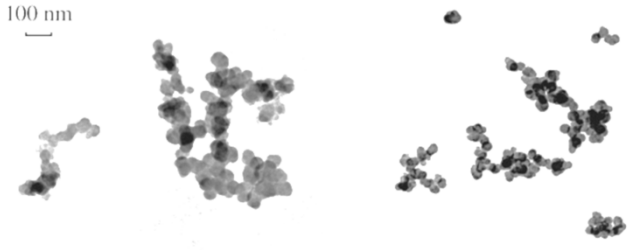

Figure 16: *Transmission Electron Microscope images of soot aggregates extracted from atmospheric diffusion flames (kerosene and ethylene respectively). Taken from Williams et. al.* [24].

The Rayleigh Debye-Gans theory implies that a scattering object of arbitrary shape may be considered as a composition of substructures smaller than the Rayleigh limit. Rayleigh theory is then applicable assuming each substructure is unaffected by the other substructures that make up the aggregate [12,25]. The total scattering and absorption cross-section for an aggregate of N monomers is defined as Eq. (23) and (24) respectively.

$$\sigma_{\mathrm{sca}}^{\mathrm{agg}} = N^2 \sigma_{\mathrm{sca}} g(x) \tag{23}$$

$$\sigma_{\mathrm{abs}}^{\mathrm{agg}} = N \sigma_{\mathrm{abs}} \tag{24}$$

Where σ_{sca} and σ_{abs} are the Rayleigh cross-sections for a single monomer, Eq. (9) and (10) respectively, and $g(x)$ is the total scattering factor for a fractal aggregate and is defined by Eq. (25).

$$g(x) = \left(1 + \frac{16}{3D_{\mathrm{f}}} x^2 \left(\frac{R_{\mathrm{g}}}{d_{\mathrm{p}}}\right)^2\right)^{-D_{\mathrm{f}}/2} \tag{25}$$

Recall that x is the size parameter which is here a function of the primary particle diameter, d_{p}. The variable R_{g}, known as the radius of gyration, is the root mean square of the monomer distances from the center of mass of the aggregate and can be thought of as the overall radius of the aggregate. D_{f} is the fractal dimension of the aggregate [26]. TEM and light scattering measurements have found D_{f} ranging from 1.5 to 1.8 [27]. The value of D_{f} indicates either a compact (high D_{f}) or a more stretched (low D_{f}) aggregate structure. The growth of soot aggregates has been observed to follow a power law relationship between N and R_{g}, where $N \propto R_{\mathrm{g}}^{D_{\mathrm{f}}}$ (Eq. (26)) [28].

$$N = k_{\mathrm{f}} \left(\frac{R_{\mathrm{g}}}{d_{\mathrm{p}}}\right)^{D_{\mathrm{f}}} \tag{26}$$

Where k_{f} is a prefactor of order unity. The values k_{f}, D_{f}, N_{p} and d_{p} are usually extracted from TEM soot sampling, examples of which are shown in Figure 16.

With the recent increased understanding of scattering by aggregates it is evident that the Rayleigh and Mie theory [12] used in early investigations are successful in determining the soot volume fraction and volume equivalent aggregate spherical diameter [26].

Emissivity of sooting flames

As described in the sections above, many uncertainties of the optical properties of soot particles exist. For this reason, in any modelling applications, soot is treated as a grey body with a constant spectral emissivity. This assumption is quite crude as the absorption and emission of radiation from small particles depends on the size of the particles themselves according to scattering theory [12]. As seen above, the absorption cross-section of a spherical particle is proportional to $\sigma_{\mathrm{abs}} \propto \lambda^{-\alpha}$, where the dispersion exponent, α in Eq. (17), accounts for the spectral variations in the refractive index. However this exponent is itself dependent on the soot maturity. To approximate the spectral emissivity of the soot, Eq. (27) is used [29,30], where n and k in $\tilde{m} = n + ik$ are calculated using the empirical correlation of Chang et. al. [22]. The correlation is based on simultaneous measurements of dynamic scattering and attenuation of light for several wavelengths, determining the complex refractive index through the KK relations [20].

$$\epsilon_{\mathrm{soot}} = 1 - \exp\left(\frac{6\pi}{\lambda} \mathrm{Im}\left(\frac{\tilde{m}^2 - 1}{\tilde{m}^2 + 2}\right) \overline{f_v L}\right) \tag{27}$$

For an optically thick flame (high f_v) the radiance observed is confined to the outer shell of the soot cloud (L becomes shorter), due to re-absorption of radiation emitted from the soot in the central part of the soot cloud. Of course temperature also plays a big role in the observed radiance because the hottest soot emits higher thermal emission according to Planck's law. All these factors should be noted when measuring the spectral radiance through the line of sight. The quantity $\overline{f_v L}$, which is a combination of soot volume fraction and optical path length, includes these uncertainties [31]. It can be determined by measuring the spectral radiance from the flame with a calibrated spectrometer. It may be difficult to measure $\overline{f_v L}$ over a wide spectral range, so to simplify the estimation of the spectral emissivity, $\overline{f_v L}$ can be measured in a narrow spectral range and assumed constant over the rest of the spectrum. Measurements of the spectral radiance from a spray flame over the spectral interval 520-630 nm [32] have been used in these calculations. This leaves $\lambda^{-1}\mathrm{Im}\left(\frac{\tilde{m}^2-1}{\tilde{m}^2+2}\right)$ describing the spectral dependence of the soot emissivity. Regarding gas radiation, the two main contributors are CO_2 and H_2O due to their high absorptivity and relatively high concentrations compared to minor and intermediate combustion species. Emissivity spectra for a range of molecular gases can be generated by line-by-line

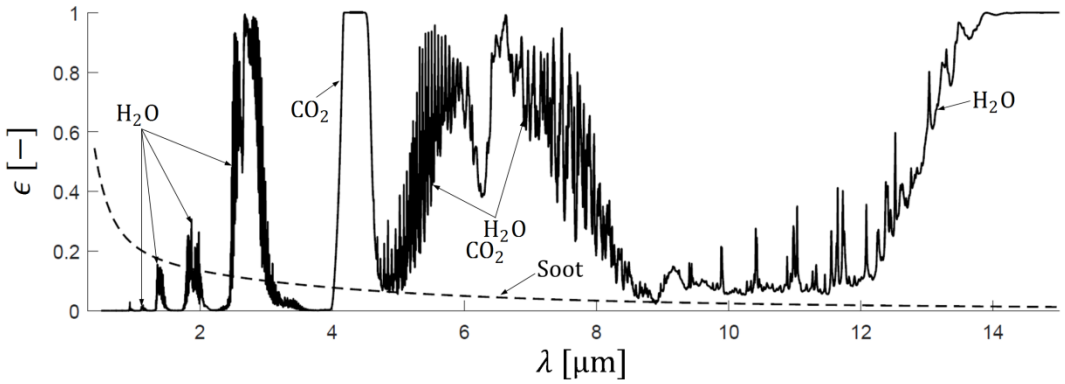

Figure 17: *The dashed line is the spectral emissivity of soot evaluated by Eq. (27), matching the measured emissivity between 520-630nm* **[32]** *and assuming constant* $\overline{f_v L}$*. The solid line is the emissivity of a* $x_{H_2O} = 0.036$ *and* $x_{CO_2} = 0.062$ *gas mixture at elevated temperature and pressure (*$T = 1000$ K *and* $p = 60$ bar*), resembling the bulk gas in a diesel engine cylinder with EGR corresponding to an* O_2 *concentration of 15%.*

calculations, narrow-band calculations, wide-band calculations or global models. Molecular lines have been mapped in the HITRAN and HITEMP databases [9,33]. For high temperature applications, the HITEMP database, validated by Aberti et. al. [34], is best suited. The emissivity spectrum of a gas mixture of H_2O and CO_2 at elevated pressure and temperature is plotted together with the soot emissivity in Figure 17. The soot emissivity is calculated with Eq. (27), assuming spectrally constant $\overline{f_v L}$ measured in the interval 520-630 nm.

This simplified calculation of the soot emissivity is very similar to the more detailed calculations by Stull and Plass [35]. It can be seen that the respective emissivity of soot and gas reside on either end of the spectrum due to the effect of the size of the soot particles, rendering the soot cloud nearly transparent at the wavelengths where gas radiation is significant. This justifies treating radiation from soot and gas separately, which can lead to significant simplifications from a modelling perspective.

Optical combustion diagnostics

In combustion research optical diagnostics are often employed for their non-intrusive nature, in-situ applicability and high temporal/spatial resolution. These methods are based on the physics mentioned above, isolating one or more of the physiochemical properties of the flame or interactions between electromagnetic radiation and the probed media in order to gain quantitative/qualitative information of the flame otherwise impossible to determine in-situ. Common cons of optical techniques are the experimental complexity, expensive equipment, advanced processing/interpretation and that optical access is required.
In this section a brief review of various baseline optical combustion diagnostics along with practical examples of their application will be given. First-hand experience (except Rayleigh scattering) with the techniques is drawn upon in order to provide a more intuitive understanding of the complex physics, conceptual functionality, experimental/interpretive complexity as well as common drawbacks for the various techniques.

Absorption based diagnostics

Several optical diagnostics are based on the absorption of radiation through the probed media. Knowledge of the absorbing nature of molecular gases and particulates is used to determine quantities such as chemical composition, soot volume fraction and temperature among others.

Infrared spectrometry

In infrared spectroscopy the absorption of infra-red radiation via molecular vibrational transitions is used to determine gas composition, species composition and in thermometry.
A widely used instrument in infrared spectroscopy is Fourier Transform Infra-Red spectrometer or FT-IR. This spectrometer takes the radiation from a wide band infrared source and passes it through a Michelson interferometer. The interferometer splits the signal through a beam splitter where half the signal is reflected off a fixed mirror and the other off a translating mirror before being recombined at the beam splitter (Figure 18). This results in constructive and destructive interference in the recombined signal and is therefore commonly referred to as the interferogram. The interferogram is in the time domain and contains information of all wavelengths emitted from the source. The reason an interferometer is used rather than a diffraction grating (commonly used in spectrometers) is that the long wave radiation is less susceptible to diffraction.
The interferogram is transformed to the frequency domain via the Fourier transform operation, thereof the name of the measurement technique, in order to spectrally resolve the intensity recorded from the source.

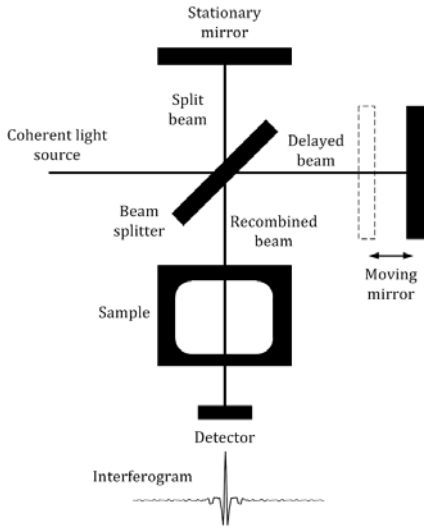

Figure 18: *FT-IR principle with Michelson interferometer. A typical interferogram is shown by the detector.*

The Fourier transform operation is defined from $-\infty$ to ∞ mirror retardation, Eq. (28).

$$I_e(\nu) = \int_{-\infty}^{\infty} R(x) \exp(-2\pi i \nu x) dx \tag{28}$$

The interferogram is only sampled over a finite interval such that the Fourier transform goes from $-L$ to L. This can be interpreted as the true interferogram from $-\infty$ to ∞ being multiplied with a truncation function, or a low pass filter window, which is unity within the mirror translation distance and zero otherwise. Consequently, this imposes a finite resolution and induces what is called the instrument line shape, ILS, function which distorts the spectral absorption lines interpreted by the spectrometer [36]. Other factors affecting the ILS are path-differences caused by misalignment and spectral dependencies of the optical components and signal electronics in the instrument. The latter effects are however only significant with high-resolution FT-IR [37].
FT-IR spectroscopy is widely used to determine the chemical composition of gases. This is done by sampling gas to a cell with a given temperature, pressure and path length. The constant ambient conditions within the cell omit the broadening effects of the spectral lines. The spectral transmission through the sample cell depends on the composition of the sample gas, where the species specific vibronic transitions (which absorb light) reside in designated intervals of the infra-red spectrum. Reference spectra of pure components obtained with the same instrument are used to generate a composite spectrum which is fit to the sampled spectra via a least squares algorithm in order to determine the concentration of the various species in the sample gas. As the reference spectra are obtained with the same instrument, effects from path-differences and ambient conditions can be neglected.
Examples of spectra from a cylinder gas with known composition of 10 % CO_2, 1770 ppm NO, 501 ppm CO and 49 ppm C_3H_8 acquired with a Gasmet DX 4000 FT-IR spectrometer can be seen in Figure 19 (above). Spectra from the same gas with 5 % H_2O vapor diluted can be seen in Figure 19 (below).

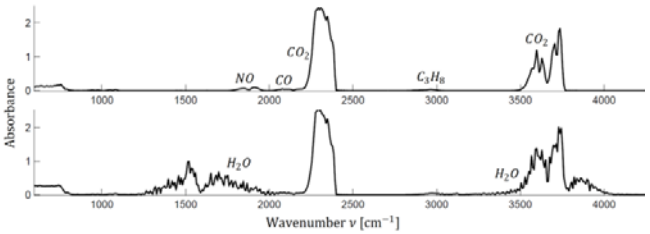

Figure 19: *Absorbance spectra of a cylinder gas with known composition of* 10 % CO_2, 1770 ppm NO, 501 ppm CO *and* 49 ppm C_3H_8 *(above) and absorbance spectra of the same gas with* 5 % H_2O *vapor added (below). Spectra were obtained with a Gasmet DX* 4000 *FT-IR spectrometer with a resolution of* 4 cm^{-1}.

It can be seen that these spectra look very different from the spectra in Figure 6. This is because the FT-IR cannot resolve individual spectral lines and as a result the absorption bands appear very wide. However, most gases behave linearly nonetheless. Using a weighted least squares algorithm the gas composition is predicted with high accuracy as seen in Table 1.

Table 1: *Predicted gas composition using weighted least squares algorithm from spectra in Figure 19.*

Gas mix	CO_2 [%]	CO [ppm]	NO [ppm]	C_3H_8 [ppm]	H_2O [%]
Cylinder	10.80	540	1770	51	-
5% H_2O	8.82	460	1668	44	4.95

FT-IR spectrometry has also been used for in-situ thermometry in flames [38,39,40]. The transition lines within the 2350 cm^{-1} vibrational band of CO_2 were used in these studies. . In the infrared, scattering by soot particles can be neglected due to the long wavelength of the incident radiation compared to typical soot particle sizes. Assuming the gas is in thermal equilibrium, the emissivity is equal to absorptivity and can readily be found by measuring the spectral transmission through the flame. The flame temperature can then be derived based on a calibration of the spectrometer with a source with known emissivity, accounting for the quantum efficiency of the detector used. The hot lines appearing at higher temperatures (Figure 6 (below)) have a higher transmission through the surrounding cooler CO_2. These transitions make it possible to determine the maximum temperature of the flame. This technique has been successful in measuring the in-situ temperature of laminar diffusion flames [39,40] and premixed rich flat flames [38].
Infrared techniques have however the disadvantage of operating at relatively low temporal resolution, limiting its application in transient flames.

Extinction measurements

In turbid media, light is both absorbed and scattered. Transmission measurements in this kind of environment are usually referred to as extinction measurements. Extinction based measurements can be used in both quantitative as well as qualitative applications.
A widely used application of extinction based techniques is soot volume fraction measurements. As mentioned, the soot volume fraction in a flame can be determined by its absorbing properties. The absorption coefficient may be deducted from extinction measurements assuming a refractive index of the soot and accounting for the scattering component with e. g. Mie theory or RDG.

The most widely used technique for extinction measurements through the years has been laser extinction [19,22,21,23,18,24,41]. Laser extinction, as name indicates, uses a laser to measures the transmission through the flame in the optical path of the laser. There has been recent interest in spatially resolving extinction measurements as the spatial information can be gained at a fraction of the time and experimental complexity and accommodates the techniques applicability in transient flames. Extinction imaging measures the light attenuation spatially by imaging a back illuminated flame. These two techniques have been performed on a co-annular laminar diffusion ethylene flame in the optical arrangement seen in Figure 20. The burner used is described in in detail by Santoro et. al. [19].

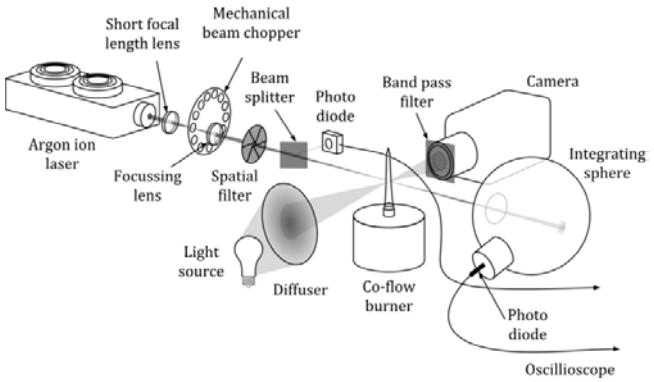

Figure 20: *Optical arrangement of laser extinction and imaging extinction of ethylene flame in co-flow burner. The laser was an argon ion laser, 514.5 nm as in* [19]*, and the extinction imaging setup had interchangeable band pass filter and LED illumination source centered at 400, 514.5, 630 nm.*

Laser extinction

The laser extinction was performed with an argon ion laser at 514.5 nm in the optical arrangement shown in Figure 20. The laser beam was focused through a short focal length lens and chopped at a frequency of 50 Hz at the focal point. The laser was chopped in order to measure the flame luminosity, I_f, in between laser pulses. The beam was then mildly focused through another lens with the beam waist located in the flame. A spatial filter was used to clean the spatial profile of the laser intensity, creating a thin beam waist. The diameter of the beam waist depicted the spatial resolution of the measurement. It was measured using a non-reflective cropping tool on a micrometer and found to be around 100 μm FWHM (Figure 21).

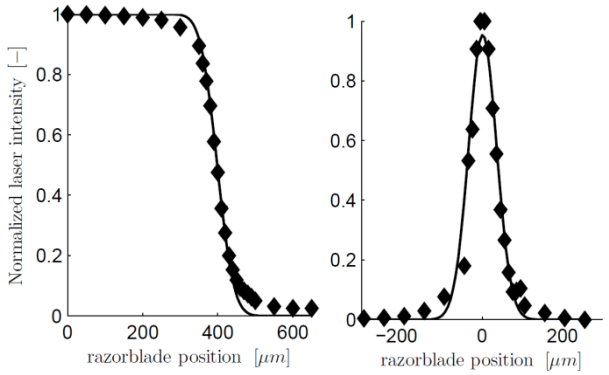

Figure 21: *Measurement of laser beam diameter through the flame. The data can be fit to a Gaussian profile with FWHM of around* 82 *μm.*

A metallic neutral density filter was used to split a portion of the beam to a photodiode in order to monitor the laser fluence, I_{ref}. The laser beam transmitted through the flame was measured with an integrating sphere equipped with a photo diode, I_{sf}. An oscilloscope was used to gather the data from the two photodiodes at 500 Hz. The laser intensity was measured with no flame present in order to establish the ratio between the signal measured by the integrating sphere, I_0, and the photo diode monitoring the laser fluence, $I_{0\mathrm{ref}}$.
The transmission through the flame is then defined by Eq. (29).

$$\tau = \frac{\Phi}{\Phi_0} = \frac{I_{\mathrm{sf}} - I_{\mathrm{f}}}{I_0 I_{\mathrm{ref}} / I_{0,\mathrm{ref}}} \tag{29}$$

The radial transmission profiles at various heights in the flame can be seen in Figure 22.

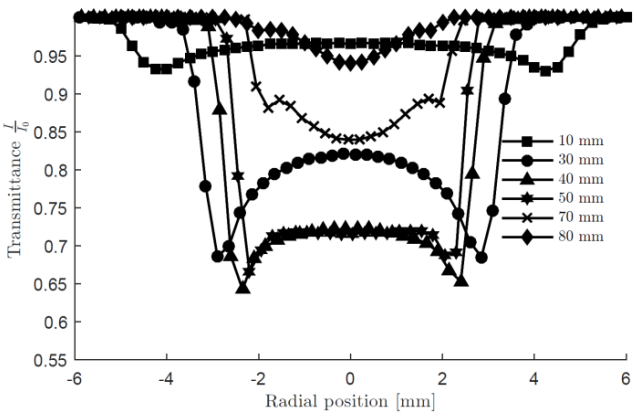

Figure 22: *Transmission profiles of argon ion laser through co-annular laminar ethylene diffusion flame at various heights in the flame.*

As mentioned, the transmission is related to the extinction coefficient, K_{ext}, through Eq. (8). Since this is a line of sight technique the extinction coefficient is measured through the optical path L. As the entire radial profiles are measured and the flame is rotationally symmetric, K_{ext} can be obtained from the transmission data via a tomographic reconstruction discussed in detail in a later section. The soot volume fraction has been determined using Eq. (14) assuming that scattering is negligible at the incident wavelength, $K \approx K_{\mathrm{abs}}$. Figure 23 shows the radial profiles of the soot volume fraction determined with the widely used complex refractive index of $\tilde{m} = 1.57 - 0.56i$ and that determined by Williams and Shaddix at 632 nm, $\tilde{m} = 1.75 - 1.03i$ [24].

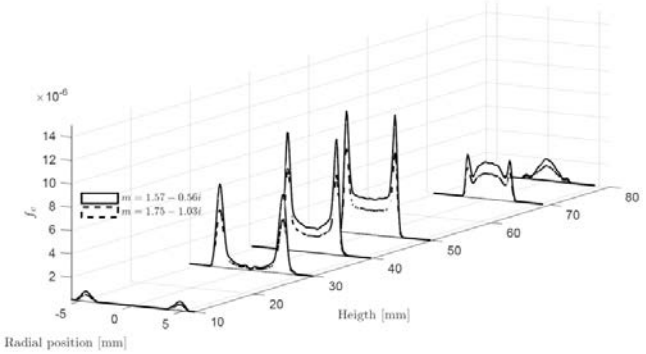

Figure 23: *Radial profiles of the soot volume fraction obtained with laser extinction with 514.5 nm at various heights in the flame assuming a complex index of refraction of* $\tilde{m} = 1.57 - 0.56i$ *and* $\tilde{m} = 1.75 - 1.03i$.

The impact of the refractive index on the determination of the soot volume fraction is evident where $\tilde{m} = 1.75 - 1.03i$ yields a 30 % lower soot volume fraction.

Extinction imaging

The extinction imaging setup applied an LED illumination source and a diffuser to back-illuminate the flame. The use of diffused lighting will be elaborated in later sections. Three different wavelength LEDs were used to gain information of the optical properties of the soot. The incident wavelengths used were 406, 520 and 632nm with bandpass filters on the camera of 400 ± 25 nm, 514.5 ± 5 and 628 ± 20 nm respectively. The camera was equipped with a 50 mm *f* 1.2 objective and a +2 dioptre close-up lens resulting in a projected pixel size of 0.11 mm (9 pixels per mm). The camera response curve deviates from linearity when the charge carrier concentration in the semi-conducting photosensitive chip becomes large enough to affect the total carrier concentration through electron collisions with energy exceeding that of the band-gap energy. For this reason the captured images were linearly corrected according to the camera response curve in Figure 24.

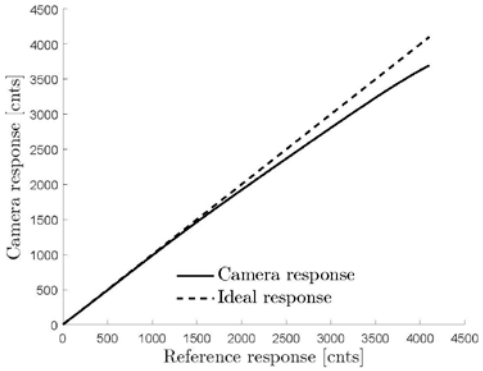

Figure 24: *Mean response curve of the Photron Fastcam SA-X2. The reference was an integrating sphere equipped with a calibrated Tungsten lamp and photodiode.*

This correction is elaborated in later sections. Extinction maps acquired at the three different wavelengths can be seen in Figure 25. It can be seen how the optical thickness of the flame increases at shorter wavelengths.
The ethylene co-annular flame is a well-known flame and has been subject to numerous studies regarding in-situ evaluation of soot optical properties [22,21,23,24,19]. The most rigorous recent study combined dual wavelength extinction and gravimetric sampling to determine the dimensionless extinction coefficient, k_{e}, and found it to be 8.67 at 632 nm [24].

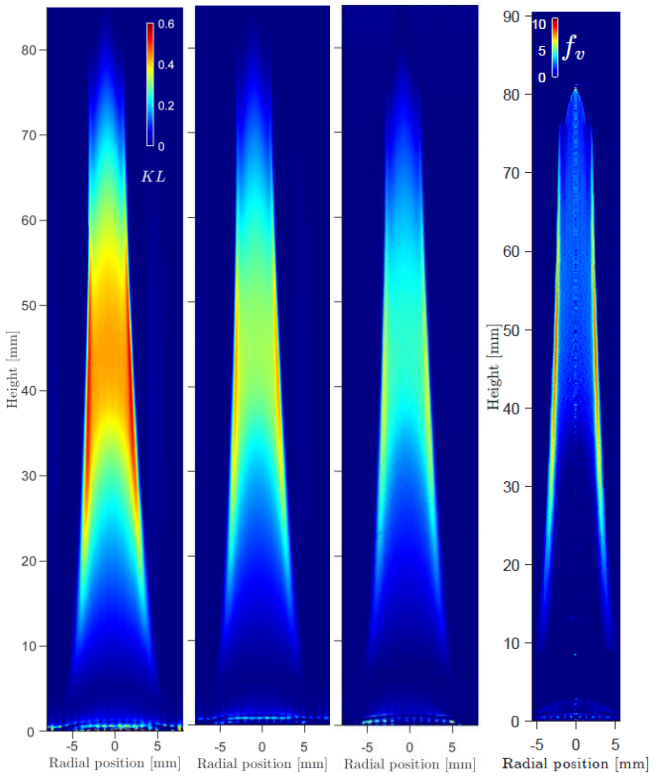

Figure 25: *Maps of the optical thickness KL of the co-annular ethylene flame at 400, 514 and 635 nm from left to right respectively. The far right image is a map of the soot volume fraction reconstructed from extinction imaging at 635 nm and* $k_e = 8.67$.

It can be seen in Figure 26 (above) that the curvature of the $\ln(K_{ext})$ vs $\ln(1/\lambda)$, across the spectral range 400-635 nm, decreases higher in the flame. This is also evident in the plot of the dispersion exponent, α in Figure 26 (below), which is the gradient of these curves (Eq. (17)). The gradient is higher between 400-514 nm compared to 514-635 nm in the lower part of the flame. The dispersion exponent becomes constant around across the spectral range 400-635 nm, 45 mm above the burner.

This indicates a change in the optical properties of the soot particles throughout the flame, where high H/C ratios of the soot in the inception zone cause the dispersion exponent to increase towards shorter incident wavelengths. Higher in the flame the soot matures and the H/C ratio decreases until the dispersion exponent becomes constant. This is consistent with the findings of Dobbins et. al. [42], who determined the transition from precursor particles (liquid like particles) to aggregates (solid structure displaying sharp density gradients at the particle border) to be around 40 mm above the burner.

As the curves in indicate, the spectral variation in optical properties relaxes towards longer wavelengths showing that the attenuation of shorter wavelength is more susceptible to nascent soot in the lower part of the flame. It is then fair to assume that the dimensionless extinction coefficient is relatively constant throughout the flame at 635 nm. With this assumption, the extinction image at 635 nm is used as the baseline measurement to determine the soot volume fraction, f_v, in the flame as seen in Figure 25 to the far right.

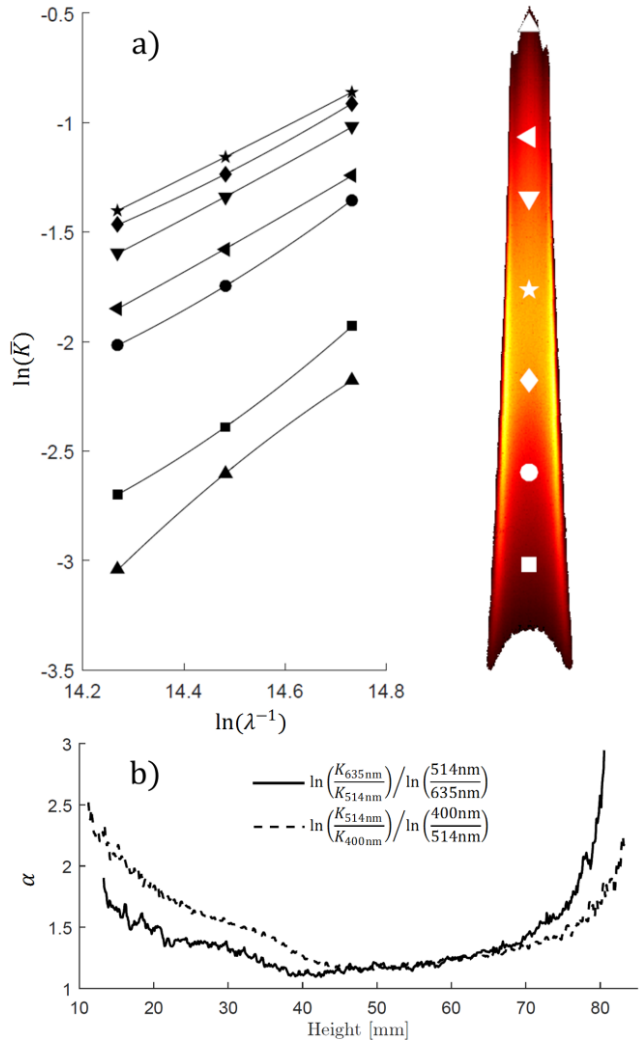

Figure 26: *(a)* $\ln(K_{ext})$ *as function of* $\ln(1/\lambda)$ *at various heights in the flame. The slope of these curves represents the dispersion exponent α which is also plotted as function of height in the flame (b).*

As f_v is a property of the flame k_e can be determined for the shorter wavelengths through Eq. (21). A least squares procedure with a Levenberg-Marquardt algorithm is used to determine k_e for each height in the flame by minimizing the residuals between the radial profiles of the soot volume fractions as determined by a specific k_e for the different wavelengths as shown in Eq. (30).

$$R = \min\left(\sum_{-r}^{r}\left(\frac{\lambda K_{ext,\lambda}(r)}{k_{e,\lambda}} - \frac{635\ nm K_{ext,635\ nm}(r)}{k_{e,635\ nm}}\right)^2\right) \qquad (30)$$

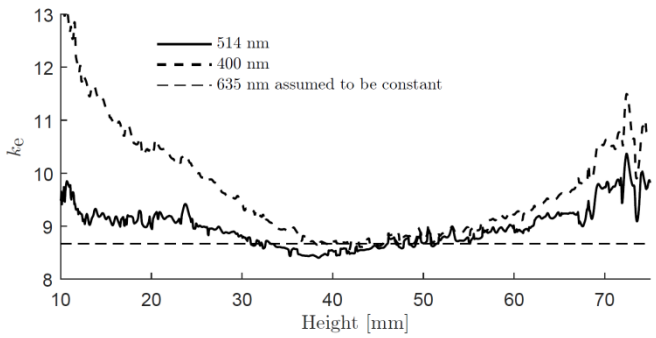

Figure 27: *Dimensionless extinction coefficient at 514 and 406 nm as function of flame height, determined from base measurement at 635 nm with* $k_e = 8.67$.

It can be seen that the variation in k_e throughout the flame relaxes at longer wavelengths. Higher in the flame the k_e for the two wavelengths are almost equal at a value close to 8.67, indicating a constant dispersion exponent (around 1.2 as seen in Figure 26 (below)). In this part of the flame the optical properties of the soot must be constant across the spectral range 400-635 nm, and the effects from scattering must be negligible.

Beyond 60 mm however, k_e start to diverge from each other. As the soot has apparently matured at this height in the flame (achieved constant optical properties), the diverging of k_e can be explained by growing aggregates moving the scattering regime into the Mie regime, thereby increasing the dispersion exponent. It can be seen that the dispersion exponents indicate a steeper gradient between 635-514 nm than 514-406 nm meaning the $\ln K$ vs $\ln 1/\lambda$ display the opposite curvature than lower in the flame. This can be explained by the scattering cross-section for the respective wavelengths transitioning from $\propto d^6$ in the Rayleigh regime, to $\propto d^2$ in the Mie regime as seen in Figure 12.

It could be possible to incorporate the KK relations to deduct the complex refractive index at 520 nm and 400 nm. The scattering amplitude can be determined with Mie calculations based on the volume equivalent particle diameter, $D_v^3 = d_p^3 N$. Based on the knowledge of the soot volume fraction evaluated at 635 nm with $\widetilde{m} = 1.75 - 1.03i$, S_{0r} can be determined at 406 nm and 514 nm by Eq. (18) and Eq. (20) via the measured extinction coefficient. S_{0i} can then be determined through the KK relations and a least square procedure could be used to find the corresponding real and imaginary parts of the refractive index. Unfortunately, time did not permit this further analysis of these measurements.

This section illustrates the vast amount of information that can be deducted from the extinction based measurements of flames. These measurements do however have the disadvantage of being line of sight and involves the assumption of rotational symmetry in order to deduct quantitative soot volume fraction measurements.

Scattering based diagnostics

Scattering based combustion diagnostics rely on the scattering nature of molecular gases and turbid media. Measurement techniques can be used to qualitatively measure/visualize flow fields, determine binary mixing and thermometry.

Schlieren/shadowgraph imaging

The schlieren and shadowgraph techniques are used to visualize the flow of fluids. Gradients in density induce a change in the local phase velocity in the medium. When a collimated beam passes through the medium, the density gradients distort the beam causing a spatial variation of the radiant intensity corresponding to the variation in the density field. The shadowgraph technique visualizes this effect directly while the schlieren technique applies a knife edge in the focal point to enhance the effect (Figure 28). The knife edge enhances the sensitivity of the diagnostic by effectively cropping rays of light in a preferential orientation. It should be mentioned that the camera lens should be focused on the probed media in order to capture schlieren effects properly and to avoid focusing artifacts [43].

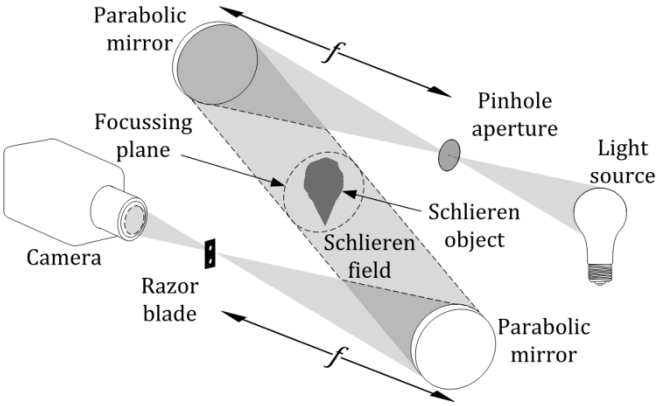

Figure 28: *Optical arrangement of a z-type schlieren system. The shadowgraph optical arrangement is identical omitting the schlieren stop (razor blade)*

Examples of shadowgraph and schlieren images of a small butane flame in air can be seen in Figure 29 (left) and (middle) respectively. It can be see that the spatial distortions in the shadowgraph are symmetric about the flame boundary while the schlieren is preferential appearing as a shadow on one side and light on the other. This is a consequence of the razor accepting only rays distorted in one direction. Figure 29 (right) shows a schlieren image of the butane gas jet in still air that would otherwise appear almost transparent to a shadowgraph. This illustrates the fine detail that can be made visible by applying a schlieren stop.

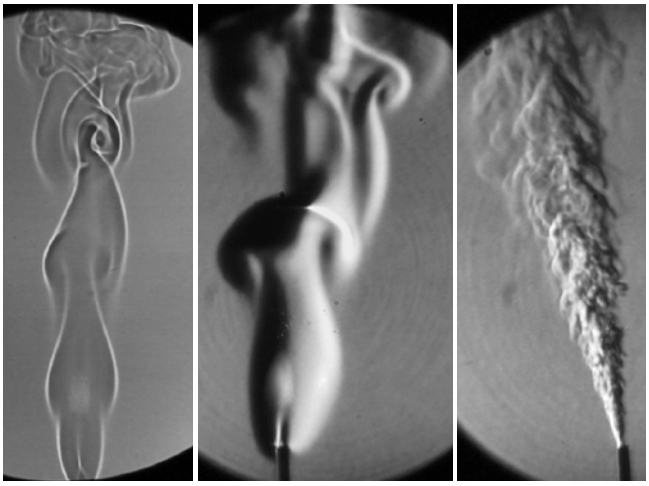

Figure 29: *Example of shadowgraph image of a small butane/air flame (left) and a schlieren image of the same flame (middle). Schlieren image of a butane gas jet in ambient air otherwise transparent to shadowgraphy (right).*

This technique is mostly used for qualitative measurements. However, quantitative schlieren techniques do exist and involve quantifying the deflection angle to facilitate quantitative measurements [44]. This is however advanced with limited applications, which is why the majority of schlieren measurements are qualitative.

Rayleigh scattering

The Rayleigh scattered light from molecules is proportional to the number density of species and cross section of the gas mixture.

$$I_{Ray} = I_0 n \Omega_c \sum_i x_i \frac{d\sigma_i}{d\Omega} \tag{31}$$

Where the subscripts Ray, 0, c and i denotes the Rayleigh scattered signal intensity, the laser intensity, the solid angle of the collection optics and the i^{th} species. The Rayleigh cross-section is a known quantity for most common gases and fuels and is proportional to $\sigma \propto \lambda^{-4}$. Thereby, the shorter the excitation wavelength the stronger the Rayleigh scattered signal. As I_{Ray} is proportional to N it is also, according to the ideal gas law, inversely proportional to temperature, $I_{\mathrm{Ray}} \propto T^{-1}$.

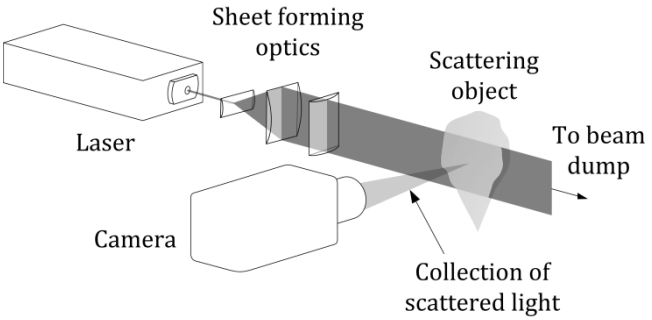

Figure 30: *Basic optical arrangement for an incoherent laser based combustion diagnostic i. e. Rayleigh scatter imaging, LIF or PLII.*

Rayleigh scattering can be used to measure the mixture field in a binary mixture through the relation in Eq. (32).

$$\frac{I_{\mathrm{mix}}}{I_a} = \left(\frac{\sigma_f/\sigma_a + N_a/N_f}{N_a/N_f + 1}\right)\frac{T_a}{T_{\mathrm{mix}}} \tag{32}$$

Where I_a and I_{mix} are the Rayleigh scattered signals from the pure component a (e. g. ambient) and the gas mixture respectively. σ_f and σ_a are the Rayleigh cross-sections. N_a and N_f are the number densities of the a and f components respectively. T_a and T_{mix} are the temperatures of the pure component a and the mixture respectively. Solving the mixture field N_a/N_f requires the knowledge of the Rayleigh cross-sections and temperatures.
In the example of a vaporized fuel spray mixing with ambient gas of known composition, number density and temperature, the mixture field and temperature field can be found by measuring the scattered signal. As the temperature and mole-weighted Rayleigh cross-section of the ambient are known and the Rayleigh cross-section for the fuel is known, the mixture field can be considered as a binary mixture of fuel and ambient. Through energy conservation, a relationship between N_a/N_f and the adiabatic mixing temperature, T_{mix} can be built knowing the thermodynamic properties of the fuel and ambient [45]. This can be used to solve Eq. (32), thereby obtaining the mixture and temperature field shown in Figure 31.

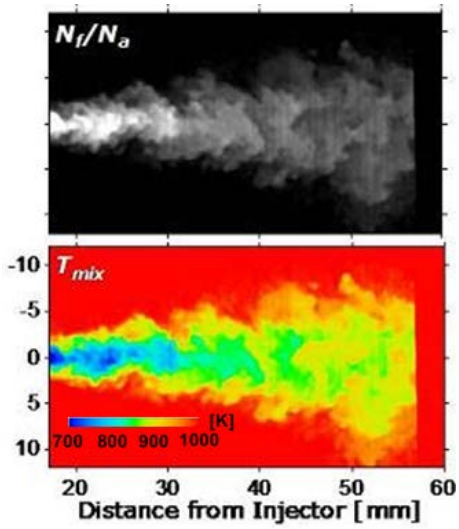

Figure 31: *Fuel to ambient number density ratio and mixing temperature determined by Rayleigh scattering taken from* [2,46].

As the Rayleigh scattering signal is proportional to λ^{-4}, a shorter incidence wavelength induces a significantly higher signal to noise ratio. However, it also makes the measurement more susceptible to mie scattering from particles which is orders of magnitude greater than the Rayleigh scattering signal and will therefore saturate the acquisition instruments. For this reason Rayleigh scattering measurements require an extremely clean environment free of particles, limiting the application to non-sooting environments.
However, molecular scattering is spectrally broader than particulate scattering due to Doppler and collisional broadening, making it possible to isolate the molecular scattering. This can be achieved by introducing a narrow band-rejection filter centered on the laser emission wavelength as seen in [47].

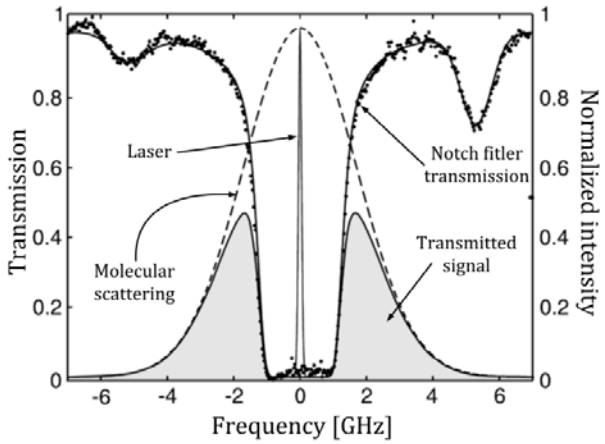

Figure 32: *The principle of the filtered Rayleigh scattering technique showing the transmission of the molecular scattering while filtering the narrow band of particulate scattering, taken from* **[47]**.

This enables the use of incident laser light in the UV where the Rayleigh cross-sections are high. The complexity of the technique increases however as the narrow notch filter requires special design and interpretation of the signal is dependent upon line broadening effects which themselves are sensitive to temperature and pressure.

Emission based diagnostics

Emission based diagnostics are based on the spontaneous emission of radiation from flames. The physics of emission properties from different gases, radicals and particles in the flame are used to measure temperature and flame structure.

Chemiluminescence

When a chemical reaction produces an atom or molecule in an excited state, from which de-excitation may occur through emission of a photon, the emission is orders of magnitude greater than what can be expected from thermal emission. This phenomenon is called chemiluminescence [43]. A range of species (e. g. C_2^*, CH_2^*, CH_2O^*, OH^*, CO_2^* etc.) may be formed in an excited state during combustion reactions. Chemiluminescence from different species and the magnitude of chemiluminescence can yield information of local flame conditions reaction pathways.
The hydroxyl radical is a highly reactive, short lived, radical formed by disproportionation of H_2O in the combustion reaction zone. In exothermic reactions the hydroxyl radical may be formed in an excited electronic state (UV) consequently emitting chemiluminescence around 308 nm through the electronic transition $A^2\Sigma^+ - X^2\Pi$. It is a commonly used tracer for determining the location of the hottest reaction and deducting information of the flame structure.

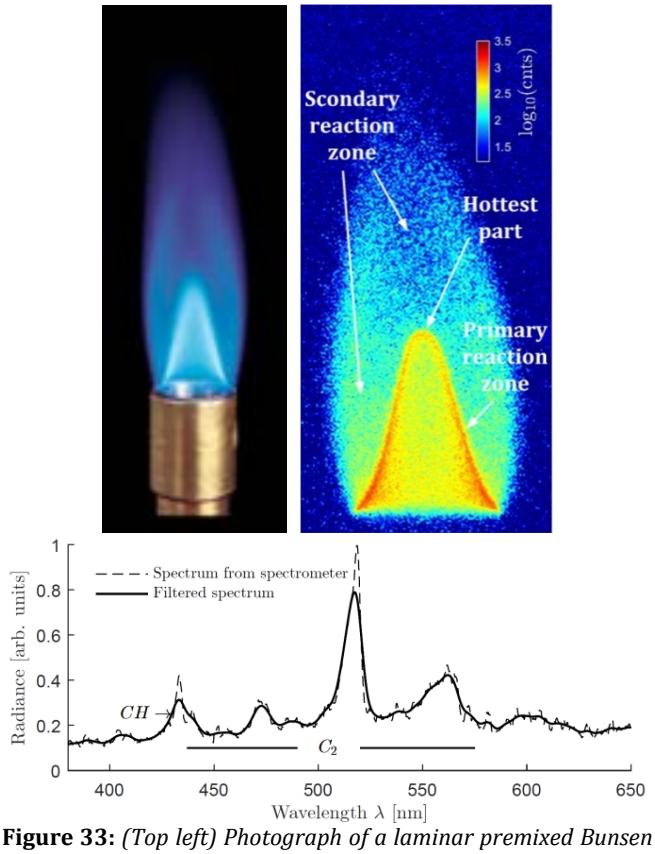

Figure 33: *(Top left) Photograph of a laminar premixed Bunsen type flame showing the visible flame emission. The bluish appearance of the flame is caused by chemiluminescence from CH and C_2 which extends to the short end of the visible spectrum. (Top right) False color image of OH^* chemiluminescence using a narrow 308 nm band pass filter on the camera. Indicated are distinct regions characterizing the flame. (Bottom) Spectral flame emission measured by an OOiBase32 spectrometer. The solid curve has been filtered with a low-pass Fourier filter.*

An example can be seen in Figure 33 (top) where a Bunsen type flame has been imaged through a narrow 308 nm band pass filter transmitting only the OH^* chemiluminescence centered on the 308 nm band. The spectral emission from the flame can also be seen in Figure 33 (bottom). The emission from the CH radical and the C_2 swan bands in the short end of the visible spectrum can be seen. The spectral response of the spectrometer was too poor in the UV to see the OH^* chemiluminescence.
The highest intensity of OH^* chemiluminescence is located in the primary reaction zone, while it is orders of magnitude lower in the secondary reaction zone. The flame stabilizes to a cone due to the laminar flame speed competing with the fuel/air stream and heat losses. The reactions taking place here are sufficiently exothermic to form electronically excited OH which is why the emission at 309 nm is much higher than the rest of the flame. In the secondary reaction zone, the emission from OH is thermal in nature and is therefore orders of magnitude lower than chemiluminescence from the inner cone. The OH^* chemiluminescence signal can then be used as a tracer to identify regions where the highest heat releasing combustion reactions are taking place.
The hottest part of the flame is the top of the flame cone. The reason for the chemiluminescence signal becoming slightly weaker in the upper part of the cone is that the chemiluminescence from the top of the cone has a longer path length through the OH in the secondary reaction zone. The chemiluminescence signal is then reabsorbed leading to a weaker signal arriving to the observer. The OH concentration is actually higher in the secondary reaction zone.
The chemiluminescence images provide spatial information of the flame structure where we can identify that the primary reaction zone is where the combustion reactions are hottest and thereby reacting in near stoichiometric conditions.
Under conditions where there is strong emission from soot, the OH^* signal may be contaminated by soot luminosity as the broad band Planck radiation extends further into the UV at higher temperatures. However, as the sooting regions are associated with rich combustion, its temperature is below the adiabatic flame temperature. The chemiluminescence emission is spectrally narrow which means the contamination from soot luminosity can be brought to a minimum using a very narrow band pass filter.

Black body emission

As soon as soot starts to form, broad band black body radiation dominates the spectral flame emission. Black body radiation is orders of magnitude higher than OH^* chemiluminescence and, as shown earlier, is highly temperature dependent. Figure 34 shows example images of broad band flame luminosity and narrow band emission at 308 nm from a Bunsen type diffusion flame.

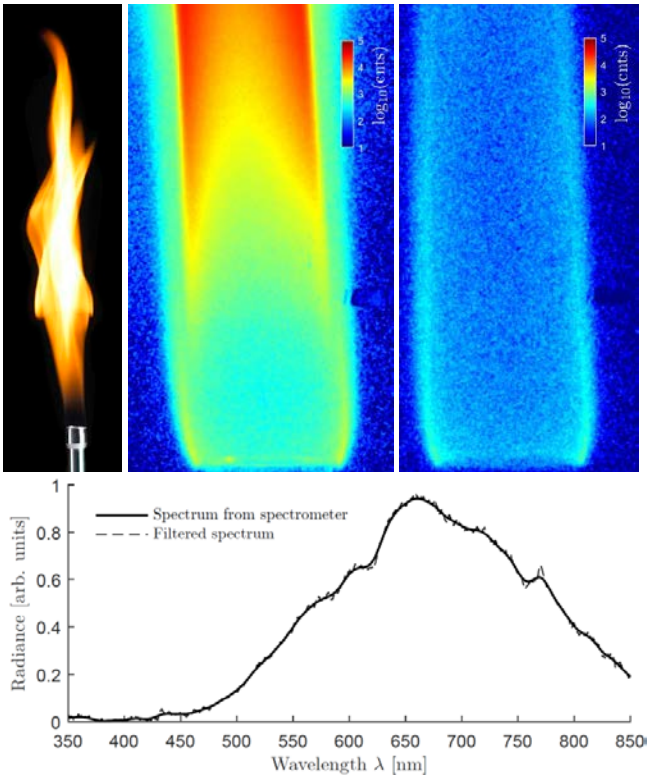

Figure 34: *(Left) Photograph of a Bunsen type diffusion flame. The orange yellow color is broad band luminosity from soot. (Middle) False color image of soot luminosity. (Right) False color image of flame emission at 308 nm. (Bottom) Spectral flame emission measured by an OOiBase32 spectrometer. The solid curve has been filtered with a low-pass Fourier filter.*

If we study the spectral emission we can see that the black body radiation dominates the emission spectrum. The blackbody radiation from hot soot is located inside the flame a ways downstream of the burner outlet. It can be seen that the OH^* chemiluminescence is most intense at the flame edge close to the burner outlet. This is where air is entrained into the fuel stream due to buoyancy forces enabling the fuel to burn near stoichiometric and is consequently where the flame is hottest. OH^* chemiluminescence can also be seen on the edges further up in the flame where the soot is being oxidized. It is however uncertain if this is in fact chemiluminescence or soot luminosity leaking through the narrow band pass filter. The temperature of the flame can be estimated based on the emission spectrum and the emissivity of the flame in the same way as mentioned in the infra-red spectroscopy section. The simplest application of this principle is two-color pyrometry, where the ratio between two wavelengths of emission is used to determine the temperature based on the assumption that the emitting body is gray across the spectral range of interest. A more rigorous application of this principle, omitting the gray body assumption, is to measure the emissivity via spectral transmission through the flame, as they are related through Eq. (33).

$$\epsilon = 1 - e^{-K_\lambda L} \tag{33}$$

The spectrum must be corrected for the quantum efficiency of the spectrometer. This is done by in-situ calibration with a source of known emissivity. Spectrometers in the visible range are significantly faster than those in the infra-red such that they can be applied in transient flames. However, the influence from scattering by soot particles may not be negligibly small in the visible as in the infra-red which poses more uncertainty in determining the true emissivity based upon extinction measurements. Another note is that the temperatures determined from flame emission in the visible rely upon soot and care must be taken in interpretation of such measurements. In the infrared one can evaluate temperatures based on emission from soot or from gases, giving the possibility of thermometry in soot-free conditions [38].

Stimulated emission based diagnostics

Stimulated emission based diagnostics exploit the absorbing properties of molecules and particles in order to induce emission of photons. A laser is typically applied due to its coherent and monochromatic nature and ability to deliver a high localized narrow spectral flux. These techniques can be used to measure flame structure, molecular concentrations, flow visualization, soot volume fraction and thermometry.

Laser- induced fluorescence

Fluorescence is a process that occurs when a molecule is electronically excited via absorption of electromagnetic radiation which leads to subsequent de-excitation via emission of a photon at a wavelength red-shifted from the excitation wavelength. This phenomenon may be induced via an external excitation source (typically a laser) targeting a specific electronic transition of a specific molecule. The fluorescence signal can then be measured.

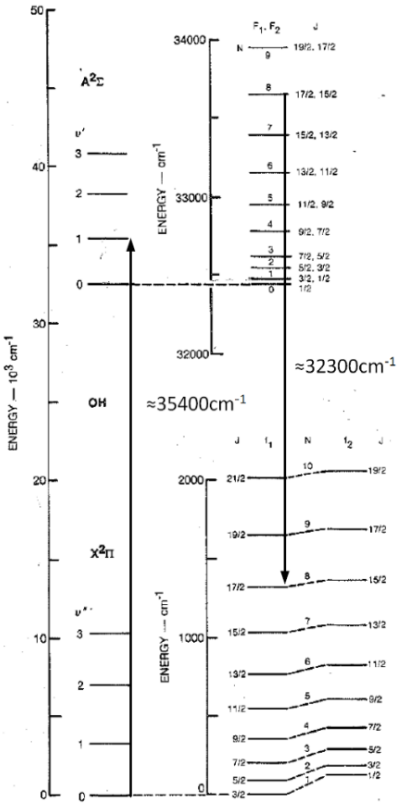

Figure 35: *Rotational energy levels of the $X^2\Pi(v'' = 0)$ and $A^2\Sigma^+(v' = 0)$ states of OH. The excitation wavelength for the Q(8) transition should be in the range 280-286 nm. The excitation and relaxation of the Q(8) transition are indicated by the arrows, taken from* [48].

When applying laser-induced fluorescence (LIF) in an imaging context, it is usually referred to as planar laser-induced fluorescence, or PLIF, as a planar laser sheet is

needed to spatially resolve the LIF signal. A typical PLIF optical setup is identical to the arrangement seen in Figure 30. The laser wavelength typically targets a fluorescing component present in the medium. In certain cases the medium is seeded with a fluorescing component. This is typically done in flow visualization and thermometry applications.

A common application of PLIF in flames is OH PLIF. The fluorescence signal of OH is dependent upon the population in the ground state from which the transition occurs, which in turn is temperature dependent (Eq. (5)). Transitions with different temperature dependence can be targeted depending on the application. In many cases it is desirable to target a ground state whose population is fairly insensitive to temperature variations in the range of typical flame temperatures such that the fluorescence signal is independent of the temperature distribution in the flame. The Q(8) transition between the $X^2\Pi(v''=0)$ and $A^2\Sigma^+(v'=0)$ states of OH is fairly temperature insensitive in the range 1500-2500 K. This transition is indicated by arrows in the diagram of rotational energy levels in of the $X^2\Pi(v''=0)$ and $A^2\Sigma^+(v'=0)$ states in Figure 35.

The transition is targeted with a dye laser pumped with an Nd:YAG laser producing a tunable laser around 590 nm. The laser is further frequency doubled with a KDP crystal generating the 2nd harmonic resulting in a tunable laser in the UV. From the rotational energy level diagram in Figure 35 it can be seen that the laser wavelength should be between 280-286 nm. To target the exact wavelength of the Q(8) transition, an excitation scan was performed where the laser was tuned across the various absorption lines and the fluorescence signal recorded. This process identifies the exact laser wavelength inducing the various rotational transitions within the vibrational band. The KDP crystal was continuously tuned to give the maximum laser intensity at the doubling frequency.

Results from OH^* PLIF in the Bunsen burner diffusion flame can be seen in Figure 36 (middle). The PLIF technique makes visible the spatial distribution of OH in the diffusion flame where the local heat release is insufficient to produce electronically excited OH (Figure 36 (right)). The thermal emission from OH is otherwise too weak and is drowned out by soot luminosity (Figure 36 (left)). This gives valuable information about the flame structure identifying a reaction zone with a rich premixed flame forming soot that is carried further downstream. A diffusion flame oxidizes the soot at the flame periphery where there is an abundance of oxygen.

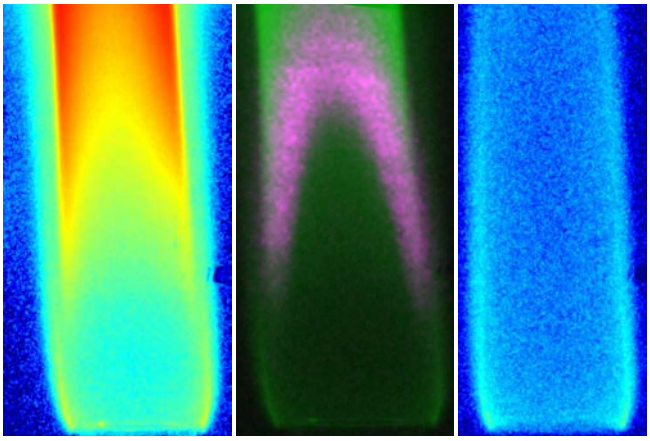

Figure 36: *(Left) Bunsen burner diffusion flame imaged with long pass filter showing the broad band flame luminosity. (Middle) Bunsen burner diffusion flame imaged with long pass filter with the OH^* PLIF image superimposed. (Right) Bunsen burner diffusion flame imaged with band pass filter showing OH^* chemiluminescence.*

The LIF technique can be used to target other species, revealing other characteristics of the flame. Another commonly targeted species in combustion applications is formaldehyde (CH_2O) as it is associated with low temperature reactions relevant to the first stage of ignition (cool-flame), or the initial breakdown of common hydrocarbons. Combining LIF imaging of OH and CH_2O can be used to identify the spatial location of low and high temperature reaction in the flame. This has, for example, been used in the study of HCCI engine combustion, investigating the influence of the charge homogeneity on the resulting ignition process [49].

As a final note, it should be mentioned that all molecular relaxation does not necessarily occur via emission of a photon. Processes that lead to a decrease in the fluorescence intensity have been given the umbrella term quenching. Quenching mechanisms are difficult to quantify and therefore pose significant uncertainties for the PLIF technique, especially quantitative PLIF.

Laser-induced incandescence

Similarly to PLIF, PLII is based on laser induced emission. However, PLII does not target specific molecules, rather exploits the absorbing properties of soot. Laser energy absorbed by soot particles in the flame result in local heating of the particles up to 4000K. As soot is a near black-body emitter, the local heating induces a stronger incandescence proportional to the amount of energy absorbed by the particles.

$$S_{\mathrm{LII}} \propto \pi d^2 \int_{\lambda_1}^{\lambda_2} \overbrace{\frac{4\pi d}{\lambda}\mathrm{Im}\left(\frac{\tilde{m}^2-1}{\tilde{m}^2+2}\right)}^{\text{Emissivity}} \cdot \overbrace{\frac{2\pi h_{\mathrm{p}} c_0}{\lambda^5 (e^{h_{\mathrm{p}} c_0/\lambda k T}-1)}}^{\text{Planck radiation}} d\lambda \qquad (34)$$

The first term represents the emissivity of the soot particles and the second term is the spectral Planck radiation. At the same time the soot can lose energy from heat conduction to the surrounding gas and through sublimation of the particles. For this reason PLII measurements are often calibrated by laser extinction measurements. Assuming the particles are within the Rayleigh limit, the extinction coefficient is equal to the absorption coefficient. The soot volume fraction can then be determined by Eq. (14). A single extinction measurement is required if the soot volume fraction is homogenous through the line-of-sight, L.

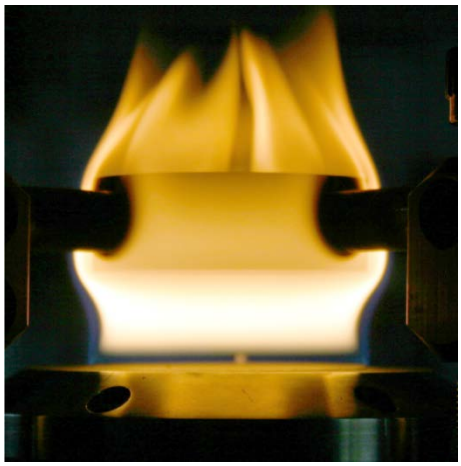

Figure 37: *One-dimensional flat ethylene/air flame from a McKenna flat flame burner with a flame stabilizing plate.*

This can be achieved with the McKenna flat flame burner seen in Figure 37 where the soot volume fraction was measured to be $f_v = 2.5 \cdot 10^{-7}$ 10 mm above the burner in a premixed ethylene/air flame with equivalence ratio of 2.3 and gas flow of 10 l/min. The LII signal can be calibrated spatially knowing the soot volume fraction at one height in the flame. The LII signal is very sensitive to the spatial intensity distribution of the laser and to the laser fluence. In LII experiments there is often reference to the LII fluence curve which is the time integrated LII signal as function of the laser fluence. For practical reasons it is desirable to have a LII signal that is relatively independent of variations in the laser fluence. The effect of the spatial intensity distribution in the laser on the LII signal can be seen in Figure 38.

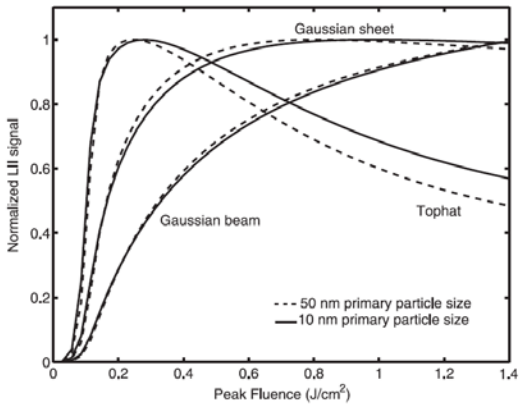

Figure 38: *Laser fluence curve for three different spatial distributions in the laser intensity* [50].

It can be seen that a Gaussian sheet produces a plateau where the LII signal is fairly invariant to the laser fluence. Too low laser fluence causes the LII signal to be sensitive to the decay of the laser energy through the flame caused by extinction, while too high laser fluence leads to significant particle sublimation decreasing the LII signal. The Gaussian sheet profile can be achieved with a telescope of cylindrical lenses and a square aperture.
As the soot is heated up to around 2000 K higher than the surrounding soot by the laser, the induced incandescence is more intense at shorter wavelengths than the flame due to Wiens displacement law. A spectral short pass filter can be used to filter out the longer wavelengths, and elastic scatter from the laser, such that the background flame luminosity is sufficiently suppressed, thereby increasing the signal to noise ratio of the LII signal (Figure 39).

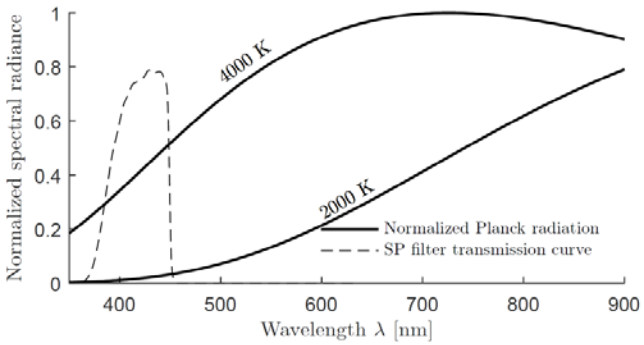

Figure 39: *Plot of the spectral radiance from the laser-heated soot (4000 K) and the surrounding soot (2000 K) along with the transmission curve for a typical 450 nm short pass filter. The wavelength range shown is the typical response range for imaging sensors.*

An LII measurement of the ethylene/air premixed flat flame was performed with an optical arrangement similar that of Figure 30. The laser used was a frequency doubled Nd:YAG (532 nm) with a pulse energy of 5.5 mJ formed into a laser sheet with a Gaussian sheet distribution. The camera was equipped with a 450 nm short pass filter in order to suppress background flame luminosity and elastic scatter from the laser. The spatially resolved soot volume fraction in the premixed ethylene/air flat flame was determined knowing the soot volume fraction 10 mm above the burner from extinction measurements (Figure 40).

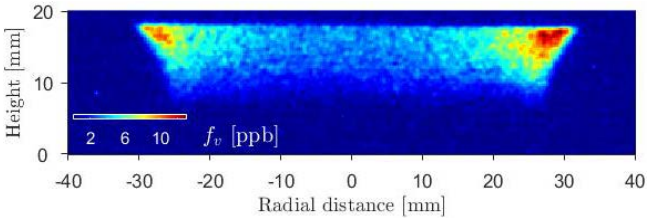

Figure 40: *Spatially resolved soot volume fraction in the ethylene/air flat flame burner with stabilization plate, as measured with LII.*

It can be seen that the soot volume fraction is highest in the lobes of the flame where the flame bends around the stabilizing plate. Unburned fuel and combustible exhaust from the flame exit at the edges of the stabilizing plate and are combusted in a diffusion flame when emerging to the surrounding air. This causes locally higher soot volume fractions at the edges. The lower soot concentration in the center of the flame can be an artifact of the measurement technique as the LII signal from the center of the flame has a longer path length through the flame where the signal can be reabsorbed. This is one of the uncertainties of this kind of measurement as reabsorption of the LII signal may be hard to determine when the soot distribution in the flame is in-homogenous.
LII can be used in particle sizing applications as the temporal decay of the LII signal can be coupled to a particle size distribution [51].
The clear advantage of LII over extinction measurements in determining the soot volume fraction is that is not a line-of-sight technique. However, LII is limited to optically thin conditions. When the soot becomes too optically thick, the attenuation of the laser sheet through the flame is so severe that the laser fluence becomes too low to induce a detectable LII signal throughout the entire path length through the flame [52]. Increasing the laser fluence induces particle sublimation of the first laser-heated soot particles.

Processing methods

Interpretation of experimental data is significantly aided by sophisticated processing methods. Correct application of these techniques can enhance the quality of the data and enable extraction of more information. Care must be taken however, as misuse of certain processing methods may lead degradation of the data and in some cases to corruption of data through introduction of artifacts. This section gives a summary of various image processing techniques, many of which have been applied in this work.

Filtering

Filtering is a technique applied to an image that modifies or enhances compared to the original image. It can be used to

remove or emphasize specific features. Some commonly used filtering techniques are detailed below.

Spatial filtering

Spatial filtering is one of the simplest forms of filtering where a local value is changed by a function of the neighboring values. The neighborhood is usually user defined and the function defined by the desired filtering effect. Examples of filtering windows can be seen in

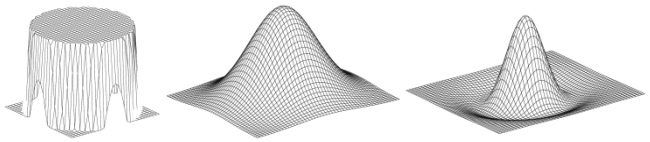

Figure 41: *Window functions for spatial filtering. (left) circular averaging filter, (middle) Gaussian averaging filter and (right) a Laplacian window.*

For example a Gaussian filter applies a Gaussian weight to the neighboring data points effectively reducing noise but also inducing blurring effects. A median filter applies the function of assigning the local data value the median value of the neighborhood. This filter preserves sharp edges to a higher degree than a mean filter and is especially effective in removing speckle and salt & pepper noise as seen in the examples in Figure 42.

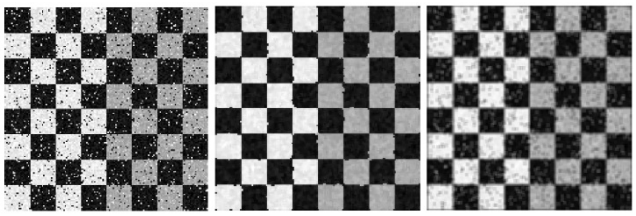

Figure 42: *Examples of spatial filtering of a sharp checker pattern image with added white and salt & pepper noise (left) using a 3x3 median filter (middle) and a 3x3 Gaussian filter.*

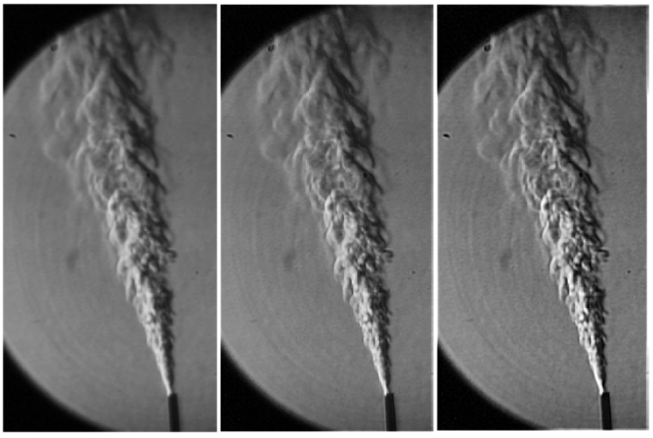

Figure 43: *(left) Original image of butane gas jet in ambient air, (middle) sharpened using spatial window weighting local pixels higher and (right) subtraction of the 2nd derivative, obtained with 3x3 Laplacian operator, from the original image.*

Different filters display different advantages and disadvantages and are tailored for different applications. For example, spatial filters can also be used to sharpen an image. A way to di this is to weight the local pixel higher than the surrounding pixels. Another way is to filter with the Laplacian operator, generating the 2nd derivative if the spatial pixel intensity. This image can then be subtracted from the original image thereby enhancing edges. Examples of these two sharpening methods can be seen in Figure 43. The Laplacian image sharpening approach is however sensitive to noise and is often used in conjunction with a smoothing filter priory.

Fourier Filtering

The objective of a Fourier filter is to remove specified frequencies embedded in the recorded signal. This is done by multiplying the signal in the frequency domain with a window that keeps the desired frequency range and removes the rest as can be seen in the example in Figure 44.

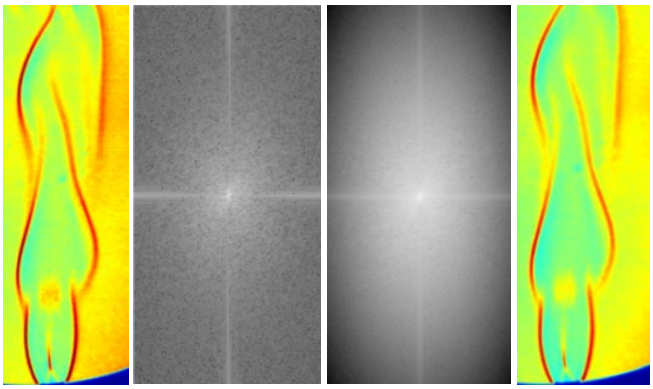

Figure 44: *(Left) Original shadowgraph image of butane flame together with it's 2D Fourier transform (middle left). (Middle right) The 2D Fourier transform image multiplied by a low-pass hamming window with the resulting low-pass filtered image (right).*

The results yield a less noisy image with the low frequency shadowgraph pattern maintained. Too small a window may lead to significant blurring effects and the amount of filtering is application specific. If the image to be filtered includes fine structured details (high frequency), a low pass filter may add a blurring effect as demonstrated in Figure 45.

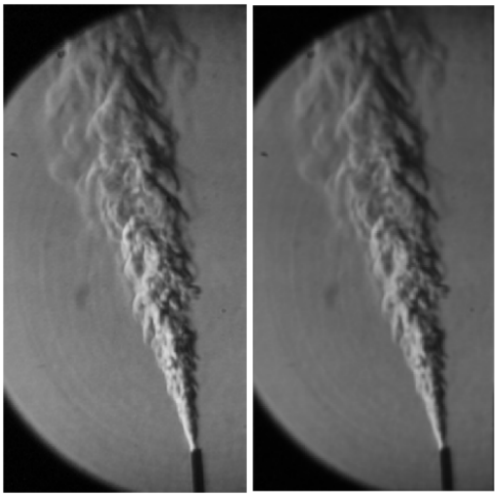

Figure 45: *(left) Original image containing high frequency information. (Right) The same image filtered with a small window, showing blurring effects of the high frequency information.*

Various window shapes exist as the nature of the cut-off pattern in the frequency domain induces artifacts in the filtered image in the form of waves as seen in Figure 46.

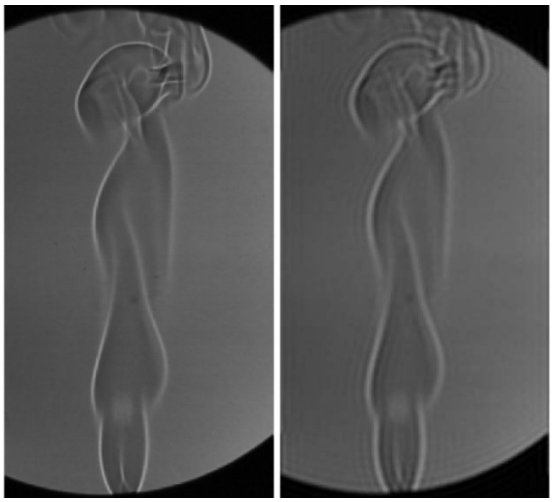

Figure 46: *(Left) original image and (right) Fourier filtered image using rectangular window with sharp cut-off.*

Adaptive filtering

Adaptive filters tailor the filtering method to the local structure and properties of the image. These filters are well suited to situations where there is little prior knowledge of the signal being processed or extensive knowledge of the noise variance.

Tomographic reconstruction

A tomographic reconstruction is an image that is reconstructed from a series of projections. The most common example of its application is in X-ray CT scanners, or computerized tomography scanners, where images of internal tissue and organs are reconstructed from angular projections of X-ray transmission.

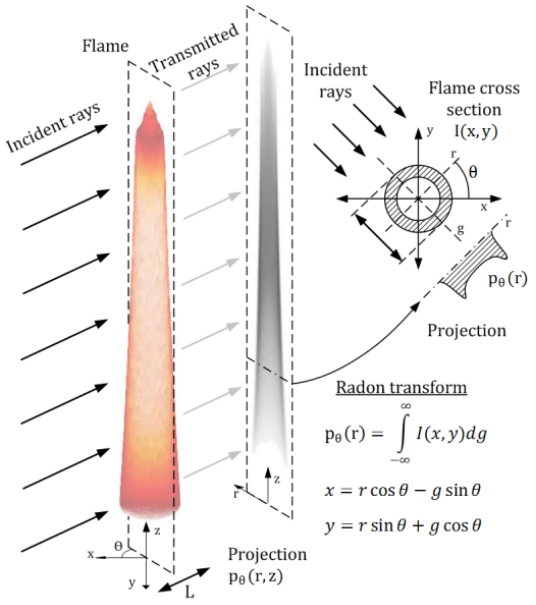

Figure 47: *Illustration of line of sight projection of the co-annular diffusion flame created by transmission of incident rays through the flame. (Right) 2D transmission through the flame as acquired by extinction imaging. (Left) Illustration of the relation between the true image of a horizontal flame cross-section, $I(x,y)$, and the projection or transmission, $p(r,\theta)$.*

Transmission of incident rays through the line of sight from a flame can be thought of in the same way, where incident rays are attenuated through the path length L creating a projection of the flame. This is illustrated in Figure 47 along with the relationship between the projection, $p_\theta(r)$, and the true image, $I(x,y)$, of flame cross-section. This relationship is often referred to as the Radon transform. To achieve a reconstruction of the true image from projections, one utilizes the Fourier slice theorem. This theorem states that the 1D Fourier transform of the projection at angle θ is equal a slice through the origin of the 2D Fourier transformed true image at the same angle. This can be easily proven for $\theta = 0$ as r becomes equal to x and the integration over g is the same as integrating over y. Thus the definition of the Radon transform reduces to Eq. (35).

$$p_\theta(r) = \int_{-\infty}^{\infty} I(r,y)dy \tag{35}$$

The Fourier transform of this function is written as Eq. (36) and the spatial Fourier transform of $I(x,y)$ as Eq. (37).

$$\hat{p}_\theta(\upsilon) = \int_{-\infty}^{\infty} p_\theta(r)e^{-2\pi jr\upsilon}dr \tag{36}$$

$$\hat{I}(\upsilon,\rho) = \int_{-\infty}^{\infty}\int_{-\infty}^{\infty} I(x,y)e^{-2\pi j(x\upsilon+y\rho)}dxdy \tag{37}$$

Inserting $p_\theta(r)$ into Eq. (36) becomes Eq. (38).

$$\hat{p}_\theta(\upsilon) = \int_{-\infty}^{\infty}\int_{-\infty}^{\infty} I(r,y)\,e^{-2\pi jr\upsilon}drdy \tag{38}$$

One recognizes that Eq. (38) is the spatial Fourier transform of the true image along $r = x$ for $y = 0$ ($\theta = 0$). This tells us that $\hat{I}(\upsilon,\rho)$ can be constructed from $\hat{p}_\theta(\upsilon)$. This proof is illustrated in the diagram in Figure 48 for a more intuitive interpretation of the Fourier slice theorem.

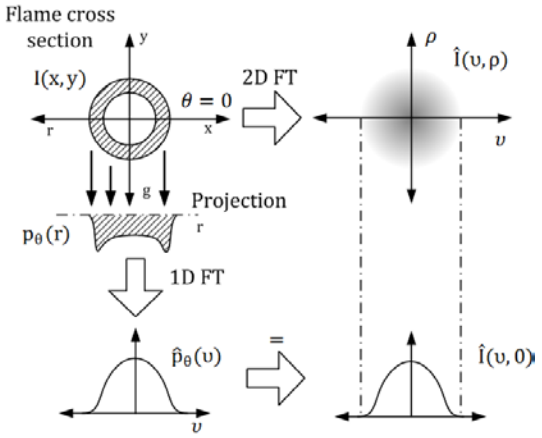

Figure 48: *Diagram illustrating the Fourier slice theorem.*

The inverse 2D Fourier transform of $\hat{I}(\upsilon,\rho)$ then gives us the reconstructed $I(x,y)$. However, the problem arises that the data in and around the origin of the image $\hat{I}(0,0)$ becomes dense while data further from the origin sparse. This is a direct consequence of the computational translation from (r,θ) to (x,y), resulting in an over representation of the lower frequencies in the center of

$\hat{I}(v,\rho)$ causing blurring effects. This can be seen in the example of a test image reconstructed from projection data with $d\theta = 1°$ in Figure 49. The projection data is shown in the form of a sinogram which is an image of the projections along r as function of the angle θ.

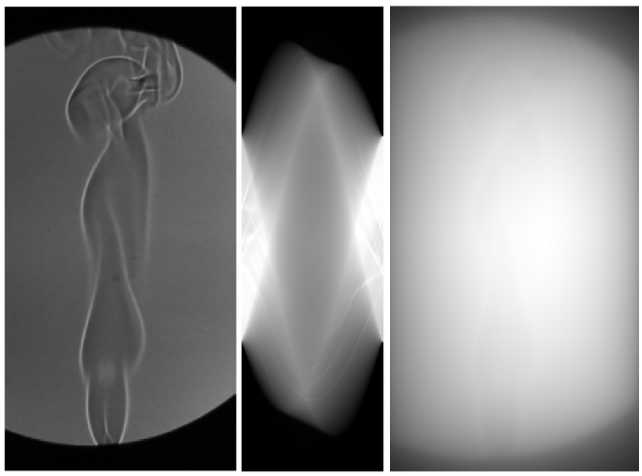

Figure 49: *Original test image, $I(x,y)$, (left) and reconstructed image (right) from unfiltered projections, $p_\theta(r)$, with $d\theta = 1°$ (middle).*

To account for the over representation of the low frequency data, a high-pass ramp filter, w, is applied. The resulting reconstructed image can be seen in Figure 50.

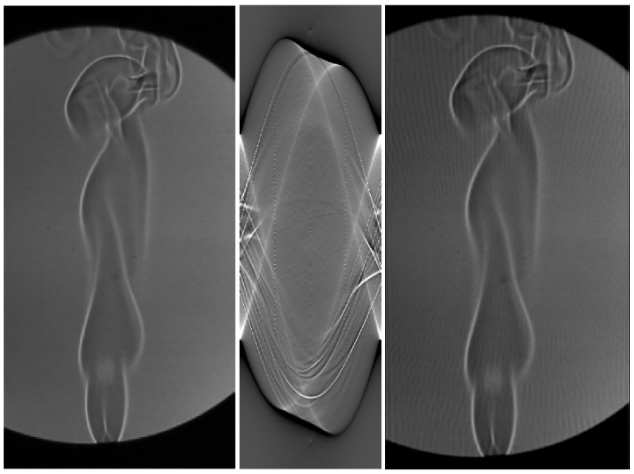

Figure 50: *Original test image, $I(x,y)$ (left) and reconstructed image (right) from projections, $p_\theta(r)$, with $d\theta = 1°$convolved with the Fourier transform of the high pass ramp filter, $p_\theta(r) * \hat{w}(r)$ (middle).*

It can be seen that the image $I(x,y)$ is well reconstructed when the high-pass ramp filter is used. A simultaneous low-pass filter can be applied to filter out high frequency noise from the reconstructed image. This is done by simply multiplying the high-pass ramp filter with the desired low-pass window. Examples of commonly used windowing functions are plotted in Figure 51.

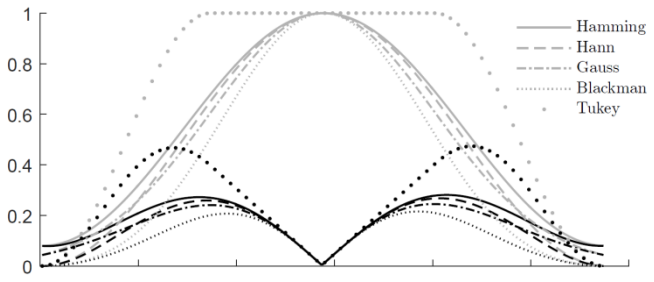

Figure 51: *Commonly used windowing functions in Fourier filtering. The gray curves show the true window function while the black curves show the window function multiplied with the high-pass ramp filter.*

The quality of the reconstruction is dependent on the number of projections and the complexity of the image being reconstructed. In cases where the object can be considered rotationally symmetric, only one projection angle is needed. This is the case with the co-annular diffusion flame. The filtered sinogram from the measured optical thickness, KL, is the same for all projection angles, θ, when the flame is rotationally symmetric. As we are using the same measured profile to generate the sinogram it is extremely important to identify the exact center of the profile. This is done by cross-correlation of the measured profile and mirrored profile (as the projection is mirrored at $\theta = 180°$). The reconstruction procedure for obtaining the spatially resolved extinction coefficient, K_{ext}, at one height in the co-annular flame can be seen in Figure 52.

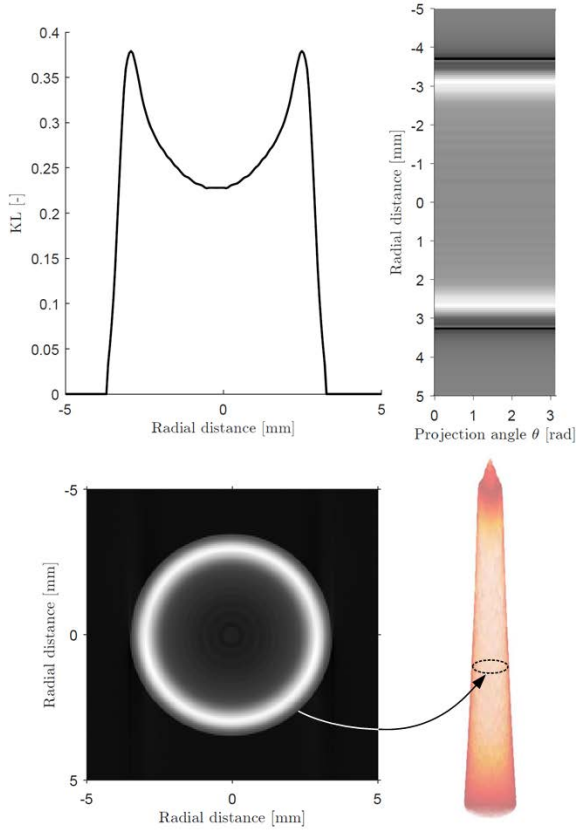

Figure 52: *Map of extinction coefficient at one height in the co-annular flame reconstructed from one line of sight measurement of the optical thickness. The filtered back projections are the same for each angle assuming the flame is rotationally symmetric.*

Liquid fuel sprays

As the flames to be studied are liquid fuel spray flames, resembling those occurring in the cylinder of a diesel internal combustion engine, a fundamental knowledge of spray combustion is required. The subject of spray characteristics and mixture formation is important in many applications, not only to CI engines. The properties of a fuel spray (e.g. liquid phase penetration, atomization, air entrainment, and mixture formation) govern the combustion process as they occur on a longer time scale than that of the chemical reactions taking place. In direct-injection Diesel engines these properties influence the engine performance and emission profiles. Fuel properties, initial and ambient conditions and injector nozzle geometry, among others, play a significant role in the resulting spray characteristics.

Dimensionless numbers

In fluid mechanics, a fuel spray can be characterized by a range of dimensionless quantities. These quantities are useful in comparing fuel spray characteristics with multiple variable parameters. The relevant dimensionless numbers are listed in the following.

The Reynolds number is one of the most common dimensionless quantities and expresses the ratio of inertial forces to viscous forces.

$$\mathrm{Re} = \frac{\rho U d}{\mu} \tag{39}$$

Where ρ, μ and U is the density, dynamic viscosity and velocity of the fuel respectively, and d is the diameter of the nozzle. The Reynolds number is used as a scaling parameter through dynamic similitude when changing e.g. fuel, nozzle diameter or injection pressure.

The Weber number is usually applied in multiphase, free-surface flow conditions and is the ratio of external inertial forces to the surface tension of the fuel.

$$\mathrm{We} = \frac{\rho U_{\mathrm{lg}}^2 d}{\gamma} \tag{40}$$

Where γ the surface is tension of the fuel and U_{lg} is the velocity of the fuel relative to the ambient gas. For injection into a still environment $U_{\mathrm{lg}} = U$. The Weber number is used characterize the liquid core's tendency to break up and form droplets.

Ohnesorge [53] found that the breakup process could be described by the Weber number and Reynolds number and he went on to define the Ohnesorge number which relates the viscous forces to inertial and surface tension forces, eliminating the velocity dependence. It is the ratio between the square of the Weber number and the Reynolds number.

$$\mathrm{Oh} = \frac{\sqrt{\mathrm{We}}}{\mathrm{Re}} = \frac{\mu}{\sqrt{\gamma \rho d}} \tag{41}$$

The Ohnesorge diagram in Figure 53 shows the breakup regimes identified (illustrated in Figure 54) by Ohnesorge as function of the various jet parameters involved in the Reynold and Weber number.

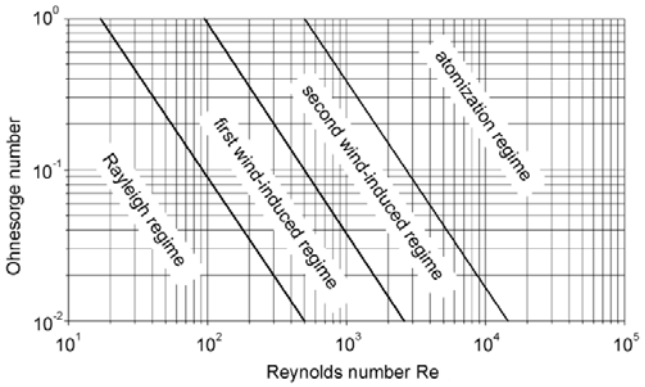

Figure 53: *Ohnesorge diagram of different jet break-up regimes* [54].

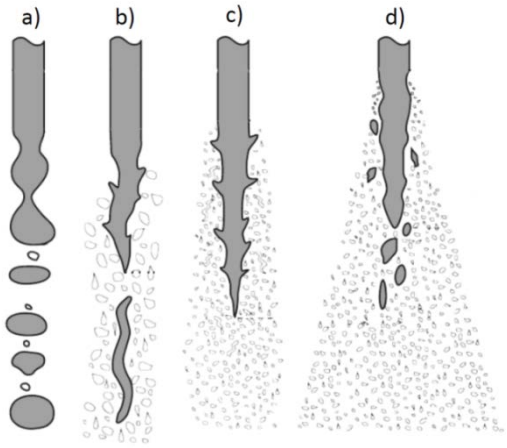

Figure 54: *Illustrations of the different breakup regimes a) Rayleigh regime, b) First wind-induced regime, c) Second wind-induced regime and d) Atomization regime* [55].

The Rayleigh breakup regime occurs at low jet velocities. In this regime, surface tension forces are dominant and aerodynamic forces are negligible and no jet is formed. Rather, small perturbations of the free surface of the fluid grow until a spherical droplet is formed (Figure 54 a). The droplets formed are typically much larger than the nozzle orifice.

In the first wind-induced breakup, the mechanisms in the Rayleigh regime are amplified by aerodynamic forces (Figure 64 b). The intact liquid core length decreases and the droplet size decreases to the range of the nozzle orifice.

In the second wind-induced regime the jet becomes turbulent and the radial velocity of the jet disrupts the liquid surface causing droplets to break off the in-tact liquid core (Figure 64 c). This process continues until the entire liquid core disintegrates into droplets smaller than the nozzle orifice.

In the atomization regime droplets break off the liquid core immediately outside the nozzle orifice and continue until the liquid core is disintegrated (Figure 64 d). The droplets are much smaller than the nozzle orifice.

Spray atomization occurs when a liquid is injected at high velocity, typically through a nozzle, into a gaseous environment. The shear forces acting on the liquid/gas interface overcome the surface tension of the fuel, causing the liquid boundary to deform leading to the formation of ligaments along the liquid core. This process is commonly referred to as primary breakup. Similarly, the further breakup of these ligaments into smaller spherical droplets is referred to as secondary breakup. These processes are indicated in the illustration in Figure 55.

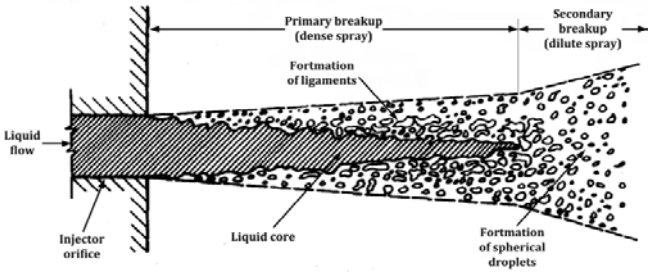

Figure 55: *Illustration of near-nozzle primary and secondary breakup processes* [56].

The liquid volume fraction in the dense spray region is high and decreases as the liquid ligaments break up into small droplets that evaporate quickly.
Another dimensionless number of relevance in fuel sprays is the cavitation number which relates the difference between local pressure and the vapor pressure of the fuel to the kinetic energy of the flow.

$$\mathrm{Ca} = \frac{p_{\mathrm{inj}} - p_{\mathrm{v}}}{0.5\rho U^2} \tag{42}$$

Where p_{inj} and p_v is the injection pressure and vapor pressure of the fuel respectively. The cavitation number is used to characterize the flows tendency to cavitate. Cavitation occurs when fluid flow bends around sharp corners causing a local pressure decrease that falls below the fluid vapor pressure. The adverse pressure gradient and flow separation usually occurs in the hole inlet region in the fuel injection nozzle, forming a vena contracta as shown in Figure 56 a.

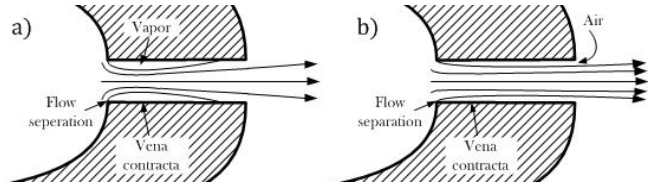

Figure 56: *a) Illustration of cavitation forming along the nozzle walls contracting the flow and b) illustration of total hydraulic flip* [57].

Several cavitation induced disturbances have been identified experimentally through visualization of in-nozzle flow and the proceeding atomization process including:
Vapor bubbles build up along the walls and cause a periodically oscillating contraction area [58].
Cloud-like cavitation bubbles periodically shed from the cavitating regions along the walls and collapse at the nozzle exit [59,60].
These processes have been identified as enhancers of jet break-up, generally causing larger dispersion angles of the spray, shorter liquid breakup lengths and smaller droplets [61]. However in some situations, conditions that cause flow separation and cavitation can result in complete separation of the flow. Under these conditions the ambient gas is free to be drawn into the nozzle orifice by the low-pressure region along the walls. The cavitation built up then collapse to the liquid core which remains shielded from the walls by the drawn in ambient gas [62]. This condition is called hydraulic flip as indicated in Figure 56 b. When hydraulic flip occurs, turbulence decreases as the flow does not experience wall shear and no adverse pressure gradient exists. The net result is that spray dispersion may actually decrease. However, the conditions that lead to total hydraulic flip, defined as complete separation around the entire liquid core up to the nozzle inlet, are somewhat abnormal, and have only been observed in scaled experiments at fairly low injection pressures [63,58,64]. Schmidt [61] reports that total hydraulic flip has never been observed in real-scale nozzles at realistic conditions. Rather, the cavitating regions that extend to the nozzle exit resemble a two phase flow consisting of both liquid and vapor. This flow has been termed super cavitation.

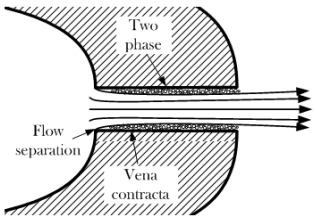

Figure 57: *Illustration of super cavitating flow where cavitating regions extending to the ambient consist of both liquid and vapor.*

Spray Vaporization

In the atomization regime the spray breaks up into droplet immediately at the nozzle exit. This leads to a drastic increase of the surface area of the liquid gas interface and the droplets evaporate quickly. The simplest model for evaporation of a droplet is the d square law, Eq. (43).

$$\frac{\partial d^2}{\partial t} = -K \tag{43}$$

Where K is the evaporation constant. For a static droplet, mass transfer is governed by diffusion and the d-square law states that K is constant meaning that d^2 decreases linearly over time. In this case K can be expressed as

$$K = \frac{8k_{\mathrm{g}}}{\rho_{\mathrm{l}} c_{\mathrm{pg}}} \ln(1+B) \tag{44}$$

Where $k_{\mathrm{g}}/\rho_{\mathrm{l}} c_{\mathrm{pg}}$ is the thermal diffusivity of the fuel and B is the Spalding heat transfer number given by Eq. (45).

$$B = \frac{c_{\mathrm{pg}}(T_{\mathrm{amb}} - T_{\mathrm{boil}})}{h_{\mathrm{fg}}} \tag{45}$$

Where c_{pg} is the specific heat of the fuel at the boiling temperature, T_{boil} is the boiling temperature, or saturation temperature, of the fuel at the ambient pressure and h_{fg} is the latent heat of vaporization. This was verified experimentally by Nishiwaki et. al. [65].

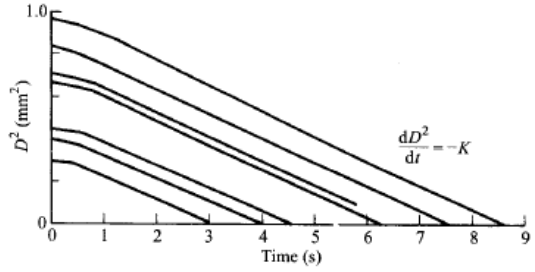

Figure 58: *Experimental verification of the d-square law for water droplets in atmospheric pressure and ambient temperature of* 620 °*C* [65].

Figure 58 shows that the evaporation of a water droplet in a still hot environment follows the d-square law after an

initial transient heat-up period in which the droplet surface is heated up to the boiling temperature.
The use of the boiling temperature assumes that the partial pressure of the fuel vapor in the film around the droplet is the same as the ambient which may be a crude assumption. Assuming mixing limited vaporization defining the conditions where the fuel and air mix, Siebers [66] defined the Spalding heat transfer number as

$$B = \frac{h_a(T_{amb},p_{amb}) - h_a(T_{sat},p_{amb}-p_{sat})}{h_{fg}(T_{sat})} \quad (46)$$

The subscript amb denotes the ambient conditions and sat the saturated vapor conditions. The difference $p_{amb} - p_{sat}$ is then the partial pressure of the ambient gas in the thin film around the droplet where the fuel is vaporizing. In the mixing limited assumption the quantity B is equal to the fuel/air ratio where the fuel is completely vaporized. Thereby, using the real gas equation of state gives the relation Eq. (47).

$$B = \frac{Z_a(T_{sat},p_{amb}-p_{sat})\cdot p_{sat}\cdot M_f}{Z_f(T_{sat},p_{sat})\cdot(p_{amb}-p_{sat})\cdot M_a} \quad (47)$$

Since p_{sat} and T_{sat} are related, T_{sat} can be found iteratively.
A droplet in motion experiences convective heat transfer which significantly affects the evaporation rate. The evaporation constant can then be expressed as a function of the Nusselt number Eq. (48).

$$K = \frac{4k_g Nu}{\rho_l c_{pg}} \ln(1+B) \quad (48)$$

The Nusselt number is yet another dimensionless number expressing the ratio between convective and conductive heat transfer. The correlation suggested by Faeth [67] in Eq. (49) can be used to evaluate the Nusselt number.

$$Nu = 2 + \frac{0.555 Re^{0.5} Pr^{1/2}}{\sqrt{1+\frac{1.232}{RePr^{4/3}}}} \quad (49)$$

A droplet in motion will decelerate due to drag and vaporize simultaneously and the convective heat transfer decreases as the droplet decelerates. Determining the droplet lifetime involves solving a set of ordinary differential equations for the vaporization rate and deceleration of the droplet. A calculation of the droplet lifetime of a 10 µm n-dodecane droplet in a still environment with ambient temperature of 900 K and density of 22.8 kg/m^3 traveling at different initial velocities can be seen in Figure 59. The initial temperature of the droplet is assumed to be uniform and equal to T_{sat}, omitting the initial transient heat-up period.

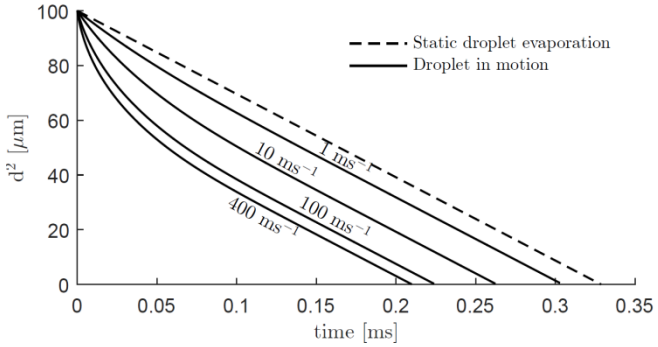

Figure 59: *Calculated evaporation rate of a 10* µm *n-dodecane droplet travelling at different initial velocities in a pressurized high temperature environment (T_{amb} = 900 K and ρ_{amb} = 22.8 kg/m^3). The calculations omit the initial heat-up period.*

It can be seen how the forced convective heat transfer significantly affects the evaporation rate and that as the droplet decelerates the evaporation rate approaches the d-square law. This example is for a single isolated droplet. In the dense spray region the number density of droplets is high and the evaporation rate of individual droplets is affected by neighboring droplets. Belland and Harstad [68] found that the evaporation rate in the dense spray region is primarily governed by diffusion as the partial pressure of the fuel vapor in the droplet film is high, increasing the saturation temperature toward the boiling temperature. In the dilute spray region, the entrained ambient gas reduces the partial pressure of the fuel vapor in the film around the droplets, increasing the evaporation rate.
However, an inherent assumption for droplets to form is that the surface tension of the fuel confines the liquid to spherical droplets. If a fluid reaches a state above its thermodynamic critical point it will have properties comparable to both gas and liquid at the same time. The important property in the context of sprays is the surface tension which diminishes near the critical point and is lacking in the super critical state. The consequence of this is that no droplets or ligaments are formed and the spray resembles a variable density gas jet [69]. This tendency requires the temperature of the liquid and the partial pressure of the vaporized fuel to be above the critical point. This is evident as twice the ambient pressure was needed to induce a supercritical mixing field for liquid N_2 injected into room temperature N_2 diluted with 20 % He compared to liquid N_2 injected into room temperature N_2 [70]. As no fuel vapor is present in the ambient gas upon fuel injection in an engine application, extreme ambient pressures would be necessary to induce this behavior in the dilute spray region where fuel/ambient mixing drives down the partial pressure of the fuel. In the dense spray region, the fuel concentration is high and thereby the partial pressure may be higher than the critical point. However, the temperature will also be low in this region due to the lack of entrained hot ambient gas. For these reasons the author speculates that it is unlikely that critical mixing occurs in CI engine relevant applications.

Fuel spray/jet characteristics

It is clear that the vaporization process depends on the mean droplet size, droplet speed (related to spray momentum), entrainment rate (related to spray dispersion angle) and ambient temperature and pressure. The internal geometry of the injector nozzle affects the internal flow and thereby governs the initial conditions of the spray i. e. mean droplet size and speed. As discussed above, the droplet vaporization rate is convection driven in the dilute regions of the spray and diffusion limited in the dense spray region. In vaporizing sprays the liquid phase penetration stabilizes
In a high temperature ambient, the entrained gas contains more energy increasing the vaporization rate, confining the liquid phase closer to the injector nozzle. A higher ambient pressure increases the turbulent transport of momentum from the injected fuel, increasing the spray dispersion angle/entrainment rate. These effects are evident in measurements of the stable liquid penetration length as seen in Figure 60.

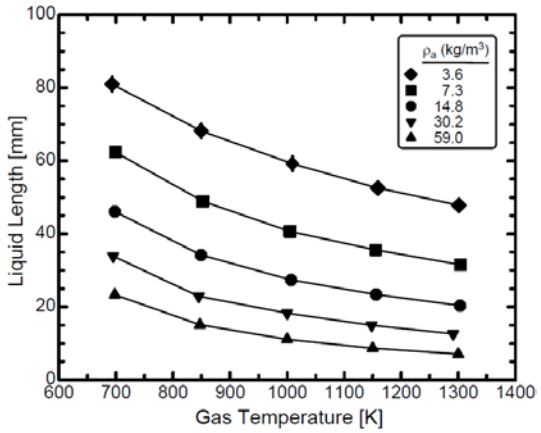

Figure 60: *Effects of ambient gas temperature and density on the liquid penetration length for heptamethylnonane* [2] *fuel at a temperature of 438 K, injected from a 0.246 mm orifice with a pressure drop of 136 MPa, taken from Siebers* [71].

The liquid penetration length stabilizes due to mixing limited vaporization. At some point downstream of the injector the energy in the amount of ambient gas entrained is enough to completely vaporize the fuel. Siebers calculated the fuel air ratio required to completely vaporize the liquid fuel based the knowledge of the initial conditions and thermodynamic properties of the fuel and ambient gas [66]. The liquid penetration length is then also affected by the volatility of the fuel, an aspect that has been examined in more detail in appendix [72].

When the fuel spray has undergone sufficient momentum exchange with the ambient, the spray/jet transitions to a regime in which it develops with self-similar scaling. In this regime the jet characteristics are governed by the ambient conditions into which it is injected. Simple modelling of the fuel jet based on self-similar scaling and momentum conservation along the diverging jet have accurately predicted the fuel air mixture field as measured with the Rayleigh scattering technique [46,73]. The dispersion angle is directly proportional to the air entrainment rate and is therefore the most influential parameter in determining the mixture field through modelling.

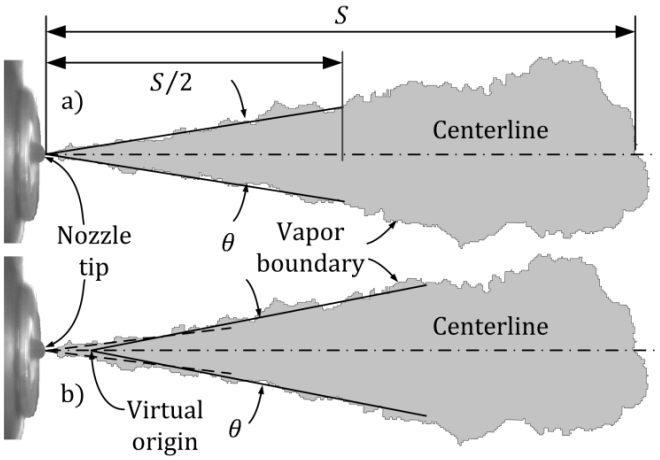

Figure 61: *a) Spray tip penetration,* ***S****, and dispersion angle,* ***θ****, of liquid fuel sprays as defined by Naber and Siebers* **[74]**. *b) Narrow dispersion angle in the spray break-up region, transitioning to wide angle in the vaporized jet region.*

Another important characteristic of the fuel spray/jet is the spray tip penetration. Naber and Siebers [74] defined the spray tip penetration, S, as the distance between the nozzle exit and the spray head at the centerline. The jet dispersion angle, θ, was defined as the angle formed by the diverging spray/jet originating from the nozzle tip to half the tip penetration distance, $S/2$. These definitions are illustrated in Figure 61 a).

Correlations have been proposed for the spray tip penetration with the consensus that $S \propto t$ in the short time limit where the spray has yet to break-up and $S \propto \sqrt{t}$ in the long time limit where the spray is vaporized [74,75]. This is shown in Figure 62 for a spray tip penetration measurement from a 0.2 mm orifice injector nozzle with $p_{\mathrm{inj}} = 1500\ bar$, into an inert ambient environment with density $\rho_{\mathrm{amb}} = 22.8\ \mathrm{kg/m^3}$ and temperature $T_{\mathrm{amb}} = 900\ \mathrm{K}$. The measurement is plotted as dimensionless penetration distance, $\tilde{S} = S/x^+$, as function of dimensionless penetration time, $\tilde{t} = t/t^+$ [74]. Where x^+ and t^+ are defined as Eqs. (50) and (51).

$$x^+ = \frac{\sqrt{C_\mathrm{a}} d_0 \sqrt{\rho_f/\rho_{amb}}}{a \cdot \tan\theta/2} \tag{50}$$

$$t^+ = \frac{\sqrt{C_\mathrm{a}} d_0 \sqrt{\rho_\mathrm{f}/\rho_\mathrm{amb}}}{a \cdot \tan\theta/2 U_\mathrm{f}} \tag{51}$$

$$U_\mathrm{f} = \frac{C_\mathrm{d}}{C_\mathrm{a}} \sqrt{2 \frac{(p_\mathrm{f} - p_\mathrm{amb})}{\rho_\mathrm{f}}} \tag{52}$$

C_a and C_d are the area contraction coefficient and discharge coefficient respectively. These quantities can be measured according to [76].

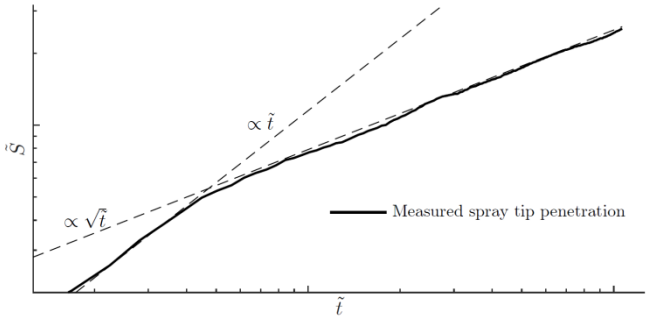

Figure 62: *Spray tip penetration measurement of 0.2 mm orifice injector (spray D) showing the dimensionless penetration distance, S̃, as a function of the dimensionless penetration time, t̃. The spray tip penetration is proportional to t̃ in the short time limit and proportional to t̃ in the long time limit.*

Recent investigations [46,73,66] have however found that a dispersion angle narrower than the measured jet dispersion angle, with the definition by Naber and Siebers [74] Figure 61 a), in the near nozzle region is needed in order to match mixing limited liquid penetration distances with liquid length measurements. This has been observed in several experimental investigations as well [46,57,77,66]. Siebers found that a coefficient of 0.66 for the measured dispersion angle matched the mixing limited liquid penetration predictions with experiments for selected fuels [66]. Pickett et. al. [46] found that the transition to a wider dispersion angle was pushed further upstream as the ambient density increased, confining the effects of break-up and evaporation closer to the nozzle. The author believes this to be a

consequence of the break-up and evaporation characteristics [78]. The dispersion angle may be misinterpreted if a constant angle is defined with the nozzle as point of origin. Thus, the definition of the dispersion angle may be discussed, as there will always be a break-up zone where the effects from the initial injection conditions dominate over the ambient conditions, pushing the self-similar jet further downstream or closer to the nozzle tip. A more general definition of the dispersion angle would then be the constant angle formed by the self-similar jet. The self-similar jet can then be thought of as emanating from a virtual point of origin as illustrated in Figure 61 b). Further understanding of the break-up and evaporation in the transition zone is needed in order to accurately predict the near nozzle and self-similar dispersion angles and the link between them.

Fuel spray combustion

The diesel combustion process occurs across a range of temperatures and equivalence ratios creating competing processes forming either NO_x or soot, as seen in Figure 63. In regions with high equivalence ratios, i. e. rich combustion, soot is formed. Alternatively, in regions with low equivalence ratios there is an abundance of air and flame temperatures are hot forming NO_x.

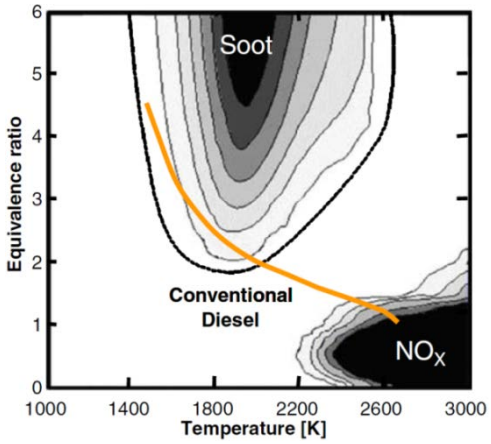

Figure 63: *Contours showing regions of soot and NO_x formation as function of fuel/air equivalence ratio and flame temperature. Also shown is the range of local conditions occurring in a conventional diesel combustion event* [79].

A conceptual description of the diesel combustion process, illustrated in Figure 64, was realized by Flynn et al [79] through numerous measurements in an optical engine. When liquid fuel is injected at high speed through an injector nozzle into quiescent surroundings, the breakup processes mentioned above form a dense spray of small droplets. The momentum of the spray causes the surrounding gas to entrain into the spray and the droplets use energy from the ambient gases to evaporate (indicated by the negative heat release prior to ignition in Figure 64 below). This process starts from the moment of injection to 4.5 CAD ASI and forms an envelope of reactive gas at the tip of the spray. At approximately 5° ASI, the fuel in the reactive mixture starts to decompose into soot precursors which in turn form poly aromatic hydrocarbons (PAHs). The decomposed fuel and air mixture auto-ignites around 6° ASI. This auto-ignition initiates a diffusion flame surrounding a pocket of excess fuel, cracked fuel and soot.

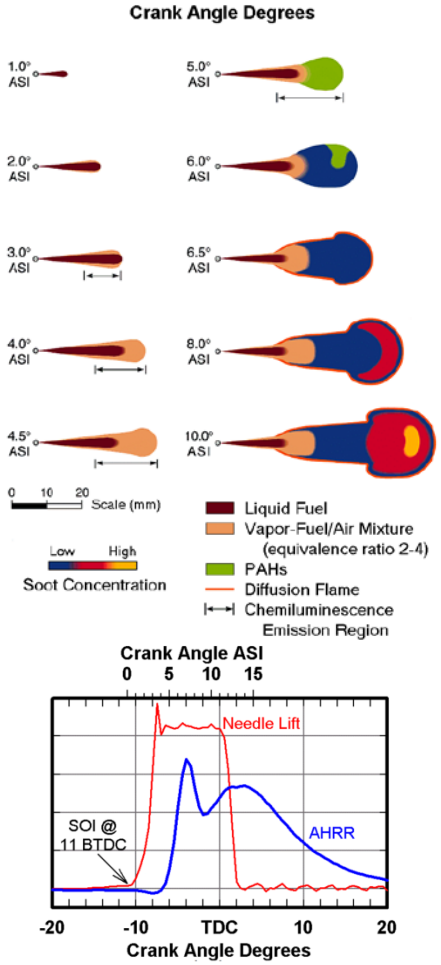

Figure 64: *Conceptual model of the Diesel combustion process from point of injection up to the development of the quasi-steady flame* [79].

A rich premixed flame stabilizes at the interface between the incoming fuel and air mixture and the pocket of hot combustion products surrounded by the diffusion flame.
At this location, the fuel/air mixture, jet velocity, turbulence, thermal diffusivity are balanced by the local reaction rate, or flame speed, such that the reaction zone, or flame, stabilizes. The distance from the nozzle to this location is known as the lift-off length. One can intuitively deduct that ambient conditions affect the lift-off length due to the effect on the laminar flame speed (chemical reaction rate) [80] while the initial injection conditions affect the local conditions in the jet.

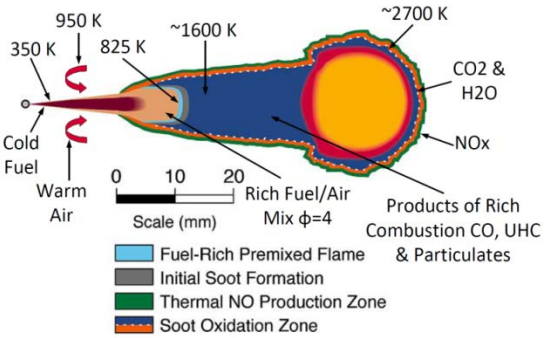

Figure 65: *Conceptual model of the quasi-steady spray flame. The flame resembles the combustion taking place the majority of the heat release duration in a CI engine* [79].

Products from the rich premixed combustion continuously feed the diffusion flame during the period in which the combustion process is said to be in a quasi-steady state (Figure 65). The quasi-steady period makes up the majority of the heat release duration.

Building upon this conceptual model, Pickett and Siebers [81] studied the soot formation near the lift-off length using different fuels and injection characteristics. They found that soot inception occurred a distance downstream of the flame lift-off location, separated by a soot precursor formation zone, consisting of gas phase species with no significant nucleation, as illustrated in Figure 66. At the lift-off location the fuel burns at a range of equivalence ratios. The fuel rich flame in the central part of the jet should then intuitively be located further downstream than the in the jet periphery where the equivalence ratio approaches 1, as also indicated in Figure 66.

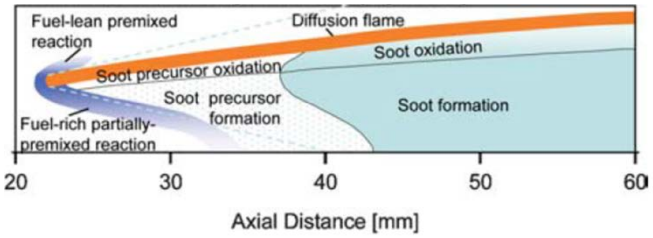

Figure 66: *Conceptual illustration of flame structure from a paraffinic hydrocarbon liquid fuel jet flame, taken from* **[81]**.

However, Skeen et. al. [82] found that formaldehyde is formed in the central part of the jet at the lift-off location that persists into the soot precursor formation zone. This indicates that oxidizing reactions occur at very high equivalence ratios in the central part of the jet. It is the author's belief that the high temperature combustion in the jet periphery at the lift-off location enhances the oxidation process in the central part of the jet, thereby forming formaldehyde.

The precursor formation zone was found to be dependent on the sooting tendency of fuel and the injection characteristics, where oxygenated fuels (with low sooting tendency) increased the separation between the lift-off location and soot inception zone compared to highly-sooting fuels. For these fuels the soot inception occurs at the edge of the jet rather than at the centerline, as is the case for oxygenated fuels. This behavior was attributed to the temperature distribution (based on adiabatic flame temperature), as soot is not formed when local temperatures are lower than 1400 K. The centerline location of temperatures exceeding 1400 K occurred upstream of soot inception for the oxygenated fuel and downstream of soot inception for the highly sooting fuel. Thereby the highly sooting fuel formed soot at the edges of the jet before the centerline, while soot inception occurred at the centerline for the oxygenated fuel. However, increased air entrainment caused the soot inception zone to occur at the centerline (not forming soot wings) even for the highly sooting fuel. These variations of the flame structure with different fuels and injection characteristics are conceptually illustrated in Figure 67.

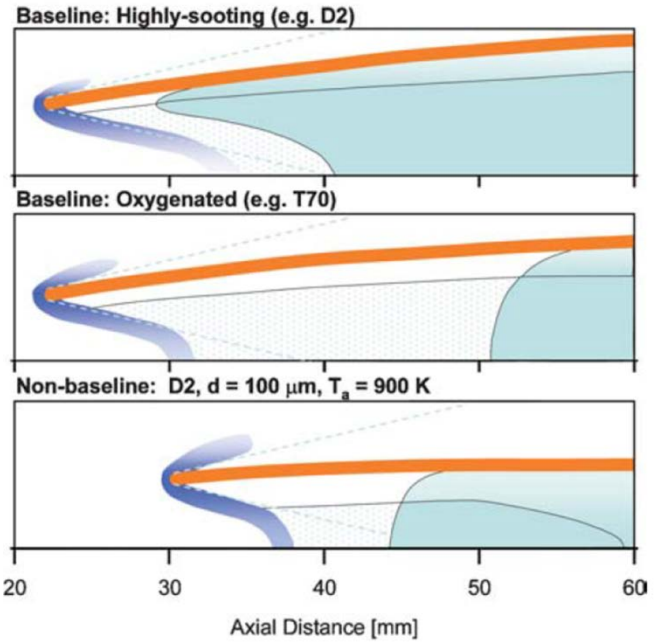

Figure 67: *Conceptual illustration of the flame structure showing the effects of the fuel's sooting tendency and the spray characteristics* **[81]**.

Motivations for choice of diagnostics

We have seen examples of various baseline optical combustion diagnostics and built up a fundamental understanding of two phase atomizing reacting sprays. In this section the motivation for the choice of diagnostic are drawn based on the limitations that arise in the reacting spray application. For instance, an injection event in a DI CI engine spans on the order of milliseconds and is injected into an environment with sufficiently high pressure and temperature such that the fuel auto ignites. The extremely high temporal resolution required to capture/freeze transient behavior in these spray flames and the optically harsh environments into which they are injected poses significant requirements to the optical diagnostics.

As the spray flames are transient, spatial information is of great important. It is therefore beneficial to use imaging techniques. The high temporal resolution requirement restricts optical methods to the visible and UV part of the spectrum, as infra-red sensors are relatively slow in comparison.

Schlieren and extinction imaging are chosen to measure the vapor and liquid boundaries of the spray/jet. In addition to determining the vapor penetration and jet dispersion, the vapor boundaries deducted from schlieren imaging can be used to estimate the mixture field through the simple steady jet model by Musculus and Kattke [73] as Pickett et. al. [46] found that the model matched well with Rayleigh scattering measurements. Schlieren imaging offers greater experimental simplicity and is not limited to non-reacting conditions compared to the Rayleigh scattering technique. In addition, high intensity lasers are limited to low pulse repetition rates limited to a single shot per injection event, requiring multiple experiments to achieve statistical convergence. The measurement of the liquid boundary gives insight into the spray break-up characteristics and can be used to evaluate the jet model based on mixing limited vaporization. DBI imaging of the liquid phase in combination with schlieren imaging of the vapor phase gives a complete image of the spray/jet.

Regarding soot, extinction imaging has in recent years become of great interest in spray applications. Only few applications of PLII have been successfully used with automotive fuel spray flames under engine relevant conditions [83,84] due to challenges arising with increased flame opacity. The laser is absorbed to such a degree that the energy becomes too low to induce a sufficient incandescence of the entire soot cloud, and increasing the laser fluence will lead to particle sublimation. The dense soot cloud also induces significant trapping of the incandescence signal. Recent advances in LED and driver technology [85] have given the LED laser like properties at a fraction of the cost. These LEDs are ideal for application in extinction imaging with high temporal resolution. The ability to spatially resolve extinction measurements in transient flames and the vast amounts of information that can be deducted from such measurements makes the technique very attractive. However, imaging through environments with high temperature and pressure with high temporal resolution has posed significant challenges to the diagnostic. A major part of this work has been to develop an optical arrangement able to image extinction under these conditions. The diagnostic is to be introduced as a standard measurement technique within the ECN community. The design of the optical setup is detailed in the next sections and in [86].

The level of detail that LIF of trace species in the flame offers is beyond the scope of this investigation. Studying the flame structure through LIF targeting of minor species is a large PhD topic on its own. Chemiluminescence imaging of OH^* is more than sufficient for evaluating the flame structure in this study.

Thermometry based on spectroscopy in the visual part of the spectrum would have been desired. However, the experimental campaign carried out at Sandia national labs was aimed at specifically isolating the effects of in-nozzle cavitation on the resulting spray/jet and combustion characteristics and did not call for such measurements. In addition, limited time leaves these measurements up to future work. These measurements are however based on spectral extinction data recorded with an imaging spectrometer and thus suffer the same limitations as extinction imaging. The findings in this work regarding the optimal optical arrangement of extinction imaging are applicable in future thermometry measurements via an imaging spectrometer.

Optical setup for extinction imaging via Diffused Back-illumination

Extinction-based measurements are sensitive to variations in the refractive index along the optical path, often referred to as “beam-steering”. Beam steering may be perceived as attenuation during post processing, when in fact light is being steered in/out of the aperture of the collection optics. This “perceived” attenuation is hard to distinguish from attenuation by scattering/absorption. Extinction measurements performed using a laser increase the acceptance angle of the collection optics in order to accommodate steering of the laser beam [41]. Extinction-imaging applies diffused back lighting to accommodate beam steering effects. It can be shown that with back-illumination of a certain character, only attenuation by absorption and scattering will be imaged.

Theoretical approach to evaluate the role of diffused back light in an extinction imaging application

The concept of the light extinction setup is illustrated in Figure 68 a), where only the light collection to a single pixel is shown. The marginal rays that are traced in the illustration are defined by the angular aperture of the camera objective. The marginal rays define the acceptance cone of the particular collection system to the particular pixel. The acceptance cone is assumed to be rotationally symmetric around the chief ray. A unit sphere is illustrated around the focal point to show the solid angle of the acceptance cone. The acceptance cone on the opposite side of the focal point is collecting light from an extended, homogenous and planar light source.

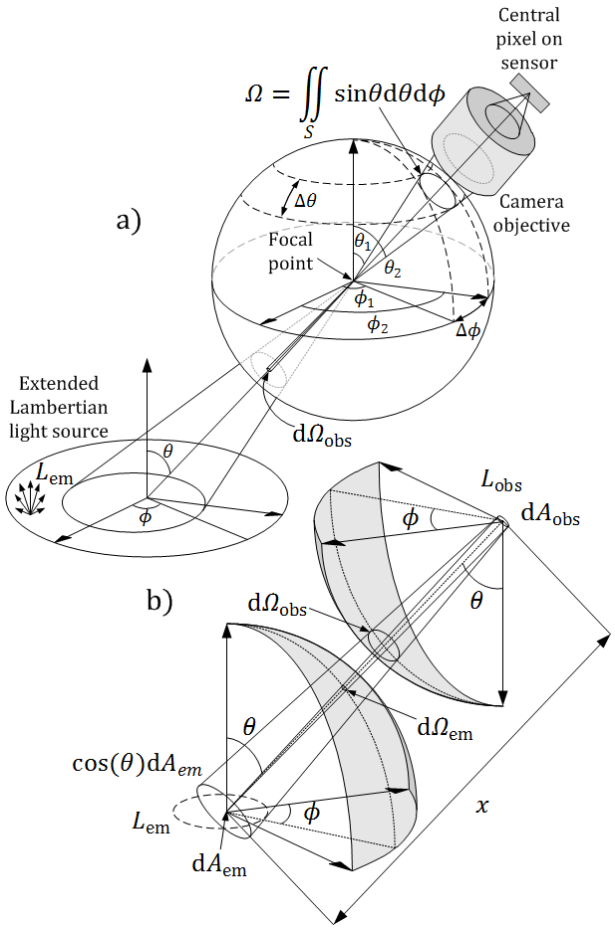

Figure 68: *Illustration of irradiance quantified through the focal point of one pixel from an extended light source with constant radiance subtended by the solid angle, Ω, of the camera objective. Also illustrated is the radiant exchange between an infinitesimal area in the focal point and an infinitesimal area on the source.*

Figure 68 b) shows a single ray within the acceptance cone to illustrate the relation between radiant flux observed, $\mathrm{d}\Phi_{obs}$, by a small area, $\mathrm{d}A_{obs}$, in the focal point and radiant flux emitted, $\mathrm{d}\Phi_{em}$, from a small area, $\mathrm{d}A_{em}$, on the light source. A unit sphere is also illustrated around the center of $\mathrm{d}A_{em}$ to show the solid angle of light subtended by $\mathrm{d}A_{obs}$. The radiance, $L_{em}(\theta)$ [W/(m²sr)], emitted by the projected area $\cos(\theta)\mathrm{d}A_{em}$ of the light source within the solid angle $\mathrm{d}\Omega_{em}$ is defined as Eq. (53).

$$L_{em}(\theta) = \frac{\mathrm{d}^2\Phi_{em}}{\cos(\theta)\mathrm{d}A_{em}\mathrm{d}\Omega_{em}} \tag{53}$$

The radiance, $L_{obs}(\theta)$, observed by the area $\mathrm{d}A_{obs}$ within the solid angle $\mathrm{d}\Omega_{obs}$ is defined as Eq. (54).

$$L_{obs}(\theta) = \frac{\mathrm{d}^2\Phi_{obs}}{\mathrm{d}A_{obs}\mathrm{d}\Omega_{obs}} \tag{54}$$

Since $\mathrm{d}\Omega_{em}$ is subtended by $\mathrm{d}A_{obs}$ and $\mathrm{d}\Omega_{obs}$ by $\mathrm{d}A_{em}$ the solid angles depend upon the distance, x, through Eq. (55) and (56).

$$\cos(\theta)\,\mathrm{d}A_{em} = x^2\mathrm{d}\Omega_{obs} \tag{55}$$

$$\mathrm{d}A_{obs} = x^2\mathrm{d}\Omega_{em} \tag{56}$$

These relations are easier understood from the illustration in Figure 68 b), where $\mathrm{d}\Omega_{em}$ and $\mathrm{d}\Omega_{obs}$ are shown as projections of $\mathrm{d}A_{obs}$ and $\mathrm{d}A_{em}$ respectively on the opposed unit sphere. In a lossless environment, energy conservation implies that $\Phi_{em} = \Phi_{obs}$. Inserting Eq. (55) and Eq. (56) into Eq. (53), substituting Φ_{em} with Φ_{obs} and integrating with respect to $\mathrm{d}\Omega_{obs}$, leads to an expression for irradiance, $E = \mathrm{d}\Phi/\mathrm{d}A$ [Wm^{-2}] (Eq. (57)). Note that the observed irradiance is based on the radiance emitted by the extended source and independent of the distance, x.

$$\frac{\mathrm{d}\Phi_{obs}}{\mathrm{d}A_{obs}} = \int_{\Omega_{obs}} L_{em}(\theta)\,\mathrm{d}\Omega_{obs} \tag{57}$$

The irradiance is a useful quantity because the cross section area at the focal point in Figure 68 a) is small and may be considered as $\Delta A_{obs} = \mathrm{d}A_{obs}$. The size of ΔA_{obs} is eventually determined by the camera objective and the pixel size, and may thus be considered as a fixed value during the measurements. The radiant flux arriving on the pixel in Figure 68 a) will, according to Eq. (55) and Eq. (56), be independent of the distance, x, between the camera and the source, if the light source is extended and spatially homogeneous with a fixed angular radiance profile.
Furthermore, if the light source is Lambertian, meaning that radiance is independent of viewing angle, it follows that Eq. (57) may be reduced to Eq. (58) and (59). This states that the radiant flux detected by a pixel is also independent of the viewing angle relative to the light source and only depends on the angular aperture of the camera objective and the radiance emitted by the source [87,10].

$$\frac{\mathrm{d}\Phi_{obs}}{\mathrm{d}A_{obs}} = L_{em}\Omega_{obs} \tag{58}$$

$$\Phi_{obs} = L_{em}\Omega_{obs}A_{obs} \tag{59}$$

These conclusions suggest that the detected signal will not depend upon refraction of rays, as it, in many cases, just will appear like moving or tilting the light source. This is however only conditionally true. The above theory serves to couple the observed solid angle and area with the emitted radiance to show that the observed radiant flux only depends on those boundary conditions. A change of refractive index, n, between the boundary conditions was ignored. However, using the Lagrange invariant it may be shown that energy conservation requires that etendue, $n^2\Omega A$, and the basic radiance $L^* = L/n^2$ (can be interpreted as the radiance in a vacuum) both are constant along a ray of light. Therefore, Eq. (58) and (59) still apply despite refraction between the boundaries. At the boundaries, however, conditions are determined by a light source and a camera with an objective lens. These are real optical systems limiting the etendue by light restrictions due to physical sizes of optics and apertures. Etendue, and thus radiant flux through real optical systems, depend on the refractive index in the systems and should therefore be kept constant during measurements. The requirement of maintaining a constant refractive index at the boundaries is easily achieved in the practical setup. As long as the light source and camera are immersed in a medium with

constant refractive index during the measurement, the etendue will remain constant.
The major refractive effects that can be encountered during extinction imaging measurements can be reduced to three essential interactions. Rays passing through a parallel faced a), non-parallel faced b) and a non-planar c) refracting media. The following illustrations are based on sequential ray tracing of the marginal and chief rays of light collected by a specific pixel on the imaging sensor. For visual simplicity, the illustrations are in 2D with the acceptance cone being rotationally symmetric around the chief ray, with Ω_{obs}, θ and A_{obs} being the solid angle, viewing angle and the area of the projected pixel of the un-refracted acceptance cone. The prime denotes the same parameters belonging to the refracted acceptance cone.

a) Figure 69 shows rays traced through a parallel faced refracting media. It is seen that the acceptance cone that collects light from the source may be translated spatially in any of the x, y and z direction depending on the orientation of the refracting media. The light collection system will effectively collect a different bundle of rays from the source than in the un-refracted case. However, all the parameter remain unchanged, $\theta = \theta'$, $\Omega_{\text{obs}} = \Omega'_{\text{obs}}$ and $A_{\text{obs}} = A'_{\text{obs}}$. As long as the size of the source is large enough and the radiance is spatially homogenous with a fixed angular distribution, then the radiant flux received by the pixel will remain unchanged.

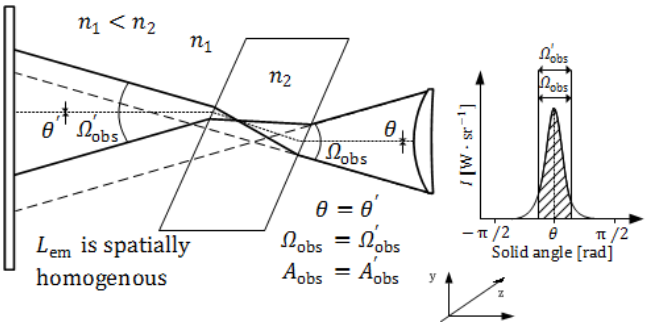

Figure 69: *Illustration of acceptance cones collecting light to a specific pixel on an imaging sensor. Chief and marginal rays are traced through a parallel faced refracting media. The solid lines trace the refracted marginal rays, the dashed lines the un-refracted marginal rays and the dotted line shows the refracted chief ray. The plot to the right illustrates the angular distribution of radiant intensity, which is Gaussian to illustrate that this particular case of refraction does not require a Lambertian distribution. The shaded area represents the irradiance received by the pixel Eq.(57).*

b) It is seen in Figure 70 that non-parallel faced refracting media not only translates the refracted acceptance cone but also rotates it. This is illustrated by the viewing angle θ' no longer being perpendicular to the source. The solid angle and projected pixel area of the refracted acceptance cone remain unaltered, $\Omega_{\text{obs}} = \Omega'_{\text{obs}}$ and $A_{\text{obs}} = A'_{\text{obs}}$. Requirements to the size and homogeneity of the source still apply. However, the altered viewing angled, $\theta \neq \theta'$, adds the requirement that the angular distribution of radiance from the source should be uniform (Lambertian) to avoid that the refracting media influence the radiant flux received by the specific pixel (Eq. (58)).

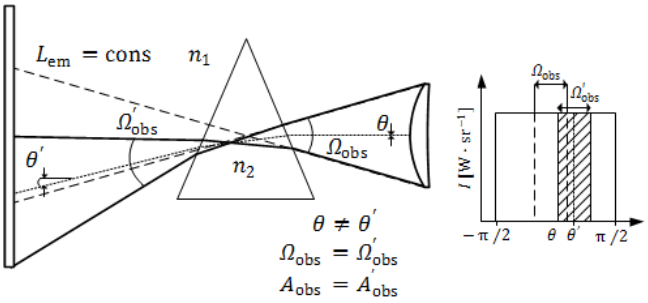

Figure 70: *Illustration of acceptance cones collecting light to a specific pixel on an imaging sensor. Chief and marginal rays are traced through a non-parallel faced refracting media. The angular distribution of emitted radiant intensity is uniform (Lambertian) and is shown as a white box in the plot to the right. The shaded box shows the radiant intensity that is collected from the source. The illustration is formatted in the same manner as Figure 69 .*

c) Through a refracting media with non-planar surfaces may not only translation and rotation of the refracted acceptance cone occur, but the solid angle of the cone may also be altered, $\Omega_{\text{obs}} \neq \Omega'_{\text{obs}}$ (Figure 71).

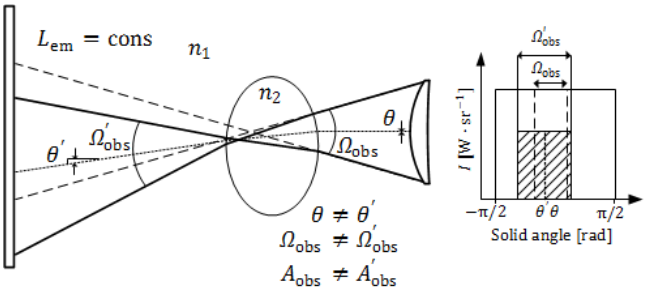

Figure 71: *Illustration of acceptance cones collecting light to a specific pixel. Chief and marginal rays are traced through a refracting media with non-planar surfaces. The illustration is formatted in the same manner as Figure 69.*

Equation (60) follows from $n^2 \Omega A = \text{Cons}$ and the refractive index next to both light source and light collection system being identical (n_1) showing that A'_{obs} has been magnified by M^2 compared to A_{obs}.

$$\frac{A_{\text{obs}}}{A'_{\text{obs}}} = \frac{\Omega'_{\text{obs}}}{\Omega_{\text{obs}}} = M^2 \qquad (60)$$

Thus as long as Ω_{obs}, A_{obs} and n_1 are kept constant for the acceptance cone at the boundary toward the light collection side, then etendue is also constant. This, and assumption of an ideal optical system between the boundaries, implies that etendue of the un-refracted acceptance cone $n_1^2 \Omega_{\text{obs}} A_{\text{obs}}$ at the light source is equal to that of the refracted acceptance cone $n_1^2 \Omega'_{\text{obs}} A'_{\text{obs}}$. If also L_{em} is kept constant, it may be seen with Eq. (59) that $\Phi_{\text{obs}} = \Phi'_{\text{obs}}$. Thus, non-parallel refracting media will not alter the detected radiant flux.
In summation, in order to counteract translation, rotation and altered solid angle of the acceptance cone from refraction interactions, the criteria for the illumination source are 1) the source should be sufficiently extended

beyond the field of view of the pixel and 2) the source should have constant radiance.

Dimensioning setup for high light throughput

Achieving these lighting characteristics while still maintaining a high light throughput (promoting high temporal resolution capabilities), involves dimensioning the size and radiance of the source according to the collection optics as shown in Figure 72.

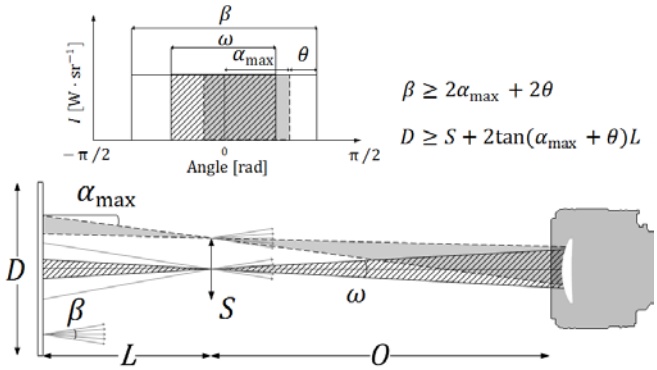

Figure 72: *Dimensioning of engineered diffuser size D and angular scattering of Θ, according to collection optics. Illumination effectively eliminates beam steering of magnitude 2θ and is optimized for light throughput.*

It was desired to use LEDs as the illumination source due to their monochromatic nature and the ability to generate short pulses of extreme intensity via drivers engineered at Sandia [88]. This gives the LED laser like properties. Following the recommendations and dimensioning considerations from [86], the optical arrangement in Figure 73 was arrived at and used in the DBI extinction imaging measurements.

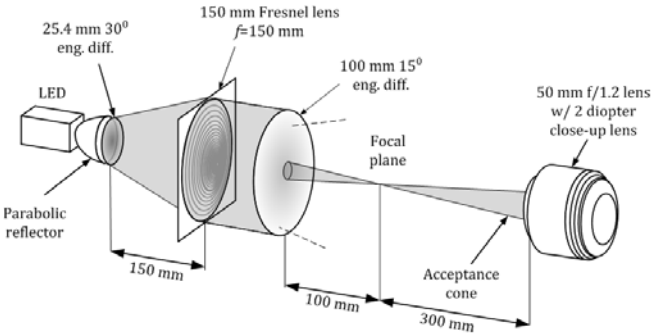

Figure 73: *Optical arrangement for DBI extinction imaging dimensioned according to* **[86]**, *employing high intensity pulsing LED.*

The LED illumination was directed forward with a parabolic reflector. A small engineered diffuser homogenized the illumination and expanded the beam to a Fresnel lens, collimating the light to a custom made large area diffuser of $D = 100$ mm and 15° angular scattering profile. The collection optics consisted of a 50 mm f/1.2 objective equipped with a 2 diopter close-up lens.

Performance of the optical setup

Early studies of soot in fuel sprays under high ambient pressure and temperature have used laser extinction and PLII [84,89,52]. Previous applications of extinction imaging of these fuel sprays have applied an optical arrangement inspired by the Ghandhi and Heim setup [90], with the goal of maximizing the light throughput. The lighting however, was difficult to characterize and the measurements displayed significant beam-steering artifacts Figure 74 (above). Shorter wavelengths of illumination helped (400-550nm) increasing the contrast between the light extinction by soot and beam-steering as the soot appears optically thicker at these wavelengths [91,15]. The benefit of using well-defined diffused back illumination in extinction imaging of soot can be seen in Figure 74 (below) where the "schlieren like" artifacts introduced by beam-steering are suppressed.

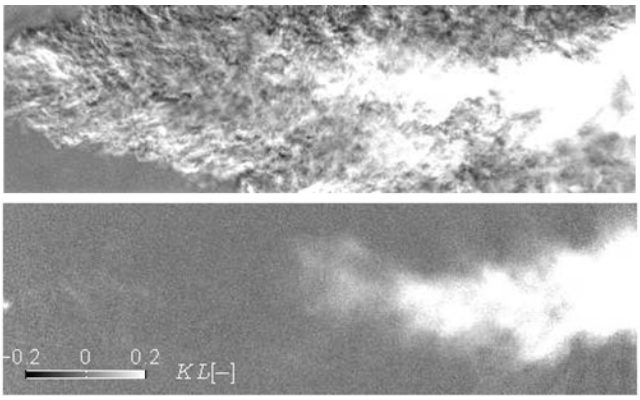

Figure 74: *Instantaneous KL images of moderately sooting flame in a high pressure and temperature environment without improvements (above) and after improvements (below) to the lighting characteristics. The above image was acquired using an optical inspired by Ghandhi and Heim* [90] *setup with 630nm LED and 41kHz framerate. The below image was acquired using the optical arrangement in Figure 73, following Westlye et. al.* [86] *setup with 630nm LED and 45kHz framerate.*

The DBI extinction imaging technique has also been used in determining the liquid penetraiton length of fuel sprays into high pressure and temperature ambient [92,93]. The most widely used method of detemrminning the liquid penetration has been imaging of mie scatter from the liquid droplets perpendicular to the illumination [71]. This technique however, applies a threshold on an absolute signal whereas a measurement normalized to a reference illumination is more useful when comparing data between institutions. The extinction imaging technique benefits in this respect. These measurements are however also suceptible to beam-steerig from the dense vapor phase in the jet. A comparison of extinction images of the liquid phase of the spray can be seen in Figure 75 using a), the setup inspired by Ghandhi and Heim and b), the optical arrangement seen in Figure 73.

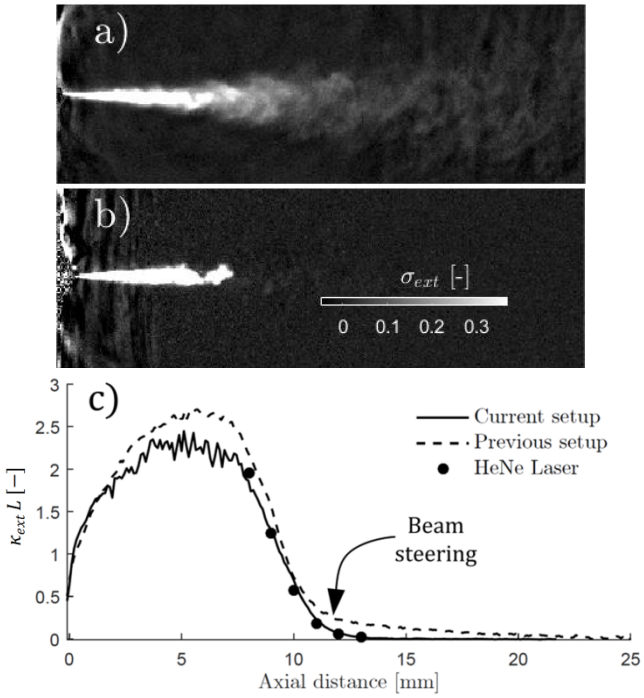

Figure 75: *Comparison of liquid penetration measurements with the same injector under identical conditions via DBI, a) using the previous optical setup inspired by the Ghandhi and Heim setup* [90] *and b) using the current optical setup. Also shown in c), is the centerline extinction profile along the spray axis for both setups. HeNe extinction measurements, fully accounting for beam-steering, are also included in the plot.*

It can be seen in the quasi steady averaged centerline profile of the optical thickness using the current imaging setup agrees very well with laser extinction measurements that fully account for beam-steering. The effect of the beam-steering from the dense vapor phase causes the extinction profile trail-off downstream never reaching 0. This caused uncertainty in the determination of the liquid-length as the recommended threshold ($KL = 0.37$ corresponding to threshold applied in Mie scattering measurements [92]) is in the range where beam-steering effects are not insignificant. An approach of slope fitting the centerline profile was then adopted instead [93]. With the current optical setup the threshold can be applied directly to the snapshots of the optical thickness.

Experimental methods

The experimental work has been done in the combustion research facilities at Sandia National Laboratories in Livermore, California. Sandia has a long tradition for pioneering engine combustion research and have state of the art facilities [94]. The research has been part of the ECN [2] focusing on experimental methods for high speed imaging measurements of diesel engine like fuel spray flames and comparing sprays from cavitating and non-cavitating fuel injectors.

Experimental facility: Sandia constant volume combustion vessel

A wide range of ambient environments in which to inject a liquid fuel spray can be generated in a constant volume combustion vessel with a high degree of reproducibility. This allows the effect of multiple variables to be isolated and assessed. In this work, all experiments involving fuel sprays have been conducted in the constant volume combustion vessel at the Sandia CRF (Figure 76). A brief mention of the vessel and operation is given here, further details can be found in [2].

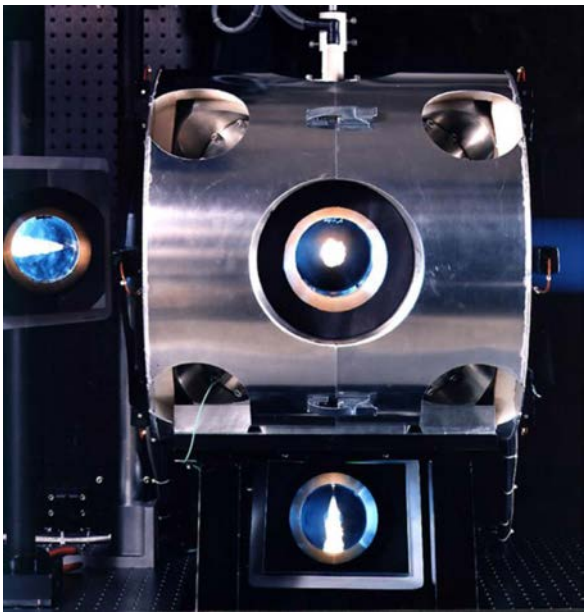

Figure 76: *Photo of Sandia's constant volume combustion vessel. 45° mirrors show the optical access windows and a side view of the fuel spray.*

The combustion chamber is cubical shaped with a characteristic dimension of 108 mm. Each side of the cube has circular ports with diameter of 105 mm. One of the ports is fitted with the injector and another with spark plugs. Circular sapphire optical access windows with a clear aperture of 102 mm and thickness of 17 mm are held in the circular remaining ports of the chamber with window retainers. This enables four optical access points and the possibility for dual line of sight access.
The range and ambient conditions that may be varied in the vessel are noted in Table 2.

Table 2: *Adjustable parameters for generating specific ambient environments in the combustion vessel.*

Parameter	Range
T_{amb} [K]	450-1300
ρ_{amb} [kg/m^3]	3-60
x_{O_2} [−]	0-0.21

The procedure for reaching the desired ambient conditions is shown in Figure 77 where the combustion chamber is pressurized to a specific density with a combustible mixture of gases.

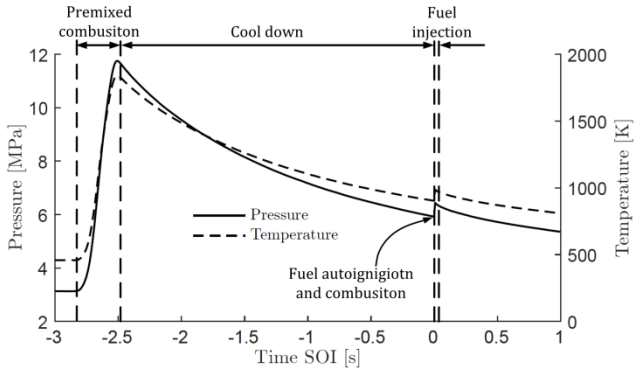

Figure 77: *Example of pressure trace and core temperature curves for generating core ambient conditions of* $T_{\mathrm{amb}} = 900$ K, $\rho_{\mathrm{amb}} = 22.8$ kg/m^3 *and* $x_{O_2} = 0.21$.

The mixture consists of acetylene (C_2H_2), hydrogen (H_2), oxygen (O_2) and nitrogen (N_2). The mixture is ignited with spark plugs and the ambient pressure and temperature increase through the premixed combustion. After a relatively long cool down period (~ 1s), the desired experimental conditions are reached and the fuel injection commences. The injected fuel vaporizes, mixes with the ambient gas and autoignites, initiating the fuel spray combustion process as seen by the second pressure rise in Figure 77.
The combustion products from the premixed flame determine x_{O_2} in the ambient during the injection event. Environments such as an inert ambient or simulated air and EGR conditions with low oxygen concentrations are generated by changing the reactant O_2 and N_2 concentrations as shown in Table 3.

Table 3: *Composition of reactants and products of the premixed combustion, in % vol, used to generate experimental environment* [2].

Products					Reactants			
O_2	N_2	CO_2	H_2O	MW	C_2H_2	H_2	O_2	N_2
21	69.3	6.11	3.56	29.5	3	0.5	28.4	68.1
20	70.3	6.13	3.57	29.4	3.01	0.5	27.4	69.1
15	75.2	6.23	3.62	29.2	3.06	0.5	22.6	73.8
10	80	6.32	3.67	29.1	3.1	0.5	17.8	78.6
5	84.9	6.42	3.72	28.9	3.15	0.5	13	83.3
0	89.7	6.52	3.77	28.7	3.2	0.5	8.25	88.1

Previously the combustible mixture used ethylene instead of acetylene. The reason for the change was to use a fuel with lower hydrogen to carbon ratio so as to reduce the water vapor content in the ambient gas after the pre-burn. The higher water content in the ambient gas promotes nozzle aging as the nozzle tip is exposed to the water containing ambient gas at temperatures and durations which never occur in a diesel engine. This causes surface aging which alter the spray characteristics causing shorter liquid penetration lengths and lower spray momentum

consequently altering the lift-off location and sooting characteristics [95],
The temperature in the combustion vessel is lower close to the walls and higher in the core of the chamber. To account for this the core temperature is measured using fine thermo-couples with adequate response time. The core temperature, T_c, is related to an estimation of the bulk temperature, T_b, through Eq. (61). The bulk temperature is estimated through the real-gas equation of state using the measured pressure trace p, the mass averaged bulk density ρ_b and the compressibility factor Z (Eq. (62)).

$$\frac{T_c}{T_b} = 1 + a\left(1 - \frac{T_w}{T_b}\right) + b\left(\frac{T_b}{T_w} - 1\right) \quad (61)$$

$$p = \frac{ZR\rho_b T_b}{M} \quad (62)$$

Values for a and b in Eq. (61) have been determined from an empirical fit to the average measured temperature for many cool-down events at given ambient gas density [2].
The fuel is injected with a common-rail fuel injection system at injection pressures ranging from 40 to 200 MPa. A range of nozzles and fuels can be tested with this system. The fuel used in the current experiments was n-dodecane with properties listed in Table 4.

Table 4: *Fuel properties for n-dodecane.*

T_{boil} [K]	489
Cetane number [-]	87
$\Delta H°$ [MJ/kg]	44.17
ρ @ 288 K [kg/m^3]	752.1
y_{H_2} [−]	0.153
ν @ 253 K [mm^2/s]	4.7
ν @ 313 K [mm^2/s]	1.5
T_{freeze} [K]	263
T_{flash} [K]	356
Refractive index (n)	1.422

The naming system for denoting measurement conditions follows the sorting code in Table 5. For example, the standard Spray A conditions are $x_{O_2} = 0.15$, $T_c = 900$ K, $\rho_{amb} = 22.8$ kg · m^{-3}, $p_{amb} = 150$ MPa and orifice diameter of 90 µm which will be denoted JKLDN.

Table 5: *Naming convention for spray measurements conducted in the Sandia combustion vessel.*

	x_{O_2}	T_c [K]	ρ_{amb} [kg/m^3]	p_{inj} [MPa]	Orifice [mm]
A	0.21	1400	3.57	140	0.254
B	0.0	1350	7.27	180	0.178
C		1300	14.8	185	0.246
D		1250	30	**150**	0.254
E	0.21	1200	58.5	110	0.363
F	0.19	1150	45	100	0.497
G		1100	123.8	90	0.1
H	0.17	1050	247.6	70	0.18
I		1000		60	0.267
J	**0.15**	950		35	0.254
K		**900**		40	0.18
L		850	**22.8**	80	0.11
M	0.12	800	18.8	100	
N		750	11.8	190	**0.09**
O	0.10	700		200	
P		650		120	
Q	0.8	600		10	
R					
S	0.5		24.3		0.05
T			1.25		0.05
U			2		
V			3		

Diagnostic considerations in combustion vessel environment

The refractive index of the sapphire windows providing optical access is affected by the temperature. This alters the spectral transmission which is an important aspect with regards to quantitative optical measurements. Absorption by various products from combustion can also interfere with certain measurements. As we confine ourselves to the UV-visible spectral range, absorption PAH's may become an issue. Many PAH's absorb UV radiation. A larger concern, however, is NO_2. The absorption cross-section of NO_2, seen in Figure 78 at atmospheric conditions, is large and spectrally broad, ranging from the UV and extending to the visible [96].

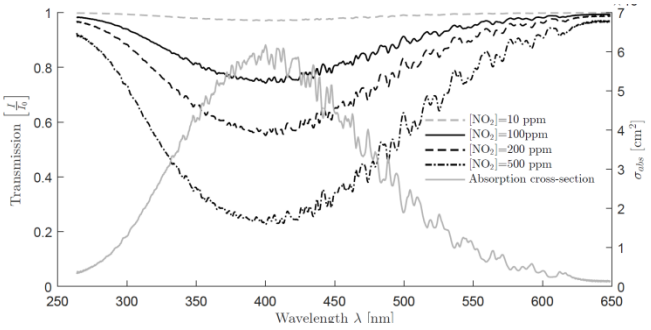

Figure 78: *Spectral transmission through 0.1 m gas containing 10, 100, 200 and 500 ppm NO_2 under typical conditions during an injection event in the combustion chamber ($T_{amb} = 900$ K and $\rho_{amb} = 22.8$ kg/m^3). The spectral transmission is based on measured absorption cross-section of 1 ppb NO_2 at $T = 298$, $p = 1$ atm* **[96]** *and is translated to the ambient conditions through Eq. (7).*

The absorption cross-section at atmospheric conditions has been translated into transmission under conditions resembling the ambient in the chamber through 0.1m optical path with Eq. (7). This is a very crude extrapolation, omitting broadening and hot lines, but shows how even trace amounts of NO_2 can potentially result in significant light losses. This was experienced first-hand when performing extinction imaging at incident wavelength of 400 nm. The transmission through the bulk gases decreased during the cool down to only 30 % transmission at the lowest. It is believed that a contaminant with bound nitrogen, forming significant amounts of NO at low temperatures, was responsible. The NO formed then further oxidized to NO_2 during the cool down causing the drastic attenuation through the bulk gas.

Spray C and D nozzles

The injector nozzles used in this study are a part of the ECN family of injectors and have been given the names Spray C and Spray D. They have been designed with the intention of isolating the effect of in nozzle cavitation on the fuel spray characteristics. Where Spray C is a cavitating nozzle and Spray D is a non-cavitating nozzle. The specifications have been made with the goal of matching the mass flow rate and momentum flow rate between them at standard operating conditions ($p_{\mathrm{inj}} = 150$ MPa and $p_{\mathrm{b}} = 6$ MPa). A series of 5 injectors of Spray C and D have been manufactured and the geometric and hydraulic specifications of these nozzles are listed in Table 6. There is consistency within the series of injectors. However, there is a slight mismatch in the average values between Spray C and D, where Spray D has a slightly higher momentum flux and mass flow.

Table 6: *Tabulated summary of geometrical and hydraulic characterization of Spray C and D injector series with n-dodecane fuel. The injector characterization was performed with injection pressure* $p_{\mathrm{inj}} = 150$ MPa *and chamber backpressure* $p_{\mathrm{b}} = 6$ MPa **[76]**.

Injector	D_{out} [µm]	$\dot{m}_{\mathrm{nom}}$ [g/s]	m_{inj} [mg/inj]	$\dot{M}$ [N]
103D	192	11.66	50.1 ± 0.2	6.81
104D	193	11.62	49.9 ± 0.1	6.90
133D	193	11.81	53.0 ± 0.2	6.87
134D	191	1195	52.8 ± 0.2	6.91
135D	190	11.49	50.8 ± 0.2	6.61
Average	192	11.71	51.3 ± 0.2	6.82
003C	212	10.26	44.8 ± 0.2	5.75
034C	214	10.00	45.1 ± 0.3	5.60
037C	208	10.10	45.2 ± 0.2	5.66
044C	215	9.96	44.1 ± 0.3	5.66
105C	215	9.98	44.6 ± 0.2	5.59
Average	213	10.06	44.6 ± 0.2	5.65

The internal geometry of injectors 134D and 037C have been measured via x-ray computed tomography [97] for detailed characterization of the internal geometry (Figure 79) and for generating CFD grids for internal flow simulations. The grids deducted from the measurements can be seen in Figure 79 a), b) and c).

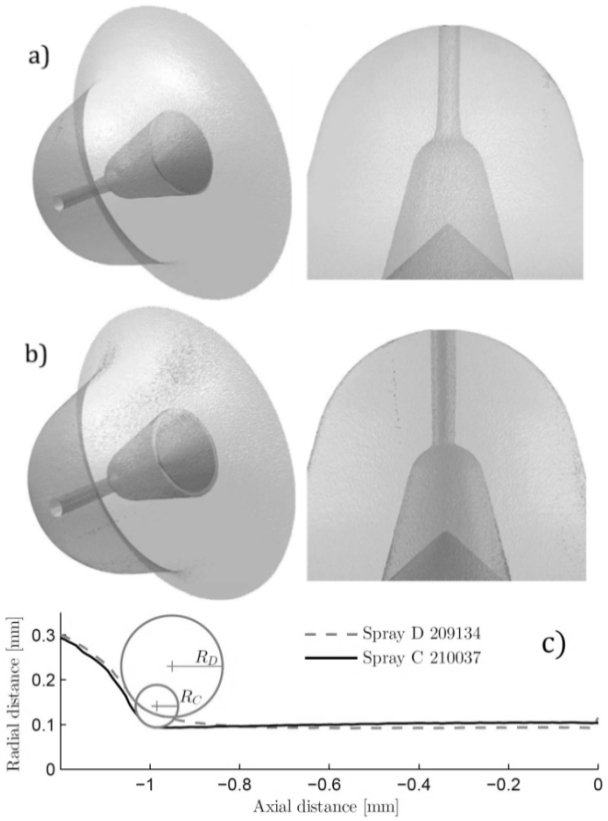

Figure 79: *Surface rendering of X-ray tomography of a) Spray D, b) Spray C internal geometry and c) 2D inlet and hole wireframe extracted from X-ray tomography with inlet radius of curvature indicated*

The data extracted from the X-ray tomography measurements of injectors 134D and 137C are summarized in Table 7, taken from [57].

Table 7: *Nominal and measured nozzle characteristics for Spray D and Spray C nozzles. The measurements have been extracted from the X-ray tomography data* **[2]** *according to* **[97]** *and from hydraulic measurements* **[76]**.

	(Spray D)	(Spray C)
Serial number	209134D	210037C
d_{nom} [µm] (specified)	186	200
d_{min} [µm] (measured)	186	187
d_{in} [µm] (measured)	193	188
d_{out} [µm] (measured)	186	208
K-factor [-] (specified)	1.5	0
K-factor [-] (measured)	0.55	-2.3
Nozzle shaping/hyroerosion	to $C_d = 0.86$	5%
$\dot{m}$ [g/s] (150 – 6 MPa)	11.96	10.12
$\dot{M}$ [N] (150 – 6 MPa)	7.13	5.83
R_x [µm] (cf. Figure 79 c))	113	48
L/D_{nom}	5.35	5
C_{d} [-] Discharge coefficient. $C_{\mathrm{d}} = \frac{\dot{m}}{\pi/4\, D_{\mathrm{min}}^2 \sqrt{2\rho_{\mathrm{f}}\Delta P}}$, where $\rho_{\mathrm{f}} = 717.9$ kg · m^{-3}@70°C and $\Delta P = 144$ MPa	0.97	0.81

Area-contraction coefficient C_a = *C_a > 1 is not physical but is most likely reflective of experimental uncertainties to derive its value	1.03*	0.89

The major difference between Spray C and D is the inlet curvature, as seen in Figure 79 c), where Spray C is sharper in order to induce cavitation. From the specs in Table 6 and Table 7 it can be seen that the criteria for matching the mass flow and momentum flux at standard operating conditions has not been met satisfactory. The measured mass and momentum flow rate is approximately 20% lower Spray C relative to Spray D. This lower flow rate is a consequence of the smaller-than-intended minimum diameter and lower flow coefficients for Spray C. In addition, it can be seen in Figure 79 c) that spray C is actually diverging with a negative K-factor as compared to the specified K-factor of 0. These differences can confound a comparison between the two injectors. However, the difference in inlet curvature promotes cavitation in Spray C and suppresses cavitation in Spray D. This is indicated in LES simulations under relevant conditions using the CFD grids of the internal geometry [57], where spray C generates significant cavitation along the walls of the injector. Also, vapor bubbles are entrained into the fuel stream, collapsing at the nozzle exit.

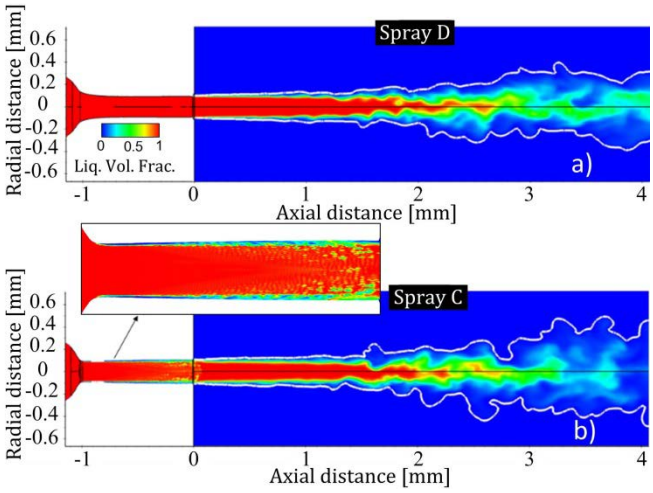

Figure 80: *LES simulations of internal flow in Spray D and C showing the tendency of cavitation in Spray C* **[57]**.

The simulations reveal that the cavitation regime resembles that of the super cavitating flow in Figure 57, where the cavitating regions extend to the exit of the nozzle and the flow along the walls is a two-phase flow.

Optical arrangements and processing methods

In this section the processing methods for the various measurements are presented. Alternative methods to processing of the measurements of the spray characteristics have been applied in the current work. The methods differ from those commonly used in the ECN community for these kinds of measurements. Motivations for the alternative approach have been that a refined DBI diagnostics was applied to measure the liquid phase penetration [86]. These measurements have been processed for direct comparison with Mie scattering measurements conducted simultaneously. The vapor phase measurements have been processed differently to facilitate a thorough comparison between the cavitating and non-cavitating nozzles. A rigorous processing procedure for the soot volume fraction measurements with the DBI diagnostic was needed due to the special way in which these measurements were acquired. In addition, as this was a new method of performing these measurements, unexpected non-idealities were bound to occur. These have been corrected in the best way possible. The origin of these non-idealities have however been identified such that the corrections applied here will not be necessary in future measurements.

Optical configuration for vapor, liquid, lift-off and ignition delay measurements

The experimental setup used in in the simultaneous measurement of vapor and liquid phase of the fuel spray is shown in Figure 81. Extended below is the setup for the OH^* chemiluminescence and luminosity based ignition delay. Further detail on the various measurements and setups can be found in [57,86].

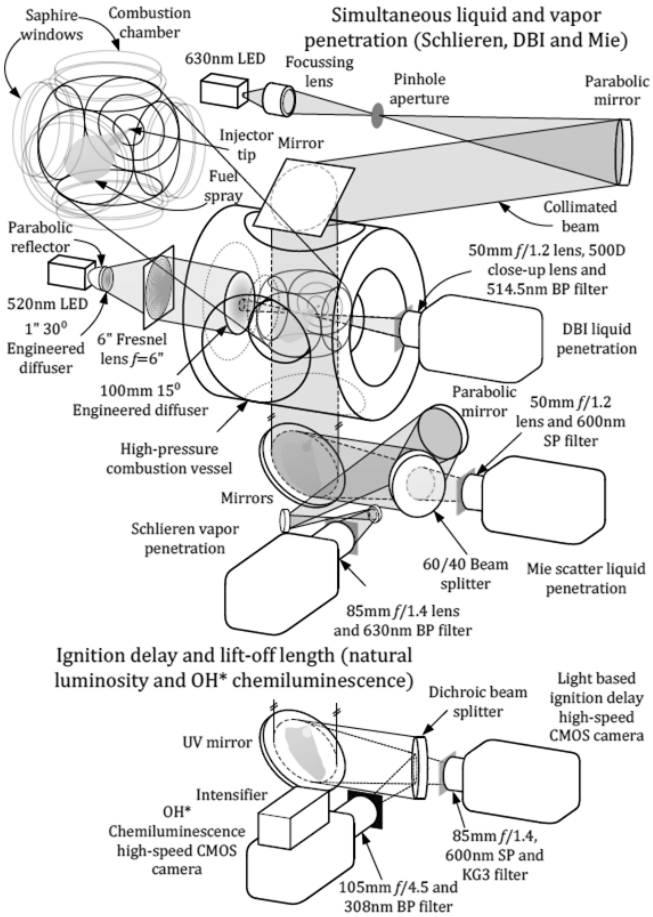

Figure 81: *Schematic of dual line of sight optical arrangement for DBI and Mie scattering liquid length and schlieren vapor penetration. Extended below is the optical arrangement for light-based ignition delay and OH* chemiluminescence measurements.*

Measuring the liquid phase

The measurement of the liquid phase is based on light extinction by scattering from liquid fuel droplets. The liquid droplets only scatter light and are otherwise transparent. Previous methods for measuring the liquid penetration

length have been based on incoherent techniques involving imaging of light scattered by the liquid phase and line of sight methods measuring the amount of light attenuated by the liquid phase. Incoherent methods have either used a laser sheet or various flood illumination schemes while imaging the light scattered perpendicularly to the illumination [71,92]. These techniques have applied a 3.1 % intensity threshold to define the liquid boundary. Through rigorous investigation, Pickett et al [92] found that this threshold translated to an optical thickness of 0.37 which corresponded roughly to 0.15 % liquid volume fraction.
In the current work extinction imaging using diffused back illumination has been used to measure the liquid phase of the spray while simultaneously imaging the scattered light perpendicularly to the DBI illumination. This has been done to evaluate the liquid phase penetration using two diagnostics and validate the DBI approach with the well-established scattering based technique. To achive instantaneous snapshots of the optical thickness, the average of 50-100 images of the reference illumination, I_0, are taken before the spray is injected. The optical thickness is then obtained with the instantaneous images, I_i, through Eq. (63).

$$\kappa_{\text{ext}}L = -\ln\left({}^{I_i}/_{I_0}\right) \tag{63}$$

With the well characterized diffused lighting, the $\kappa_{\text{ext}}L$>0.37 threshold can be applied directly to the instantaneous snapshots of the optical thickness of the liquid phase to obtain time resolved liquid boundary. Previous processing methods applied a linear slope fit on the average centerline profile in order to the determine the liquid penetration length by the intersection of the linear slope fit with 0 $\kappa_{\text{ext}}L$ [93].

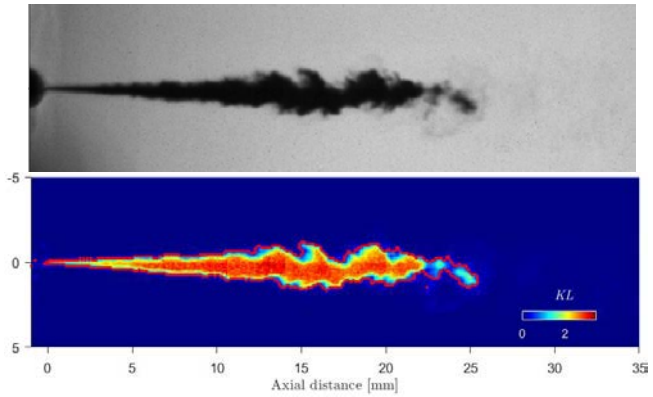

Figure 82: *(Above) Raw snapshot of DBI measurement of the liquid phase of the spray from Spray D. (Below) Map of optical thickness of the dense spray from Spray D and the processed boundary based on an optical thickness of 0.37 and liquid volume fraction 0.15 %.*

The scattering based liquid penetration measurement was captured perpendicularly to the illumination at a third of the temporal resolution, meaning the scattered light from three LED pulses was captured every frame. The signal was still quite weak and the poor signal to noise ratio made it hard to apply the stringent 3.1 % of max signal threshold. For this reason a 2D Fourier filter was applied before thresholding, filtering the higher frequencies of spatial noise.

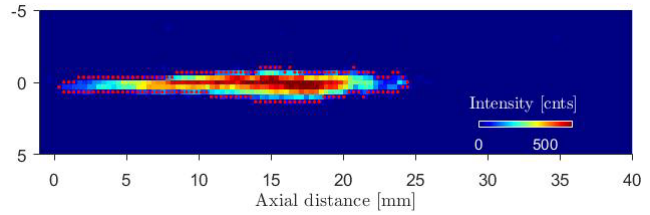

Figure 83: *Snapshot of Fourier filtered scattering based liquid phase measurement with 3.1 % of max signal threshold applied for the liquid boundary.*

It can be seen that a lot of fine details are lost in the poor spatial and temporal resolution when comparing to the Mie scatter measurements in Figure 83 to the DBI measurements in Figure 82 (below). However, a quantitative penetration length can be interpreted from the Mie scatter images.

Measuring the vapor phase

A sequence of raw schlieren images acquired during a single injection event can be seen in Figure 84.

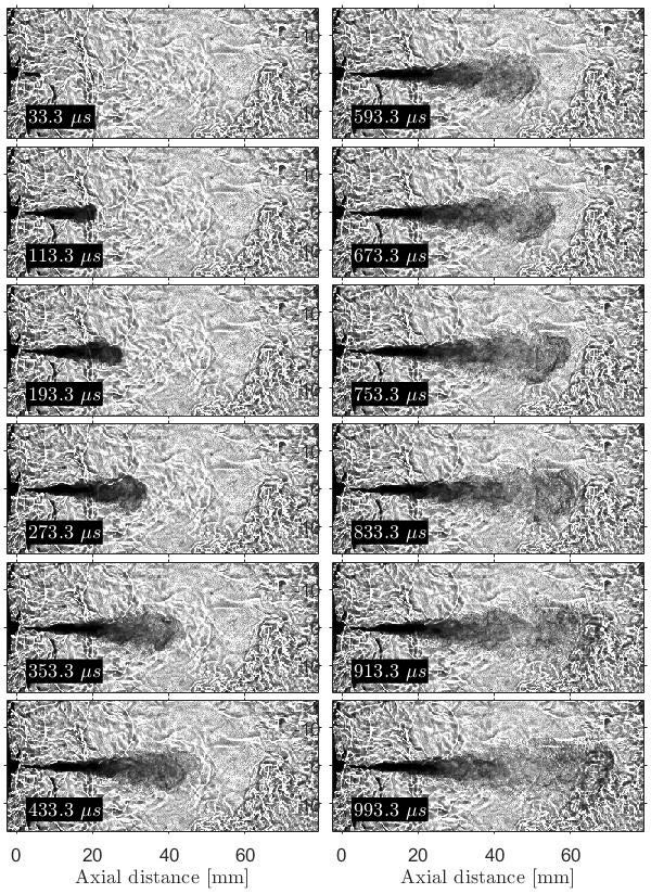

Figure 84: *Sequence of raw schlieren images of a single injection event from Spray D injector. The fuel is injected at 1500* bar *into and inert environment with* $T_{\text{amb}} = 900$ K *and* $\rho_{\text{amb}} = 22.8$ kg · m^{-3}. *The time stamp indicates the time after star of injection.*

The high temperature, high pressure and turbulent environment in the combustion vessel cause significant inhomogeneity in the refractive index which is captured by the schlieren technique, as seen by the erratic background in the image sequence in Figure 84. It can also be seen that this background is relatively slow moving compared to the spray. As the schlieren images are acquired at very high speed, the rapid spray movement can be isolated from the

relatively still environment by subtracting the previous image from the current image as seen in Figure 85 (above).

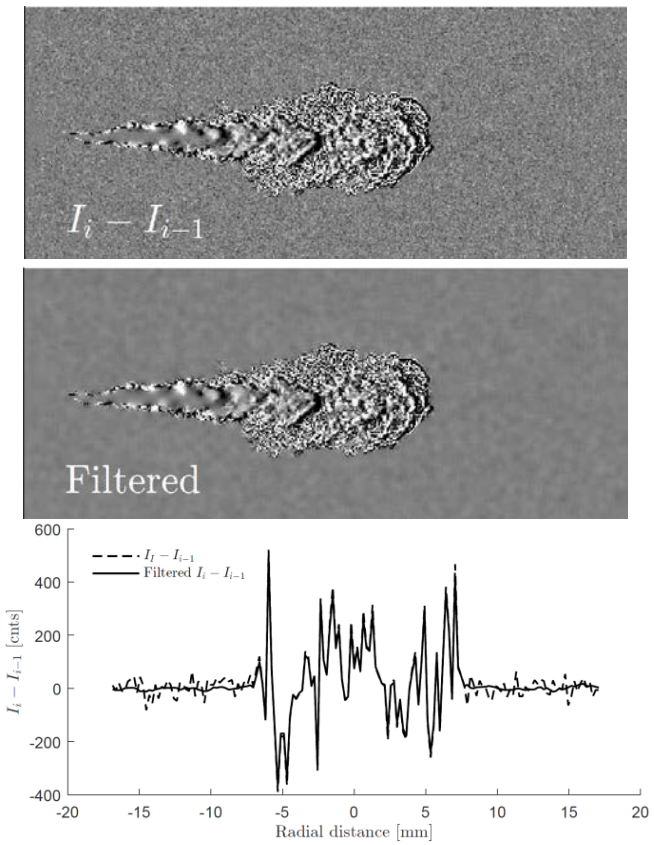

Figure 85: *(Above) Temporally differenced schlieren image. (Middle) The above image filtered with 2D adaptive Wiener Filter using background variance sampling. (Below) Radial profiles from the unfiltered and filtered temporally differenced images*

When subtracting these images from one another, the background consists of camera noise only. This noise is white and systematic which can be exploited in the filtering process. By using an adaptive 2D Wiener filter [98], targeting the variance of the background camera noise, the signal to noise ratio can be raised without sacrificing spatial resolution as seen in Figure 85 (middle and below). This allows fine detail of the vapor boundary to be captured and lowering the threshold for defining the vapor boundary, making the processing procedure more sensitive.

Previous processing methods [74] have used standard deviation filtering in combination with pixel dilation and erosion which affects the spatial resolution and may cause drift of the interpreted vapor boundary depending on the user's filtering specifications. This may consequently influence the interpretation of the dispersion angle of the sprays. An image comparing the interpreted boundaries using the two methods can be seen in Figure 86.

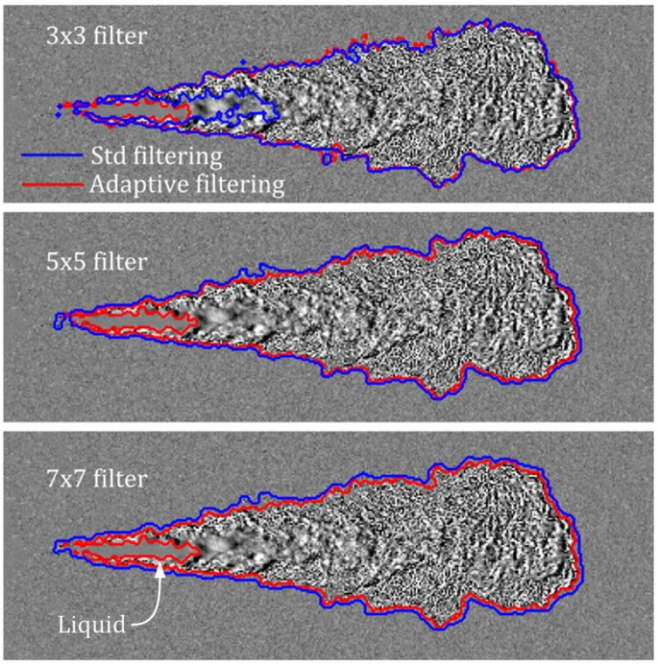

Figure 86: *Comparison of vapor boundary interpreted by means of std filtering and adaptive filtering with different filter sizes.*

It can be seen that similar vapor boundaries can be determined with both methods, however adaptive filtering is relatively insensitive to the size of the filter. The std filtering method displays degradation of the spatial resolution of the vapor boundary and appears slightly dilated around the spray as the filtering widow expands, while the vapor boundary interpreted using adaptive filtering is virtually unaffected by the filter size. These variations cause misinterpretation of the spray tip penetration and dispersion angle.

The spray tip penetration, S, is evaluated by the distance between the nozzle and the vapor boundary along the spray centerline. In order to evaluate the spray/jet boundary in the break-up zone near the injector tip, the instantaneous liquid phase boundary, measured with DBI, is scaled and used to mask the region where the liquid phase scatters the schlieren signal indicated in the lower image in Figure 86.

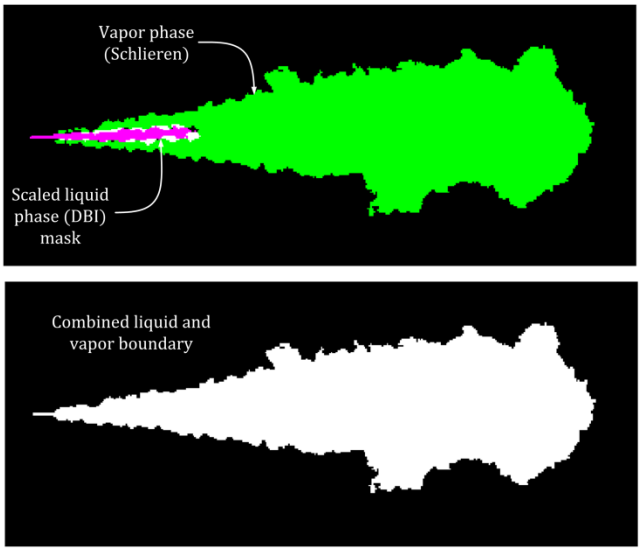

Figure 87: *(Above) Snapshot of the interpreted vapor boundary (green) with a snapshot of the liquid phase (magenta) used to mask the region where the schlieren signal is scattered. (Below) Snapshot of the spray/jet boundary interpreted from the combined snapshots of the liquid and vapor phase.*

The dispersion angle of the self-similar jet, θ, is evaluated by linear regression from the end of the break-up distance to around 30 mm downstream of the break-up length as seen in Figure 88.

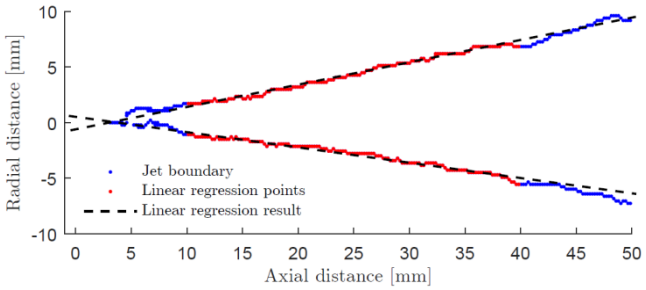

Figure 88: *Interpreted dispersion angle from averaged vapor boundary using linear regression from the end of the break-up distance to 30 mm further downstream.*

The break-up length can be evaluated from liquid boundary measurements or from spray tip penetration data where $S \propto t^{0.5}$.

Measuring the lift-off length

The lift-off length is defined as the distance from the injector to the location where the flame stabilizes. This quantity can only be measured using an imaging technique. Various portions of the natural light emission from the flame can be used as identifiers for the lift-off length. Higgins and Siebers [99] imaged the flame emission at 280, 310, 330, 340, 434, 532 and 695 nm, where the first 4 bands fall within the bands of OH^* chemiluminescence, the fifth within CH^* chemiluminescence band and the last two dominated by broad band soot luminosity. It was found that the 310 nm band was provided the best marker for the lift-off length. This band is dominated by OH^* chemiluminescence with minimal contamination from soot luminosity while still exhibiting good detectability. This is the band chosen to evaluate the lift-off length based on OH^* chemiluminescence. A high speed camera equipped with an intensifier is used to image the flame through a narrow 10 nm FWHM band pass filter centered on 309 nm. In extremely sooting regions, it is possible for the soot incandescence to be intense enough to bleed through resulting is some contamination of the pure OH^* signal. However, significant amounts of soot only form downstream of the lift-off location, thereby not affecting this metric.
The chemiluminescence snap shots are averaged over the quasi steady period of the injection. The average image displays two lobes of strong chemiluminescence close to where chemiluminescence initiates. The lift-off length is defined by the distance from the injector to the location where the chemiluminescence intensity is approximately 50% of the signal at the intense lobes as seen in Figure 89.

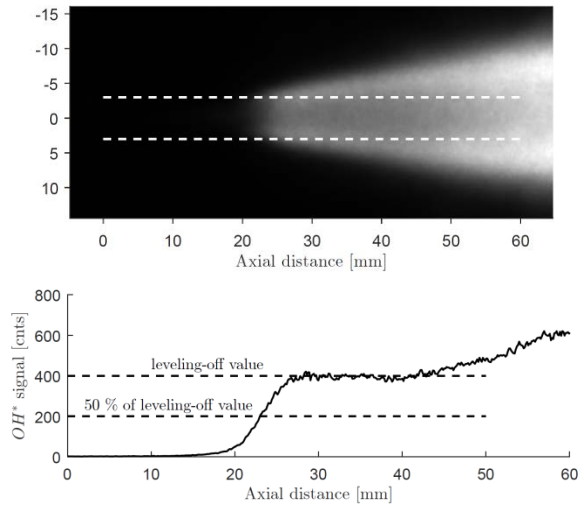

Figure 89: *Image representation of processing procedure for determining lift-off length from OH^* chemiluminescence imaging in fuel spray.*

Higgins and Siebers [99] found this definition to identify the mean location of the fluctuating instantaneous lift-off length.

Measuring the ignition delay

The ignition delay is determined as the time delay between the first indications of fuel emergence from the nozzle tip to the time of ignition. This definition is employed instead of the trigger to the injector as different nozzles have different hydraulic delays resulting from variations in needle lift and influences from the internal geometry etc. The hydraulic delays of Spray C and D have been determined from the DBI measurements of the liquid phase using the time from the trigger to the time of the frame just prior to any indication of liquid (Figure 90). The average hydraulic delay for Spray C and D were found to be 369 µs and 388 µs respectively.

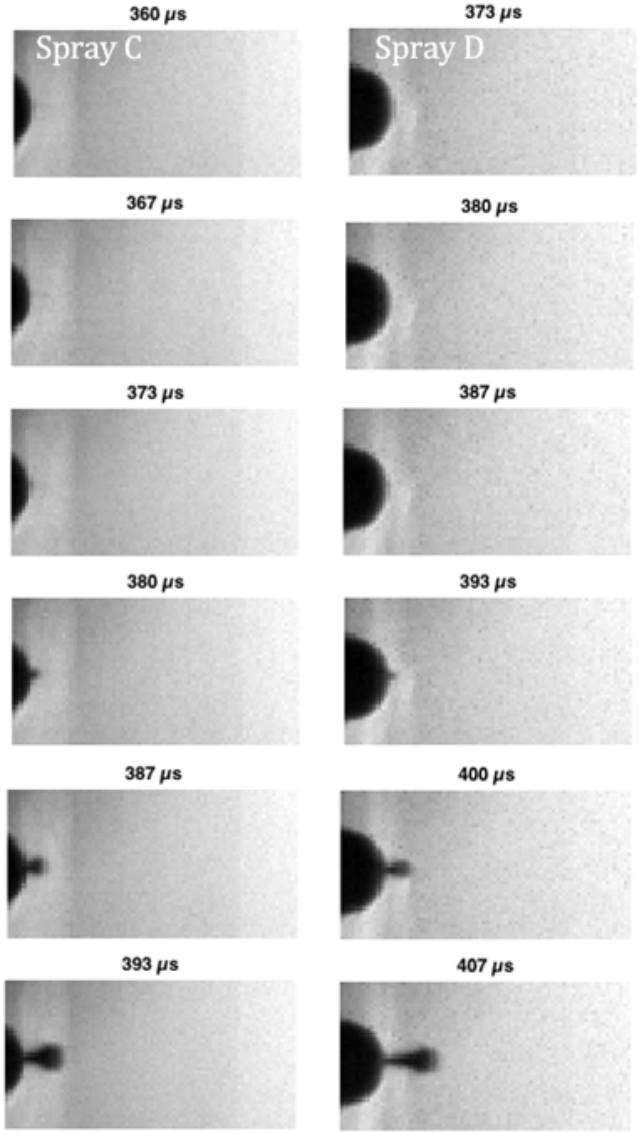

Figure 90: *Determination of hydraulic delay from raw liquid DBI measurements for Spray C and D. The hydraulic delay for these specific images is 373 μs and 387 μs for Spray C and D respectively.*

The ignition delay is found by imaging the natural luminosity from the flame. Ignition is said to occur when the absolute luminosity surpasses a user defined threshold found by identifying the signal strength of the strong chemiluminescence occurring prior to any soot formation [100]. An example of this can be seen in Figure 91 where the first three frames are low intensity luminosity from the cool flame.

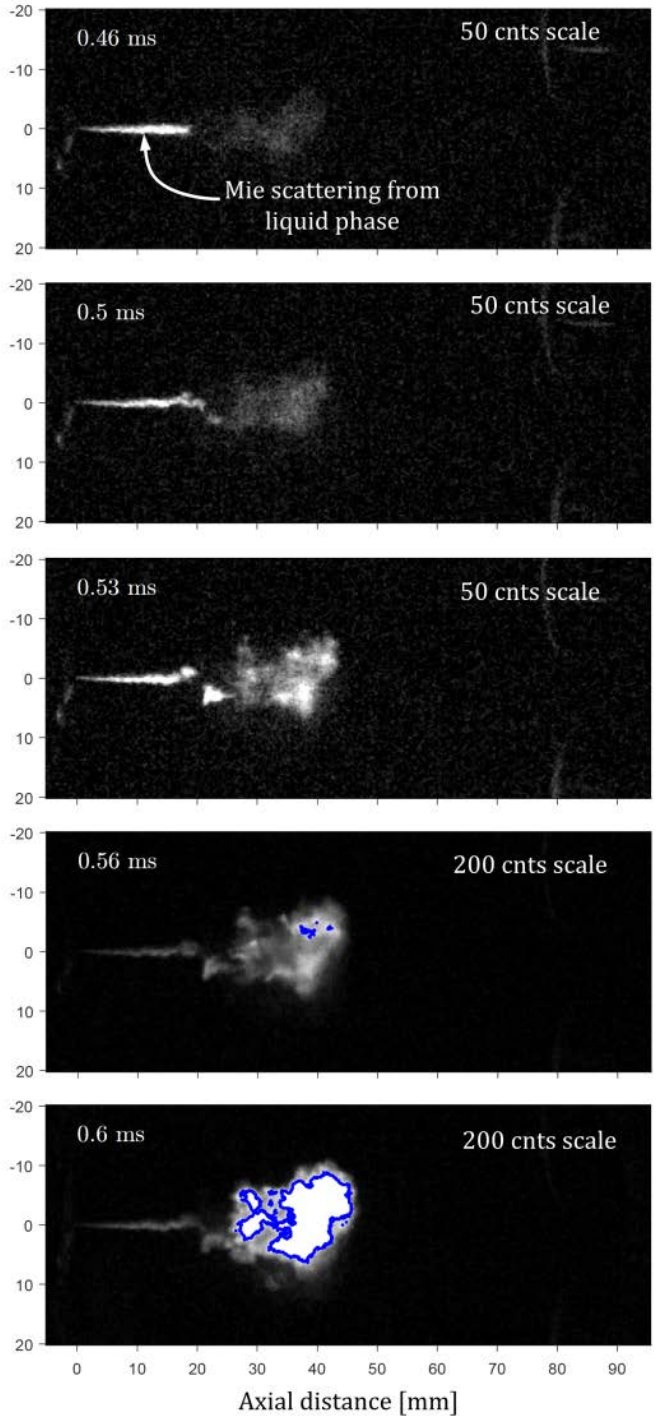

Figure 91: *Natural luminosity image sequence for a single injection event. The scaling is indicated in the top right corner of the respective images. The threshold of 200 cnts for the strong chemiluminescence is indicated by the blue boundary.*

In the last two frames strong chemiluminescence is indicated by the borders at a threshold of around 200 cnts. The interpreted ignition delay for the sequence in Figure 91 was 0.56ms.

Optical configuration for soot measurement

Soot extinction measurements were acquired with the DBI technique described in the earlier sections. An LED with emission centered on 630 nm 17 nm FWHM was the source of illumination. The back illumination was significantly brighter than the flame luminosity in the spectral band of the LED. The camera was equipped with a 628 nm 32 nm

FWHM band pass filter and a neutral density filter with an optical density of 2.5 ($\tau = 0.0037$) in order to reject the broad band flame luminosity. The camera used a 2.5 µs exposure and a framerate of 90000 fps, resulting in an effective resolution of 45 kHz for the extinction imaging measurements. The optical arrangement for imaging the light extinction by soot can be seen in Figure 92.

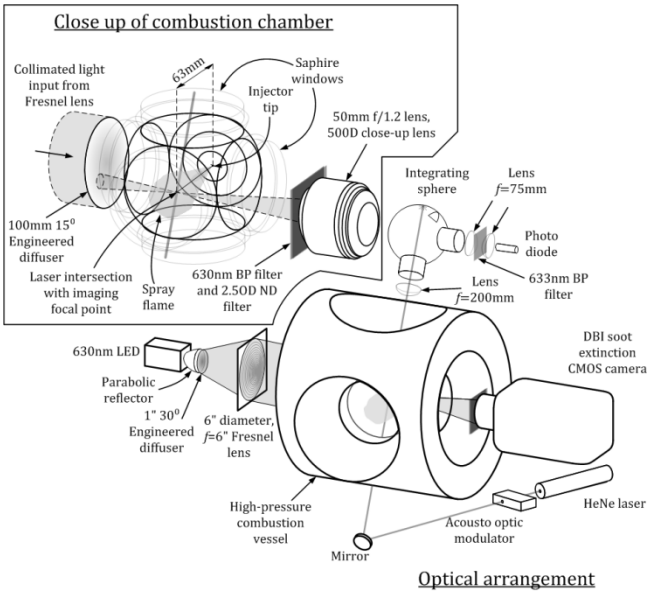

Figure 92: *Optical arrangements for extinction based measurements of soot.*

One-dimensional HeNe laser (632.8nm) extinction measurements were conducted simultaneously with the 2D resolved extinction imaging. The 10mW laser beam with a diameter of 1 mm passed through the flame at an axial distance of 63 mm from the injector tip (Figure 92). A collection lens increased the collection angle to a 100 mm integrating sphere (IS) in order to account for beam-steering effects. The signal from the IS was passed through a 1nm FWHM 633nm bandpass filter, to reject as much broad band flame luminosity as possible, before being focused to a photodiode. This collection system has previously been shown to be insensitive to beam-steering effects through the flame [41]. An acousto-optic modulator was used to generate rapid laser pulses at 104.17 kHz and the flame luminosity was collected in between the pulses at the same rate. More details on the HeNe laser extinction setup and processing can be found in [41,101]

The initial intention of these measurements was to perform multi-color extinction imaging at 400, 514 and 630 nm, thereby gaining quantitative soot volume fraction and information of the optical properties of the soot. However, attenuation by the bulk gas at the shorter wavelengths inhibited measurements at 400 nm and 514 nm. The attenuation is believed to arise from a contaminant as the severity could vary between injection events. It is believed that the attenuating agent was NO_2 as the attenuation was most severe at 400 nm, where NO_2 has its largest absorption cross-section. The contaminant could be an oil of some kind with a nitrogen component, releasing free radical nitrogen at significantly lower temperatures than that required for molecular nitrogen dissociation. For this reason only the measurements at 630 nm have been processed and analyzed for determining quantitative soot volume fraction.

Determining the optical thickness

When performing high speed soot extinction imaging of transient flames, some special considerations need to be taken into account. The optical thickness KL is calculated by Eq. (64).

$$\frac{I_{\mathrm{sf}}-I_{\mathrm{f}}}{I_{0\mathrm{s}}} = e^{-KL} = \tau \tag{64}$$

Where $I_{0\mathrm{s}}$, is a reference image of the illumination source (LED) through the combustion chamber ambient and optical access windows. I_{f} is the flame luminosity without back illumination and I_{sf} is the back illumination source together with flame luminosity. I_{f} and I_{sf} are collected alternately every other camera exposure. In present setup this is achieved with a LED pulsing at high speed as described in the experimental setup section. The flame luminosity image is subtracted from the I_{sf} image in order to measure the part of the back illumination that passes through the flame.

It is desirable that $I_{0\mathrm{s}}$ utilize as much of the dynamic range of the camera to maximize the signal to noise ratio of the transmitted signal between I_{sf} and I_{f}. As the transmitted signal is riding on the flame luminosity signal, the level of I_{f} should be reduced as much as possible using a combination of spectral and neutral density filters. One reason for this is that the signal to noise ratio of the transmitted signal decreases at higher levels of I_{f} due to the influence of shot noise (Figure 93).

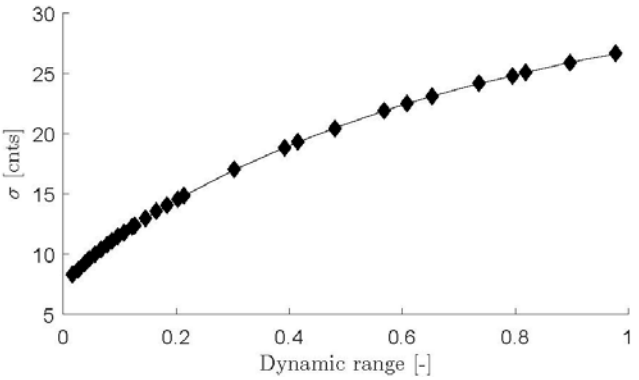

Figure 93: *Standard deviation of shot noise across the dynamic range of the camera.*

Another reason to minimize I_{f} is to reduce the errors introduced by the temporal separation between I_{fs} and I_{f} as they are measured alternately. This temporal separation depends of course on the frame rate of the camera and leads to local errors in the evaluation of the optical thickness. If $I_{\mathrm{f}} > I_{\mathrm{fs}}$, imaginary values of KL will occur which is a common artifact under optically thick conditions [15]. This can be reduced by performing the measurement at the highest temporal resolution possible and by suppressing the flame luminosity by means of filtering.

Motion estimation of flame luminosity

The Courant number (Eq. (65)) from numerical mathematics can be used as a dimensionless indicator for this source of error.

$$C = \frac{U\Delta t}{\Delta x} \quad (65)$$

Where U is the velocity of the spray, Δt is the temporal separation between the two images and Δx is the projected pixel size. A low Courant number in the measurements increases the chance that a soot cloud in a specific pixel during a I_{fs} measurement is still present in the same pixel during the following I_{f} measurement. Previous investigations applied median filtering to effectively degrade the spatial resolution, thereby decreasing the Courant number [91,15].

Averaging the flame luminosity images taken before and after the back illuminated image can also reduce the error. However, averaging images of a moving object is incorrect and differs from an interpolation method to estimate the intermediate position of the object. Rather, a temporal up conversion approach can be applied by using a motion analysis to estimate the position of flame luminosity between the two luminosity images before and after the illuminated frame. Some commonly used motion estimation algorithms are based on block-matching, phase correlation, pixel recursive or optical flow. Block matching and phase correlation work best at estimating relative translation between two similar images. They therefore work best with images of coherent structures. An example of a flame image, between two temporally shifted flame images, estimated by the block-matching algorithm can be seen in Figure 94.

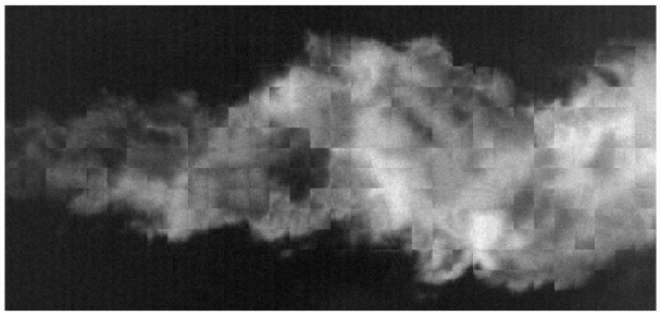

Figure 94: *Flame image predicted by block matching motion estimation algorithm.*

It can be seen that the motion estimation algorithms estimating translative offsets between images do not work well at estimating the flame movement as structures in the images may deform slightly from frame to frame. Methods of gradient based motion estimation like e. g. optical flow fit better to this specific application.

An example of the optical flow algorithm [102] applied to the prediction of a flame luminosity image from the images before, $I_{\mathrm{f},i-1}$, and after, $I_{\mathrm{f},i+1}$, the target image, $I_{\mathrm{f},i}$, can be seen in Figure 95. Also shown is the temporal average of the images $I_{\mathrm{f},i-1}$ and $I_{\mathrm{f},i+1}$ for comparison. Figure 95 shows that the prediction of the target image by means of simple averaging is blurred and that the residuals are larger and more local compared to the optical flow predicted image.

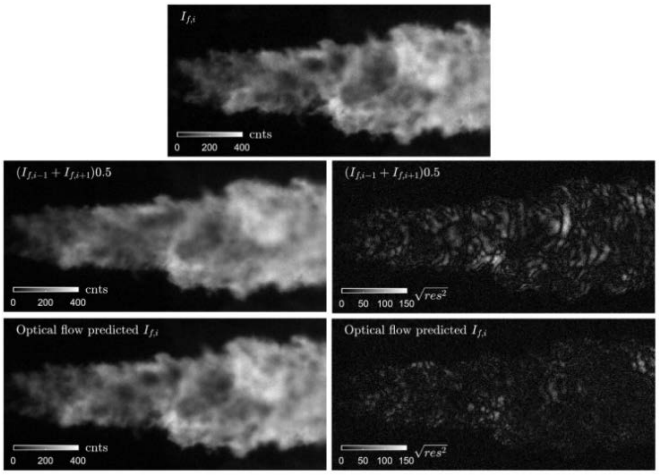

Figure 95: *Example of Optical flow motion estimation (below) used to predict $I_{\mathrm{f},i}$ (above) from $I_{\mathrm{f},i-1}$ and $I_{\mathrm{f},i+1}$. The result from averaging $I_{\mathrm{f},i-1}$ and $I_{\mathrm{f},i+1}$ is also shown (middle). The residuals are shown to the right of the respective images.*

Based on vapor penetration rate measurements of the current spray, U 60 mm downstream of the injector tip is around 65 ms^{-1}. This is used to estimate an effective Courant number

The example in Figure 96 shows the error that can occur in determining KL with degrading temporal resolution. The flame luminosity images before and after the illuminated frame are averaged. The base measurement has a temporal resolution of 90 kHz corresponding to a temporal delay of 22.2 µs between the flame luminosity images. The projected pixel size is 0.1068mm/pixel leading to a Courant number of $C = 6.79$ Also shown is the instantaneous KL map for the same measurement obtained with an optical flow estimated I_{f} image.

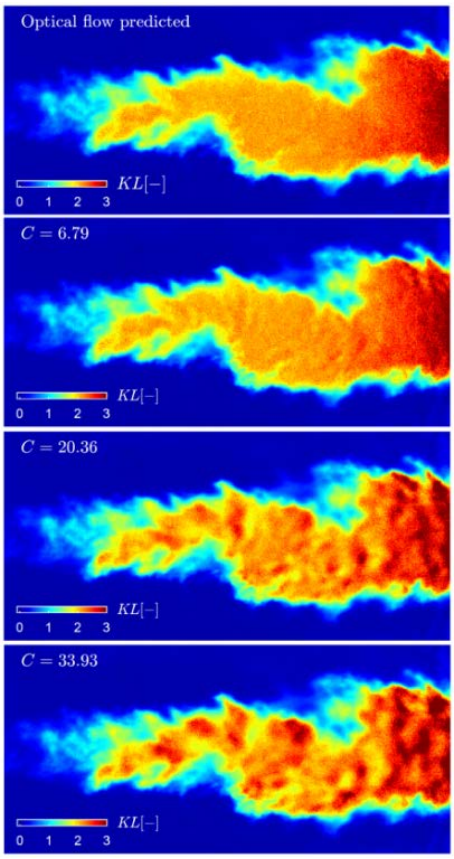

Figure 96: *Example of the error introduced in the instantaneous KL maps by the movement of the flame between images. The KL maps with increasing Courant number were obtained by*

averaging I_f images with increasing temporal separation ($C = 6.79$ being the Courant number at 90 kHz). The top image shows the KL map obtained with the optical flow estimated I_f.

The errors that occur are local and resemble ripples or wrinkles on the true KL map. This can even be seen in the 90 kHz measurement. As the optical flow predicted I_f displays lower residuals than that of temporal averaging (Figure 95), it can be assumed that the top image in Figure 96 is closest to determining the true local optical thickness. This image also displays least wrinkling, showing that using a motion estimation algorithm can reduce the error in determining the instantaneous *KL* map even at this high temporal resolution.
As seen in Figure 96, the significance of this error increases toward larger Courant number due to the larger movement of the flame luminosity between the images. Movement interpolation may also begin to fail at too large Courant number due to degradation of the pattern recognition. This highlights the importance of using the highest temporal resolution possible. Even though the optical flow algorithm [102] produces impressive results, testing of various algorithms is still a work in progress by the authors.
As mentioned this error is reduced by suppressing the flame luminosity. A consequence of this is that the transmission measurement consists of individual images from both the lower and upper end of the dynamic range of the camera. This makes the measurement sensitive to camera non-idealities.

Special camera considerations and corrections

As mentioned earlier, a typical camera response curve deviates from linearity as the pixel approaches saturation (Figure 24). In addition, there is "pixel response non-uniformity" (PRNU), which means that the sensitivity is pixel dependent. The pixel sensitivities are proportional and may be corrected with a gain factor specified for each individual pixel. However, as extinction imaging applies the ratio of images the gain factors of the individual pixels cancel out. Thus, it is sufficient to linearize the response curve of the individual pixels and leave the signal as an arbitrary count number. Maximum utilization of the cameras dynamic range increases the signal to noise ratio, thus influence of non-linear response should be expected and corrected.
The camera response curve should intercept zero. The zero is usually defined as the dark signal level (signal when sensor is un-illuminated). This signal reflects the random generation of electrons and holes as a consequence of the sensor temperature and the accumulated signal from all electrical components in the camera. It is dependent on the camera temperature and operating conditions.
However, it was found that the dark noise level was affected when the chip was exposed to alternating high and low levels of illumination. This is believed to be caused by an equilibrium offset of current leakage that pulls down the instantaneous dark noise level below the static reference level. Experiments made at 90,000 frames per second showed that several successive dark images were required to restore the dark level to the reference level. The difference between the instantaneous and static dark image was sensitive to the pixel specific charge distribution and exhibited a certain pattern which was found to be an effect of the chip architecture (Figure 97). The magnitude of this difference depended on the illumination brightness that the pixel was exposed to in the previous image.

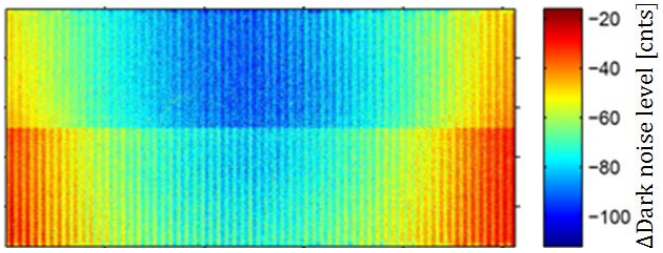

Figure 97: *Image of the altered dark signal level between the static level and the level immediately after an illuminated frame.*

Camera software usually offer an optional automatic correction for dark noise (termed e. g. shading correction or current session reference). This correction references the pixel specific readout range to the static dark noise level such that the dynamic range is extended. However, care must be taken when applying such a correction, as the dynamic level may be below the static one and consequently will be read out as zero. In this case information is lost.

Filtering considerations

As mentioned, spectral and neutral density filtering is a necessity in these kinds of measurements. Neutral density filters provide a constant spectral optical density, or transmission, across a wide range, usually across the visible range. Spectral filters transmit specified spectral range. Band pass filters transmit a narrow spectral band while short or long pass filters transmit a broad spectral range above or below a cut-off wavelength. Spectral curves of the optical density for various types of filters can be seen in Figure 98

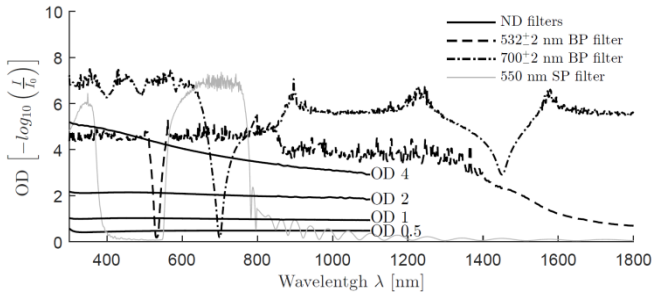

Figure 98: *Spectrally resolved optical density, $OD = -log_{10}\left(I/I_0\right)$, curves for various types of filters typically applied in extinction measurements.*

It can be seen that the specifications for the filters are only valid across the visible spectral range as these filters are intended for cameras with a response in the visible. The sensors in these cameras are usually non-responsive, or have poor quantum efficiency, in the wavelength range where the filters transmit outside their specified range. It is however vital that the filter's specs are valid in the range where the quantum efficiency of the camera is >0, as misinterpretation of measurements may occur otherwise.
The combination of a narrow band pass filter and neutral density filters with high optical density (<0.1 % transmission) effectively transmit a very small portion of the illumination and broad band flame luminosity. These filters can either be absorptive or reflective and are placed in a holder directly in front of the camera lens. Care should

be taken when using reflective filters, as the combination of the large amount of rejected radiation and the reflective surfaces may cause unintended reflections that can significantly affect the measurement. Examples of this can be seen in the DBI based extinction measurements of soot in Figure 99. The images were acquired with the optical arrangement in Figure 92. The camera was equipped with a combination of reflective ND filters, accumulating to an optical depth of 2.5 (Figure 99 above) and 2.8 (Figure 99 below), and a 628 FWHM 32 nm BP filter.

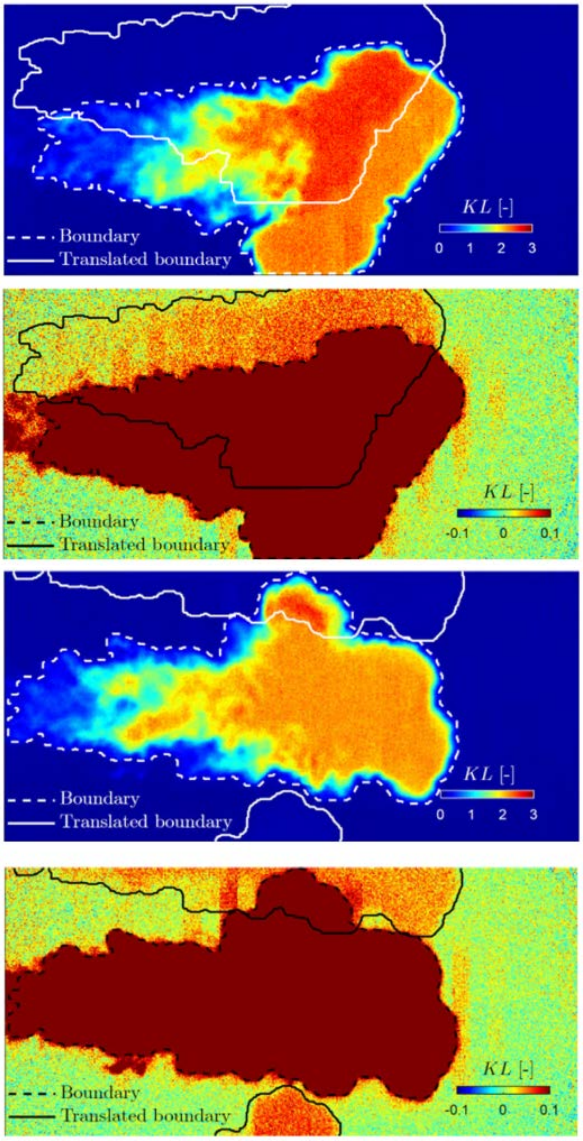

Figure 99: *Scaled KL images showing a translated image of the soot cloud as a consequence of light contributions from reflections. The two above and below images show the reflections for two slightly different orientations and combinations of the ND and BP filters.*

The above images in Figure 99 indicate that reflected rays form multiple translated images of the source and flame. This is believed to be a consequence of the combination of filters acting as a kind of "cavity". This means that light contributions not passing through the flame, I_R, are present in the true extinction image of the flame. Formulating this mathematically, we arrive to the following equation, Eq. (66), for the optical thickness KL.

$$KL = -\ln\left(\frac{(I_{fs}-I_f)-I_R}{I_0-I_R}\right) \tag{66}$$

The error in the interpreted optical thickness is not constant as it depends on the true optical thickness of the probed media. This can be seen in Figure 100, where the interpreted optical thickness is plotted as a function of the true optical thickness for different magnitudes of I_R.

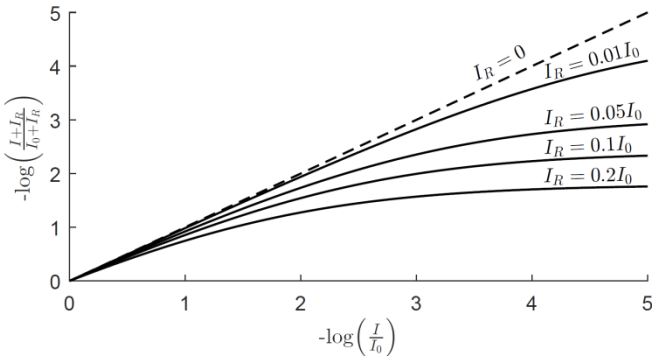

Figure 100: *Error introduced by contributions from reflected light, I_R, on the interpreted optical thickness of the soot cloud.*

Impressions of extinction measurements of soot

The spray C and D injectors are wide bore nozzles with orifice diameters of around 0.2 mm. Siebers and Pickett [52] found that sooting tendencies increase drastically with increasing orifice diameter. Albeit a more sooting fuel was used in those studies, the sooting tendencies observed from Spray C and D were extremely high.

The soot formed from these injectors is so optically thick, it is practically opaque. This is demonstrated in the high temperature DBI soot extinction measurements (cf. Figure 101), where the optical thickness reaches a plateau not far downstream of the injector, indicating saturation behavior.

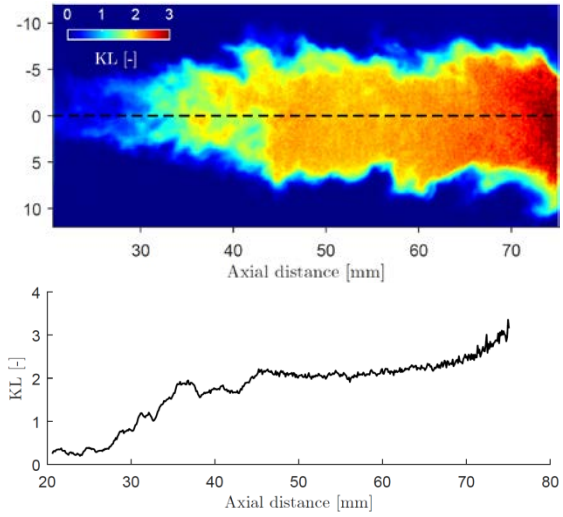

Figure 101: *Snapshot of optical thickness during the quasi-steady period of injection event JELDC (above). Centerline profile of optical thickness along spray axis (below).*

This phenomenon is also evident in the laser extinction measurements where the temporally resolved optical thickness at the point 63 mm downstream on the central axis of the injector reaches a maximum level at higher temperatures. This can be seen in Figure 102. The

measurements at higher temperature are very noisy as the signal, if any, to noise ratio is so poor that only noise is measured.

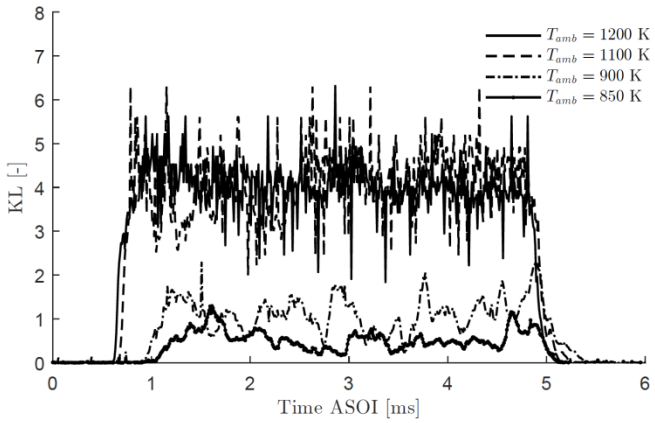

Figure 102: *Laser extinction measurements at a point 63 mm downstream of the injector tip for Spray C at various ambient temperatures.*

Back to the extinction images, the low optical thickness, ~2, in the apparently opaque region of the flame (where KL should approach infinity) is a consequence of reflected light, I_R, not passing through the flame reaching the detector. I_R can be thought of contribution of reflected light from filters and internally in the camera objective. The measured optical thickness will be affected in the manner seen in Figure 100. The reflected light forming multiple images of the source, and consequently flame attenuation, is caused by the filter pack acting as a sort of reflecting cavity. We denote this contribution $I_{R,f}$. The statistical occurrence of internal reflectance in the camera objective drastically increases when the light source is diffused and extended, which is yet another contribution which we will call $I_{R,c}$. $I_{R,c}$ is likely much smaller than that of $I_{R,f}$. These contributions are illustrated in Figure 103 along with the main contribution I_{fs} which is the quantity we want to measure.

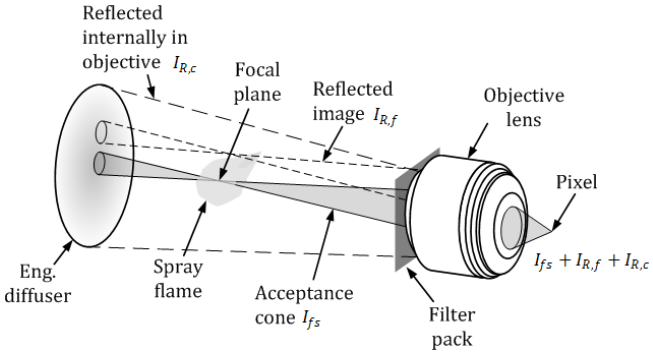

Figure 103: *Illustration of all possible light contributions to one single pixel.*

If we entertain the idea that the flame is in fact opaque, one can obtain information of the spatial distribution and magnitude of the reflected light, I_R, as this must be the only contribution to light in the opaque region of the flame.

As the opaque region of the flame sweeps across the field of view during the injection event, more and more of I_R becomes exposed. This is utilized in order to attain as much spatial information of I_R as possible as seen in Figure 104, where the image of I_R is based on 3 JELDC injection events.

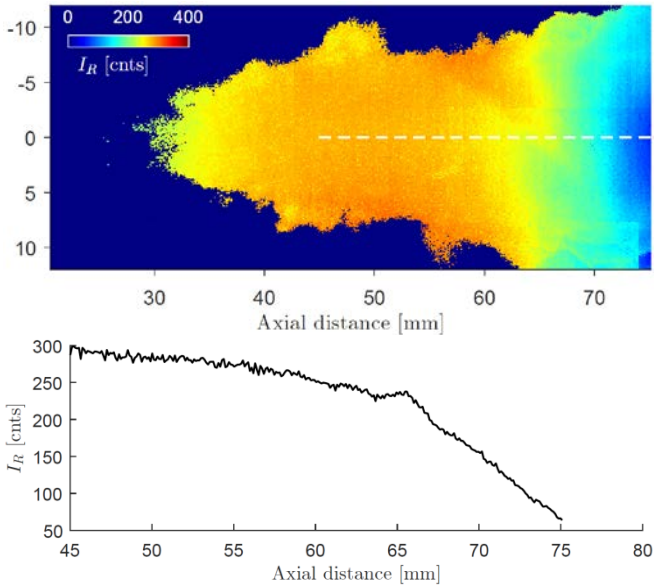

Figure 104: *Spatial information of I_R obtained via averaging $I_{sf} - I_f$ in the opaque regions of the flame for three injection events in JELDC condition (above). The axial profile of I_R as indicated by the dashed line in the image of I_R (below).*

The rest of I_R is taken to be rotationally symmetric using the profile in Figure 104 (below). It is impossible to separate the reflection contributions and only the combined contribution, I_R, can be determined.

As the flame attenuates I_R in the regions shown in Figure 99, light in these regions must be compensated for before subtracting I_R in Eq. (66). This is done by adding translated images of $\left(1 - \frac{I_{sf} - I_f}{I_0}\right) C I_0$ to I_{sf}, where the scaling constant C is estimated qualitatively based on the removal of the reflections outside the flame as seen in Figure 105.

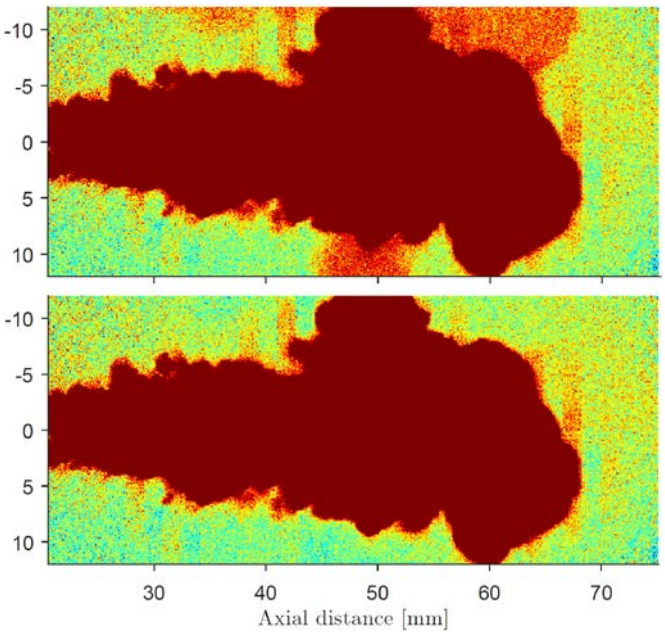

Figure 105: *Scaled images of the flame optical thickness showing the correction compensating for attenuation of I_R. (Above) before correction and (below) after correction.*

This procedure re-establishes the contribution from I_R in these regions such that the total contribution from I_R can be subsequently subtracted as in Eq. (66). The total equation can then be written up as Eq (67).

$$\tau = \frac{(I_{\mathrm{fs}} - I_{\mathrm{f}}) + \left((1-\tau)CI_0\right)_{\mathrm{trans}} - I_R}{I_0 - I_{\mathrm{R}}} \tag{67}$$

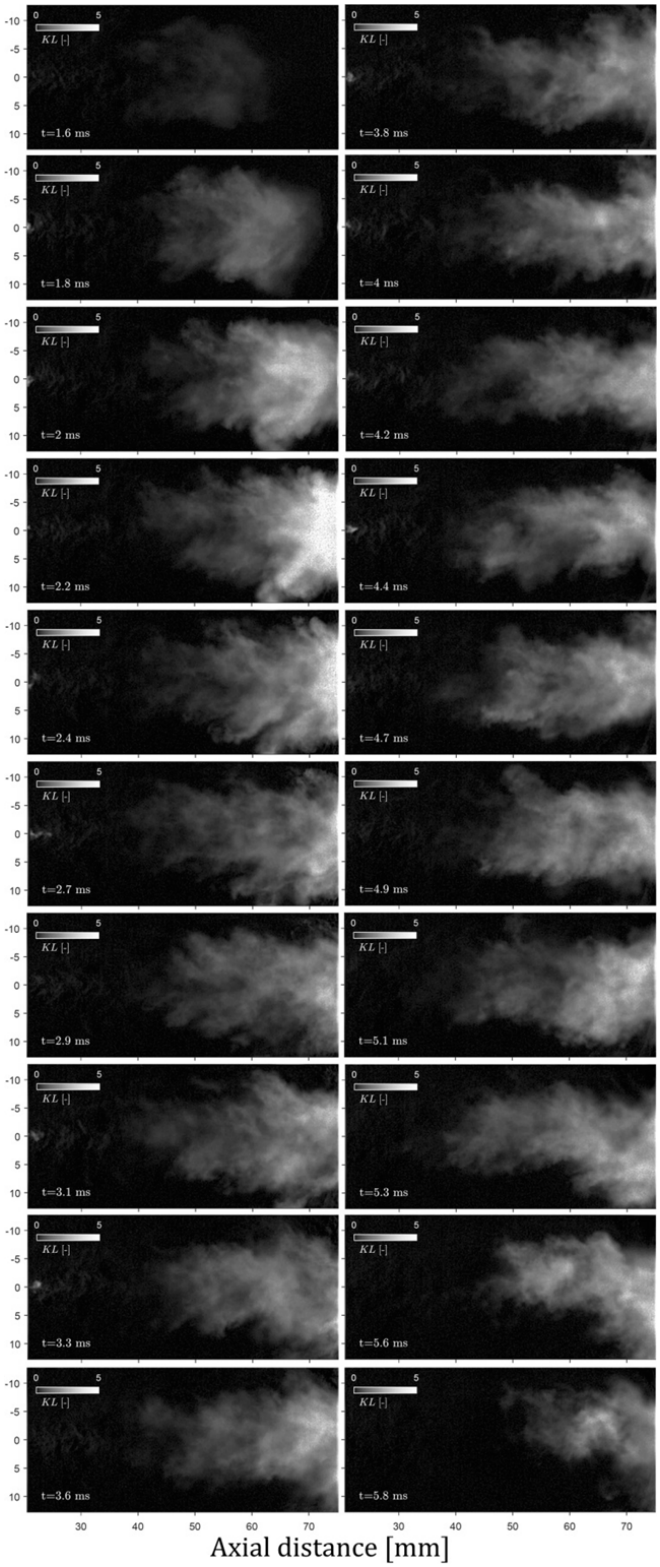

Figure 106: *Optical thickness image sequence of a JKLDC injection event with time ASOI indicated. The gray scale goes from 0 to 5 optical thickness.*

The argument that the flame is opaque is likely as the difference between $I_{\mathrm{fs}} - I_{\mathrm{f}}$ images from separate measurements display only noise in the regions where the flame is opaque. This also indicates that the contribution I_{R} is constant and reproduced in separate measurements (as long as the filter orientation is not changed). Furthermore, the KL maps generated with optical flow predicted flame luminosity indicates that the true KL map is indeed completely flat and featureless (Figure 96).

Reflections should ideally not be present emphasizing the importance of proper filtering. Extinction imaging under these conditions is still a new area of research and the findings of this work have significantly aided in improving the technique and identifying sources of error. However, with the assumptions made, a correction for I_{R} has been obtained. Thus, the optical thickness where the flame is not opaque can be determined. An image sequence of the optical thickness from a JKLDC injection event can be seen in Figure 106.

The images have been corrected in the manner described and illustrate the amount of detail captured in the snapshots. The sequence also indicates the quasi-steady period of the injection event, starting from when the spray head has passed the field of view, approximately 2.9 ms ASOI, until the injection stops, approximately 5.1 ms ASOI. Unfortunately the flame is highly asymmetric in the snapshots such that a tomographic reconstruction assuming rotational symmetry would yield inaccurate slice profiles of the soot volume fraction. However, averaging the images over the quasi-steady period of the injection event will average over the turbulence, revealing an image of the stable flame which is relatively symmetric. Furthermore, as the boundary conditions in the vessel are highly reproducible ensemble averaging is also possible. This enables tomographic reconstruction assuming rotational symmetry.

The soot from spray combustion under similar conditions to those here have been TEM sampled [89] from which the parameters in Table 8 have been determined [91]. The dimensionless extinction coefficient at 630 nm has been determined from these parameters using the Rayleigh-Debye Gans approximation assuming a refractive index of $\widetilde{m} = 1.75 + 1.03i$.

Table 8: *Parameters determined from TEM soot sampling of fuel sprays* **[89,91]**.

Parameters	Value
Fractal prefactor, k_{f}	8.36
Fractal dimension, D_{f}	1.79
Number of primary particles, N	150
Primary particle diameter, d_{p} [nm]	16
Radius of gyration, R_{g} [nm] (Eq. (26))	40
Wavelength, λ [nm]	630
Refractive index, $\widetilde{m}$	$1.75 + 1.03i$
Scattering to absorption, $\alpha_{\mathrm{sa}} = \sigma_{\mathrm{sca}}^{\mathrm{agg}} / \sigma_{\mathrm{abs}}^{\mathrm{agg}}$	0.059
Dimensionless extinction coefficient, k_{e}	7.45

Experimental results

A qualitative view of the spray/jet emanating from the spray C and D injectors can be seen in image sequences in Figure 107, where simultaneous images of the liquid and vapor phase of the sprays have been superimposed in false color. The images provide an excellent demonstration of what can be made visible with the two different back-illumination techniques.

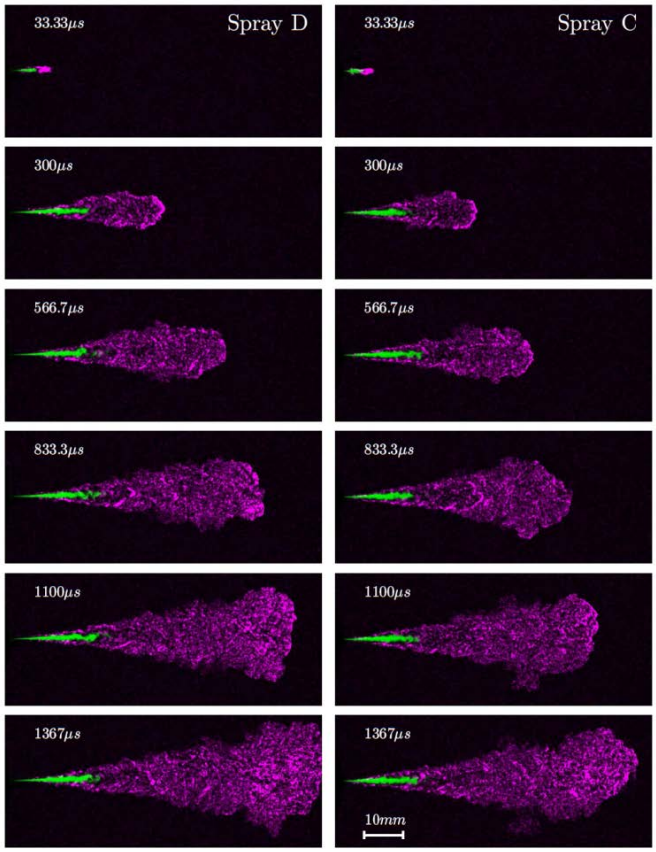

Figure 107: *Image sequence of superimposed liquid (green) and vapor (magenta) phase of single injection event from nozzle D (left) and C (right). The images consist of DBI liquid penetration and schlieren vapor penetration measurements under standard non-reacting conditions. Spatial resolution of the vapor measurements have been scaled according to the liquid measurements in order to superimpose in false color. The time stamps indicate time after start of injection* [57].

Lliquid phase

The time resolved ensemble averaged liquid penetration length as measured with DBI and Mie scattering can be seen in Figure 108.

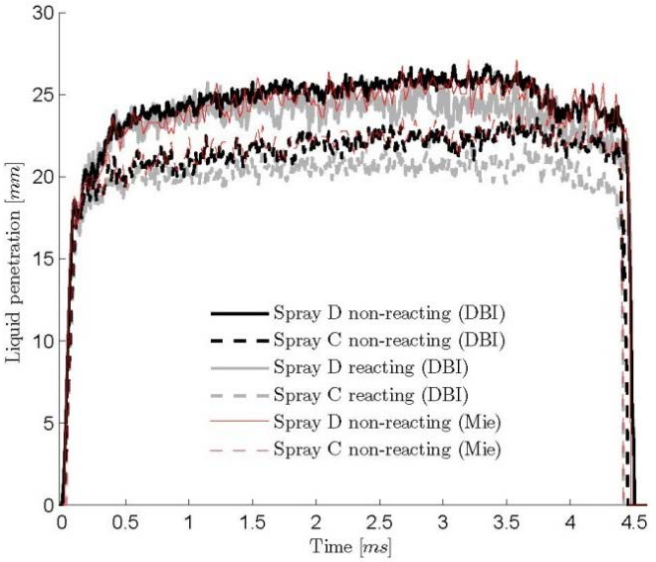

Figure 108: *Time resolved ensemble averaged extinction-based (DBI) and scattering-based (Mie) liquid penetration measurements of Spray D and C injectors under standard non-reacting conditions and standard reacting conditions ($x_{O_2} = 0$, $T_{amb} = 900$ K, $p_{inj} = 1500$ bar, and $\rho_{amb} = 22.8\ kg \cdot m^{-3}$) with DBI only* [57].

It can be seen in Figure 108 that, in contrast to previous studies [93,92], there is excellent agreement between the scattering and extinction based measurements of the liquid penetration length. The difference in liquid penetration length between Spray C and D cannot be explained by the difference in spray momentum and nozzle coefficients (cf. Table 7) alone according to the spray/jet model by Musculus and Kattke [73]. The differences must then be a consequence of cavitation induced flow disturbances within the nozzle. Studying the liquid phase boundary in more detail reveals that the differences are confined immediately outside the nozzle exit. In this region Spray C is wider and has a larger angle compared to Spray D as can be seen in the superimposed snapshots of the liquid phase from Spray C and D in Figure 109. This indicates differences in the spray break-up.

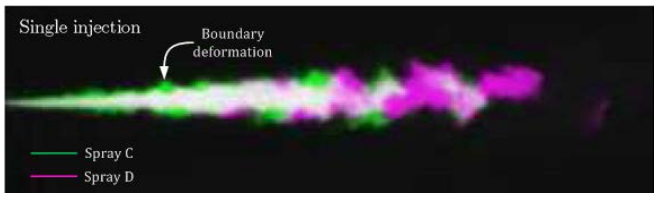

Figure 109: *Superimposed snapshots of the liquid phase from Spray C and Spray D showing that Spray C is wider in the near nozzle region with larger boundary deformation. The white region shows where the sprays overlap* **[57]**.

On average the radial profiles exhibit resemblance beyond a point downstream of the injector. For future reference the point from which the sprays exhibit similar behavior has been termed the "similarity onset" or SO which is located closer to the injector for Spray C. The averaged radial boundaries with their respective SO indicated are plotted in Figure 110 a). It can be seen that the profiles collapse downstream of SO when referenced to their respective SO.

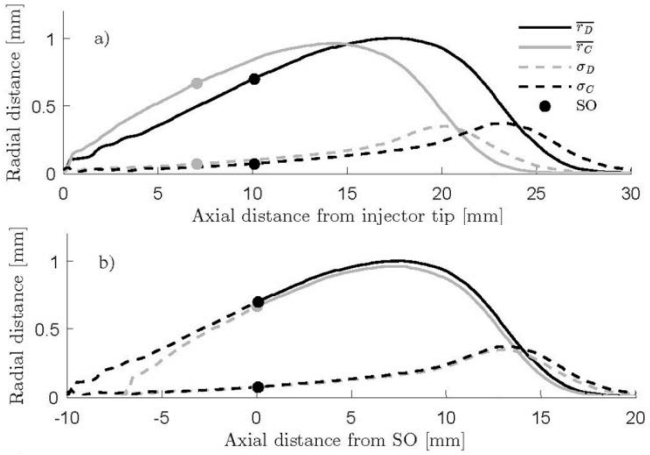

Figure 110: *Quasi-steady and ensemble averaged radial boundaries of the liquid phase and the standard, **σ**, of the boundary deformation for injection conditions BKLD a) referenced to the injector tip and b) referenced to SO* **[57]**.

Vapor phase

The measured spray tip penetration from spray C and D can be seen in Figure 111. It can be seen that Spray D penetrates slightly faster than Spray C most likely due to the slightly higher spray momentum.

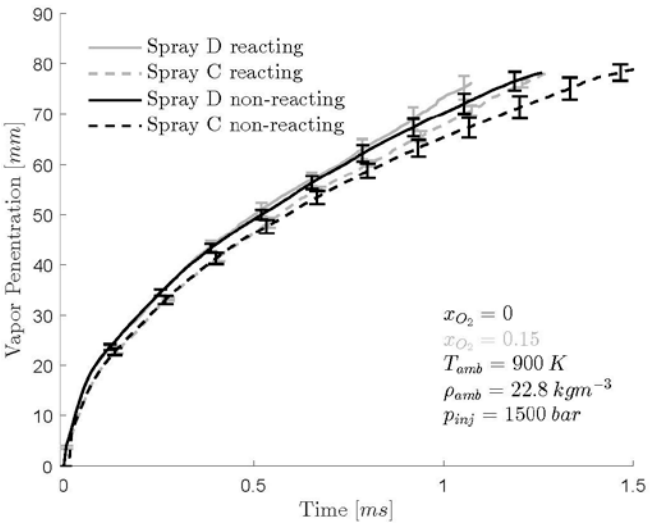

Figure 111: *Measured spray tip penetration measurements from spray C and D under inert (BKLD) and reacting (JKLD) conditions* **[57]**.

However, when plotting the dimensionless penetration distance vs. the dimensionless penetration time for the two nozzles on a logarithmic scale [74], an interesting observation can be made. It can be seen that for Spray D, $\tilde{S} \propto \tilde{t}$ in the short time limit due to spray break-up, while for Spray C, $\tilde{S} \propto \sqrt{\tilde{t}}$ from the start of the injection. Slight misinterpretation of the start of injection may greatly influence the result seen in Figure 112. Nevertheless, it was found that $\tilde{S}$ never became proportional to $\tilde{t}$ when adjusting the start of injection for Spray C.

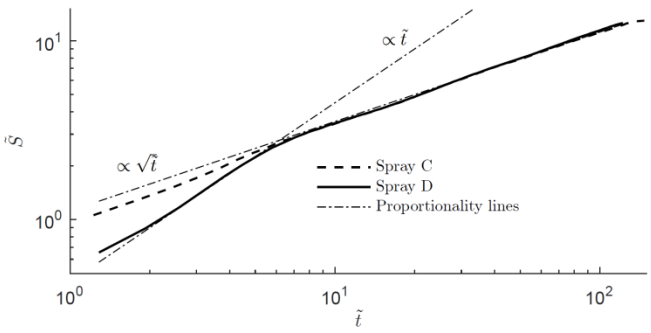

Figure 112: *Dimensionless spray tip penetration distance, $\tilde{S}$, as function of dimensionless penetration time, $\tilde{t}$, for Spray C and D. x^+ and t^+ were evaluated from nozzle coefficients stated in Table 7.*

This indicates vastly different break-up processes occurring from the two injectors as can be expected from influences of cavitation. The difference in the dispersion of the spray immediately at the nozzle exit, causing $\tilde{S} \propto \tilde{t}$ for Spray D and $\tilde{S} \propto \sqrt{\tilde{t}}$ for Spray C, may then also contribute to the difference in vapor penetration.

The dispersion angles, θ, deducted from the vapor boundaries using the definition from Naber and Siebers [74] revealed difference of over 2 degrees between Spray C and D, with Spray C being $20.8° \pm 0.1°$ and D being $18.7° \pm 0.2°$. These results are similar to that of [103] who deducted θ from similar nozzles with the same definition illustrated in Figure 61 a). However, when using the definition illustrated in Figure 61 b), assuming an unspecified virtual origin of the self-similar jet, the interpreted dispersion angles were $20° \pm 0.4°$ and $19.8° \pm 0.2°$ for Spray C and D respectively, basically showing that the dispersion angles are the same. The differences are then confined to the break-up zone, where the enhanced break-up from cavitation induced flow disturbances increases the dispersion angle immediately outside the nozzle. This shortens the break-up length, forcing the transition to self-similar scaling flow closer to the nozzle.

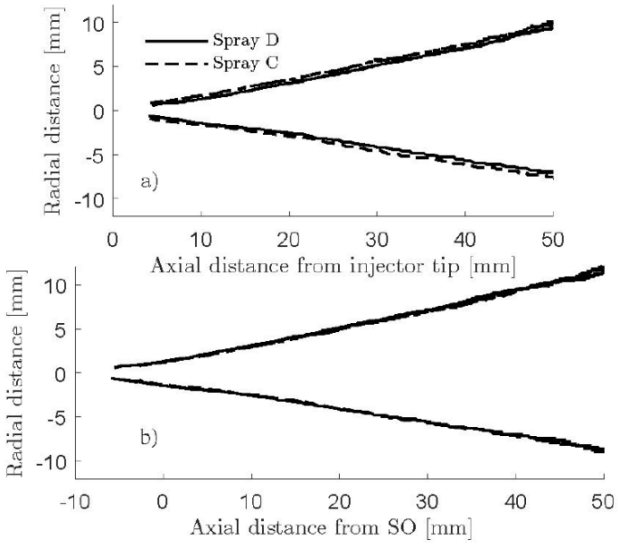

Figure 113: *Average vapor boundaries of Spray C and D interpreted from schlieren imaging a) referenced to the injector tip and b) referenced to SO* **[57]**.

The definition of a virtual origin is a more accurate interpretation of θ as the vapor boundaries from Spray C and D collapse when referenced to SO as seen in Figure 113. It can also be seen that θ remains fairly constant downstream of SO for both sprays, indicating that the dispersion angles in the self-similar part of the jets are in fact very similar.

Lift-off length

Ensemble and quasi-steady averaged images of OH* chemiluminescence from Spray C and D across the temperature range 800-1200 K can be seen in Figure 114.

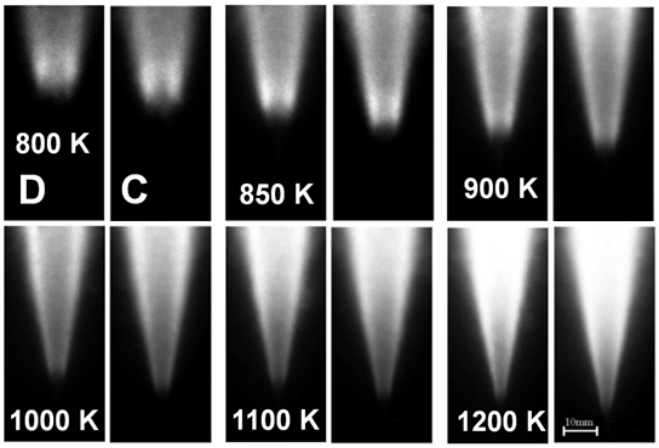

Figure 114: *Ensemble and quasi-steady averaged images of OH* chemiluminescence from Spray C and D.*

It can immediately be seen that the flame stabilizes closer to the injector for Spray C compared with Spray D across the entire temperature range. The signal saturates at higher temperatures due to the intense soot luminosity leaking through the narrow band pass filter at 309 nm. Scatter plots of the interpreted lift-off length across a range of operating conditions can be seen in Figure 115.

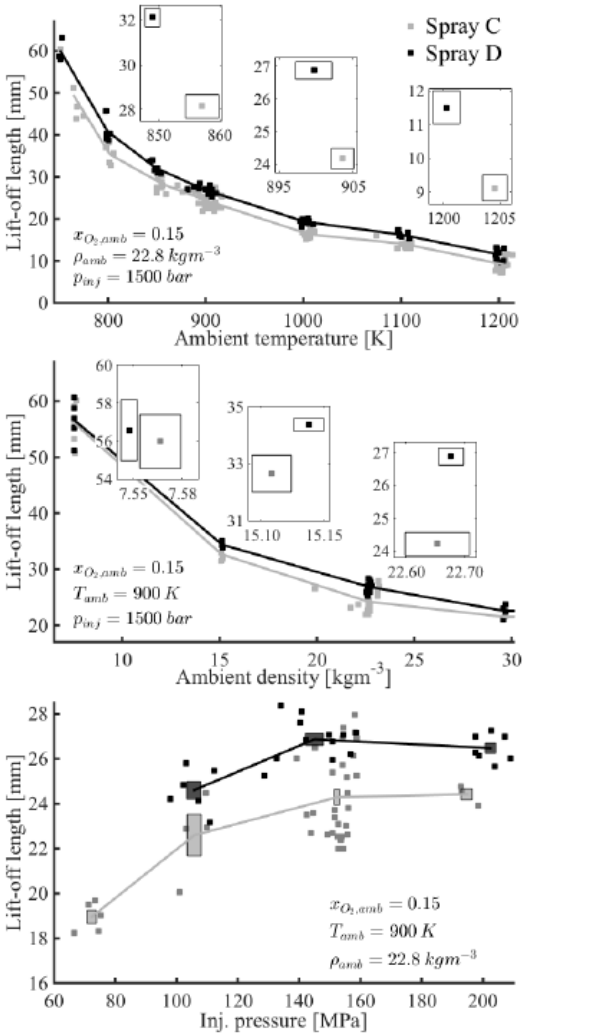

Figure 115: *Scatter plots of the quasi-steady lift-off length as a function of ambient temperature (top), ambient density (middle), and fuel injection pressure (bottom). Because the standard error cannot be resolved in the full axis, inset axes are provided in the top and middle panels with the mean values and the standard error for select cases* **[57]**.

The difference in lift-off length seems to be consistently 3-4 mm across the broad range of conditions. This value is consistent with the difference in SO observed in the liquid phase.

Remarkably, comparison of many distinguishing features of the two sprays shows consistency when referenced to SO. Liquid length, lift-off length, and the jet outer boundary collapse when this similarity offset is taken into account. Even for reacting data obtained over a wide range of operating conditions, the dispersion angle discernable in OH* chemiluminescence images also appear similar. The differences in the spray break-up region apparently create an important offset between a cavitating Spray C and non-cavitating Spray D that affect many of the spray and combustion metrics to a similar degree.

Ignition delay

The ignition delay times deducted from luminosity imaging are identical for the two nozzles as seen in Figure 116.

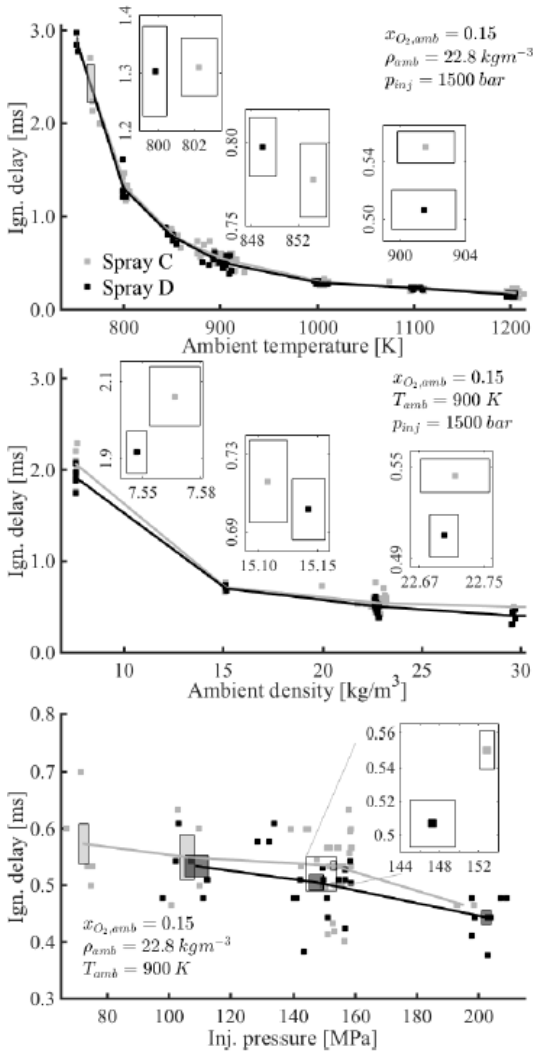

Figure 116: *Scatter plots of light-based ignition delay measurements as a function of ambient temperature (top), ambient density (middle), and fuel injection pressure (bottom). Inset plots are provided for select cases showing the mean and standard error of the mean for both the x- and y-variables* **[57]**.

The ignition location is slightly further downstream for Spray D as can intuitively be deducted when comparing the spray tip penetration and the ignition delay measurements.

Soot volume fraction

Ensemble (over minimum 3 injections) and quasi-steady averaged maps of the optical thickness of the soot clouds from spray C and D have been used to reconstruct the soot volume fraction maps across an ambient temperature sweep from 850-1200 K. The results can be seen in Figure 117. Artifacts along the central axis are a consequence of the tomographic reconstruction. As discussed above there is no information available in the regions where the flame appears opaque. Upstream from the dashed lines the flame is not opaque, meaning that the measured f_v can be trusted in this region. Downstream from the dashed line the opaque region is indicated by a region of zeros. A pixel was considered opaque when the optical thickness was greater than 4 during more than 50% of the quasi-steady period.

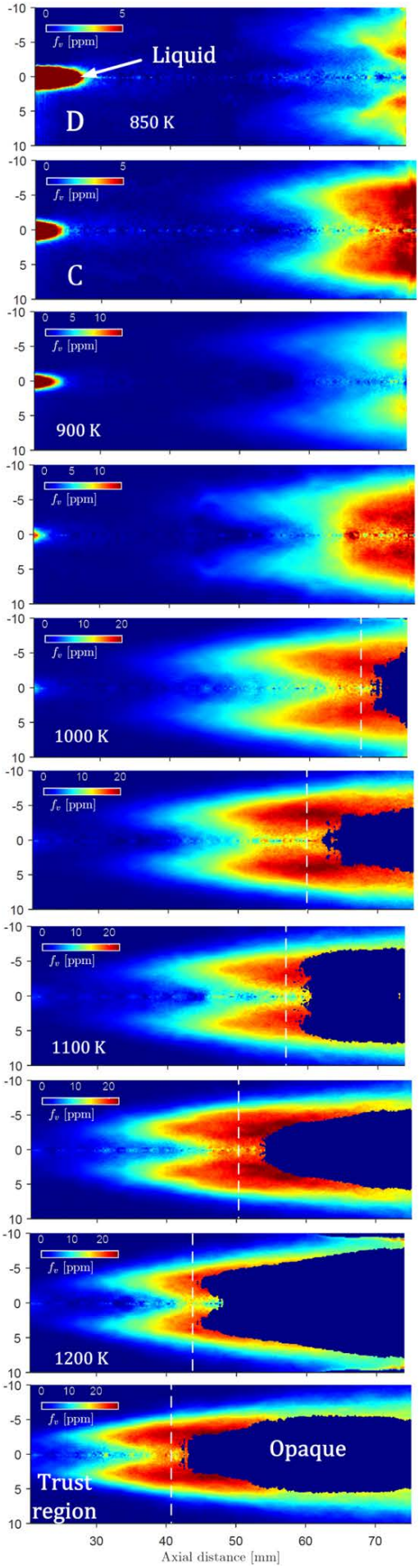

Figure 117: *Maps of the soot volume fraction from Spray D (left) and Spray C (right) with the trust region and opaque region indicated.*

The soot inception starts at the sides of the central axis, forming soot wings. The wings are formed due to the air entrainment rate in these large orifice diameter injectors. Higher entrainment rates lessen the tendency for the soot to form wings in the spray periphery [81]. Further downstream these wings merge and form a large soot cloud with a high soot concentration. This leads to an extremely optically thick flame (mostly due to the long optical path length). The bell shape where the wings merge is a consequence of the radial velocity and mixture distribution in the jet.

At higher temperatures the soot inception zone moves upstream, where the spray is narrower with higher axial velocities and richer mixtures. This occurs as the reaction rate drastically increases with temperature. Soot oxidizes faster at higher temperatures as well, causing the soot cloud to be thinner with sharper gradients in the soot concentration.

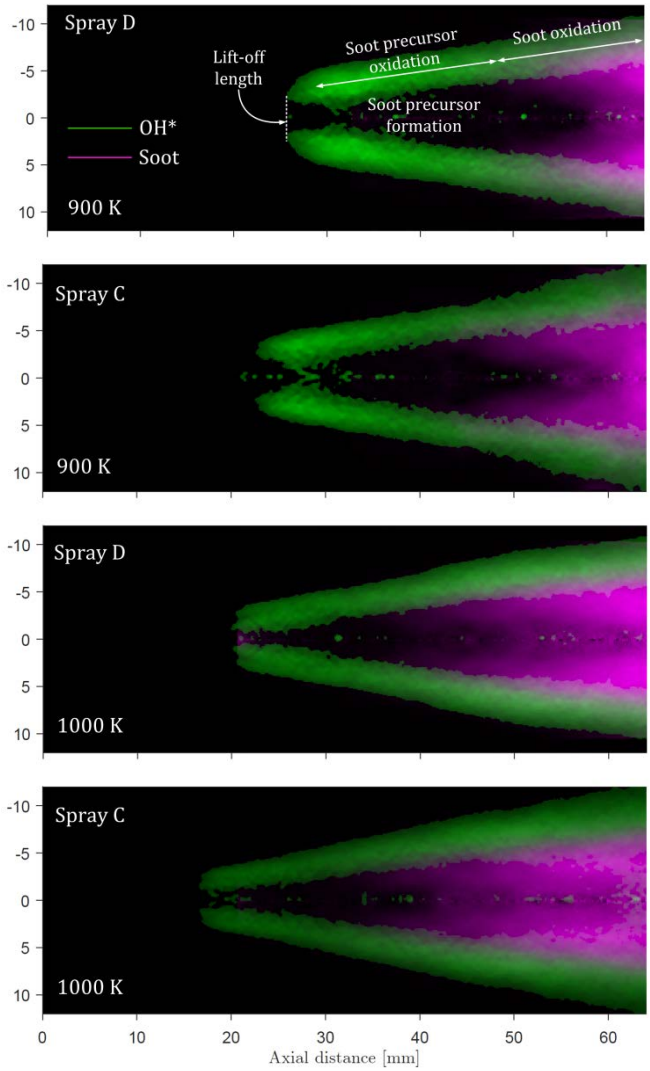

Figure 118: *Spatial distribution of OH^* and soot generated from super positioning of composite images of the reconstructed soot field and OH^* distribution.*

In Figure 118 the spatial distribution of OH^* chemiluminescence has been reconstructed via tomography and super imposed onto the map of the soot field showing qualitatively the flame structure. It can clearly be seen that the soot and OH^* are separated, where the OH^* is located outside the soot zone where the soot is oxidized in a diffusion flame. The flame structure agrees well with Pickett and Siebers's [81] adaptation of the conceptual model of Flynn et. al. [79].

It should be noted that there are experimental uncertainties involved in the OH^* measurements. The tomographic reconstruction does not take into account the absorption of the signal through the line of sight. In addition, soot luminosity may contaminate the signal in the soot oxidation zone, leading to an incorrect representation after tomographic reconstruction. This artifact can be seen in the lower image of Spray C at 1000 K, where OH^* chemiluminescence is evident in regions with high soot concentration. Despite these uncertainties it is believed that a fairly accurate representation of the flame structure can be deducted and that the majority of the signal in the soot oxidation zone stems from OH^* as the signal is highest where the soot concentration diminishes. The fact that the OH^* signal prior to nucleation of soot precursors is not contaminated by soot luminosity and that the continuation of the diffusion flame from the precursor oxidation zone to the soot oxidation zone further suggests that the majority of the signal is in fact OH^* chemiluminescence.

To further analyze the flame structure, the steady spray model of Musculus and Kattke [73], enabling user defined spray/jet boundaries, has been applied in order to deduct information of the mixture field. This model assumes the velocity distribution issuing from the nozzle to be uniform transitioning to fully developed flow at the end of the potential core. The velocity profiles are of the form described by Abramovich [104] in Eq. (68).

$$\frac{U}{U_c} = (1 - \zeta^{\alpha})^2 \tag{68}$$

Where ζ is the dimensionless radius (r/R), U/U_c is the velocity profile normalized by the center axial velocity. The exponent α describes the shape of the velocity profile throughout the potential core and is constant in the self-similar part of the jet. For the uniform profile issuing from the nozzle, α is ∞. Beyond the potential core, in the self-similar part of the jet, α is 1.5.

The spatially resolved averaged liquid and vapor boundaries deducted from DBI and schlieren measurements for the reacting as well as non-reacting case were used as inputs to the model. The liquid boundary was determined using the mixing limited vaporization assumption of Siebers [66] (Eqs. (46) and (49)). The NIST standard reference database [105] was used to look up the thermodynamic properties of fuel and ambient in the iterative procedure. A fuel temperature of $T_f = 363$ K and the ambient gas composition for 15 and 0 % O_2 stated in Table 3 was used in the calculations. The results from the calculations have been superimposed together with the OH^* and soot measurements for Spray D and C at 900 K ambient temperature and 22.8 kg/m^3 ambient density in Figure 119.

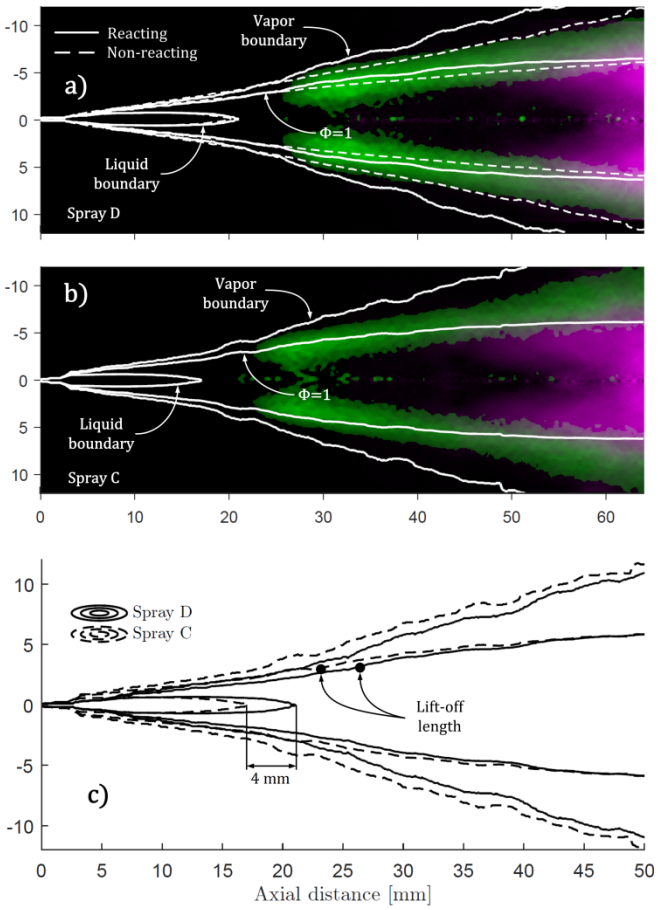

Figure 119: *Mixing contours superimposed onto the image of the flame structure from a) Spray D and b) Spray C. c) shows the difference in the mixture field caused by the geometrical difference between the Spray D and C injectors.*

Firstly, the exponent α, depicting the onset of self-similar flow, reaches a constant value of 1.5 at an axial distance of around 6 mm for Spray C and 10 mm for Spray D. This agrees very well with the SO determined from comparing the liquid radial profiles in Figure 110. Figure 119 a) includes the non-reacting spray/jet boundaries in order to illustrate the effect of thermal dilation of the jet from the heat released by the combustion reactions. The boundaries leading up to the lift-off length are identical before the reacting jet expands. It can be seen in both Figure 119 a) and b) that the stoichiometric mixture contours coincide well with the "lobes" of intense OH^* chemiluminescence where the most exothermic combustion reactions are taking place. However, the mixture field downstream of the lobes with intense chemiluminescence, in the precursor and soot oxidation zone, does not follow the diffusion flame. The reason being that beyond the fuel rich premixed flame, the mixture contours are misrepresentative as the model assumes a non-reactive jet. The fuel is decomposed through partial oxidation in the rich premixed flame at the lift-off length, consuming the oxygen and thereby dilating the location of the diffusion flame wrt to the non-reacting mixture field. The liquid penetration lengths evaluated based on mixing limited vaporization accurately predicts the difference of 4 mm in liquid penetration between Spray C and D. The absolute penetration distance is however slightly under predicted by around 3 mm compared to the measured liquid penetration lengths. However, using a constant dispersion angle, depicted by the jet in the self-similar region, as input to the model and omitting the Siebers's correction factor of $a = 0.66$ [66], leads to an under prediction of the liquid penetration length by over 10 mm and a difference between Spray C and D of less than 1mm. This shows that the effect of cavitation on the break-up of the spray is captured by the simple steady model as they are inherent in the measured spray/jet boundary. The reason for the slight under prediction of the absolute penetration distance may be due to the finite resolution of the measured spray/jet boundary or uncertainties about the initial temperature of the fuel. It may then be assumed that the mixture field generated by the model is also representative. It can be seen in Figure 119 c) that the stoichiometric mixture contour from Spray C occurs at a wider radial location wrt Spray D and that the radial position of the at the lift-off length is almost identical. It seems again that the cavitation induced wider dispersion angle in the break-up region causes a shift in the combustion metrics downstream.

The flame structure seems to be fairly well maintained, with Spray C shifted closer to the injector. The differences in the soot inception distance between the two nozzles also reflect this, with Spray C being shifted upstream by around 4 mm. However, when looking at the absolute measurements of the soot volume fraction, the growth rate appears faster for Spray C as is apparent from the axial increase in soot concertation in the soot wings. In fact the soot distribution from Spray D resembles more that from Spray C at 100 K lower ambient temperature. It is speculated that the differences in the soot formation is caused by slightly higher fluctuations in the velocity field for Spray C. This would in turn affect the average self-similar velocity profile, causing a slightly lower centerline velocity and higher velocities in the periphery. The effect would decrease the available oxygen to the interior of the mixing controlled flame beyond the lift-off location. Slight decrease in the oxygen availability could explain the more rapid growth in soot concentration for Spray C compared to D.

Comparison with CFD modelling

The purpose of the measurements is to validate CFD modelling of the complex flow, chemistry, soot formation and radiation in these types of flames. These elements are all dependent on each other. In this section RANS CFD simulations of Spray D under reacting and non-reacting conditions have been initiated by K. M. Pang and compared to the measurements here to demonstrate the use of experimental data in model validation.

The model used a Lagrangian framework to model the two phase portion of the jet, unsteady Reynolds-averaged Navier Stokes $k-\varepsilon$ method to model the turbulent flow and a skeletal n-dodecane surrogate model for the combustion and soot modelling [106,107,108]. The modelling of soot is fairly new and is empirically based for the most part. Recently Skeen et. al. [109] summarized the progress of soot modeling and experimental soot measurements made by the ECN and the agreement between modeling and experiments thus far.

The vapor and liquid boundaries and penetration measurements have been used to validate the flow field. The lift-off length and ignition delay measurements have been used to validate the combustion model and the soot volume fraction measurements used to validate the soot model both quantitatively and qualitatively.

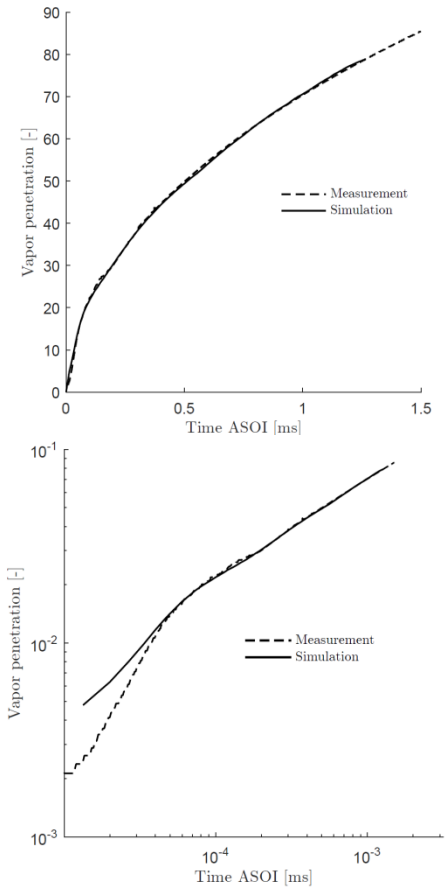

Figure 120: *(Above) Simulated and measured vapor penetration for Spray D under non-reacting conditions with* $T_{\mathrm{amb}} = 900\ K$, $\rho_{\mathrm{amb}} = 22.8\ \mathrm{kg \cdot m^{-3}}$ *and* $p_{\mathrm{inj}} = 1500$ bar. *(Below) The same curves on a logarithmic scale in order to enhance the break-up time.*

The vapor penetration predicted by the model agrees well with the measured penetration as seen in Figure 120 (above). It can also be seen that the break-up model predicts a similar break-up time as the measurements though with a slightly steeper gradient. The short time limit penetration is very demanding to model and the agreement with measurements is therefore quite impressive.

This indicates that the two phase portion and turbulent part of the jet is fairly well predicted by the model.

The mixture field predicted by the CFD model can be seen in Figure 121 along with the mixture field predicted by the steady jet model of Musculus and Kattke [73] using measured vapor the boundary. It can be seen that the fuel air ratio corresponding to roughly the same angle as the measured vapor penetration seems to be shifted downstream, posing the question if the entire mixture field may be shifted due to inconsistencies in the modelling of the complex spray break-up near the nozzle. However, the outer vapor boundary is measured with the schlieren technique which in turn is based on the gradient in density. For this reason a more logical method of comparing the outer most vapor boundary is comparing the gradient of the simulated mixture field with the measured one.

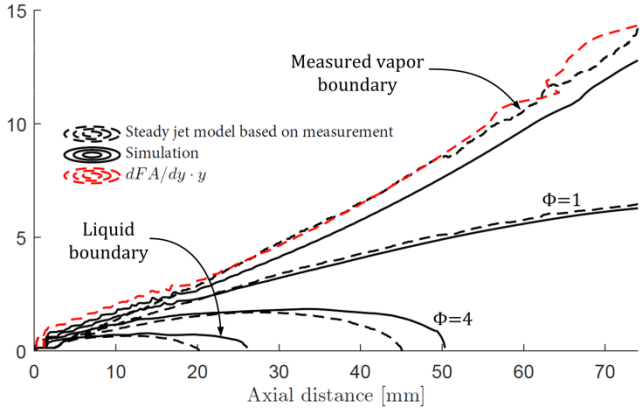

Figure 121: *Mixture field of Spray D under non-reacting conditions with* $T_{\mathrm{amb}} = 900\ K$, $\rho_{\mathrm{amb}} = 22.8\ \mathrm{kg \cdot m^{-3}}$ *and* $p_{\mathrm{inj}} = 1500$ bar *predicted by the CFD model compared to that predicted by the steady jet model based on measured vapor boundary.*

With this method of comparison the result is an outer boundary matching the angle and position of the measured vapor boundary as indicated by the red dashed line in Figure 121. It can also be seen that the CFD model predicts a liquid penetration length closer to the measurements and that the $\Phi = 4$ contour extends further downstream. The difference in the velocity distribution from the CFD model to the constant distribution of the steady jet model causes this difference. All in all, the CFD model appears to predict the spray/jet well.

The measured and predicted lift-off length and ignition delay times can be seen in Figure 122. Very good agreement can be seen in the prediction of lift-off length. However, the ignition delay times are under predicted compared to the measurements. This is most likely due to the different thresholding methods for model compared to

measurements. Where the model is based on the pressure rise and the measurements based on chemiluminescence from ignition reactions using an absolute camera count threshold. The ignition delay time and lift-off length are however coupled. This supports that the mismatch in ignition delay stem from different thresholding methods based on the well matched lift-off length.

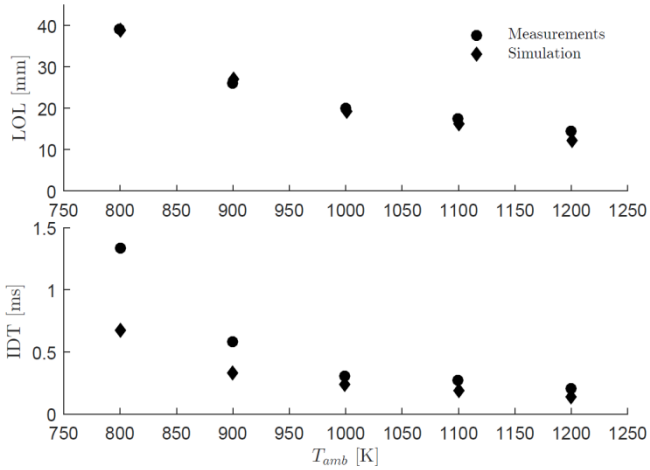

Figure 122: *Measured and modeled lift-off length and ignition delay times for Spray D with* $x_{O_2} = 0.15$, $T_{amb} = 900 \rightarrow 1200\ K$, $\rho_{amb} = 22.8\ kg \cdot m^{-3}$ *and* $p_{inj} = 1500\ bar$.

The soot volume fractions from the simulations have been translated into optical thickness in order to achieve a more direct comparison with measurements. The reason why this method of comparing may be useful is that the measured optical thickness is not strictly rotationally symmetric and therefore the tomographic reconstruction may introduce artifacts. The soot field from RANS simulations is axisymmetric and therefore rotationally symmetric i. e. translating the simulations into optical thickness rather than translating the measured optical thickness into soot volume fraction introduces fewer artifacts.

The baseline soot model under predicted the soot volume fraction by a factor of around 2. However, this model was initially based on a skeletal n-heptane model, while n-dodecane has a slightly higher soot propensity. A tuning parameter directly connected to the soot propensity is the surface growth submodel constant, C_g [107] which has been doubled from the base model. As seen in Figure 123, the optical thickness predicted by the simulation generally increases more rapidly with axial distance than the measurements. This indicates that soot formation or oxidation rates may be over or under predicted.

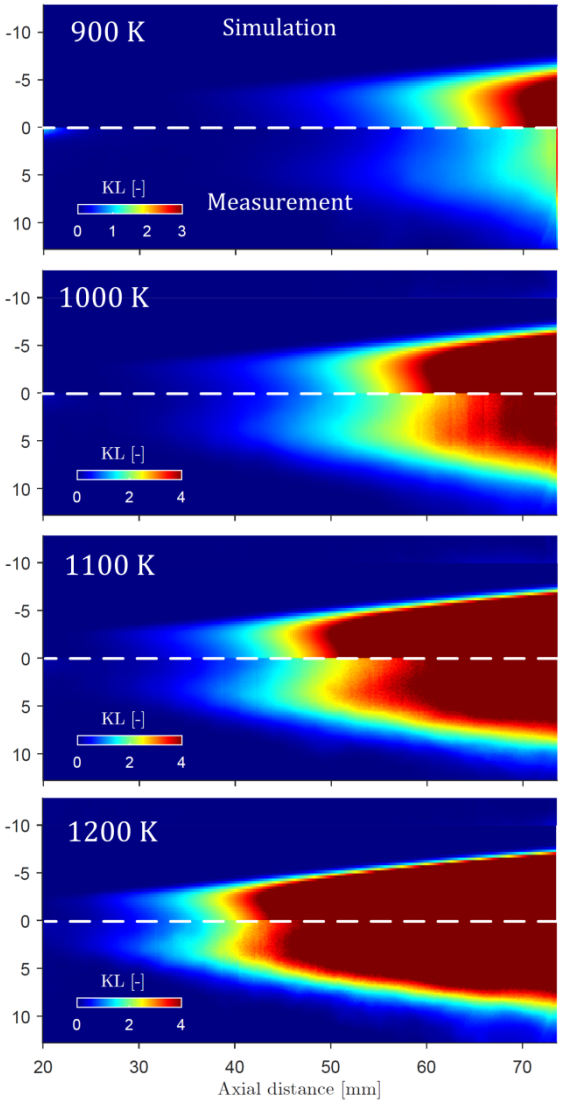

Figure 123: *Optical thickness at 635 nm of soot cloud from Spray D with* $x_{O_2} = 0.15$, $T_{\mathrm{amb}} = 900 \rightarrow 1200\ \mathrm{K}$, $\rho_{\mathrm{amb}} = 22.8\ \mathrm{kg \cdot m^{-3}}$ *and* $p_{\mathrm{inj}} = 1500\ \mathrm{bar}$ *predicted by the baseline CFD model with* $2 \cdot C_{\mathrm{g}}$ *compared to measurements.*

The oxidation rate of soot by O_2 was tuned to investigate this influence. Doubling the oxidation rate, k_{O_2}, gave results more consistent with the measurements wrt the optical thickness as seen in Figure 124. It can be seen that the model still increases slightly more rapidly with axial distance. However, the difference is very slight considering the complex physics that are being modelled.

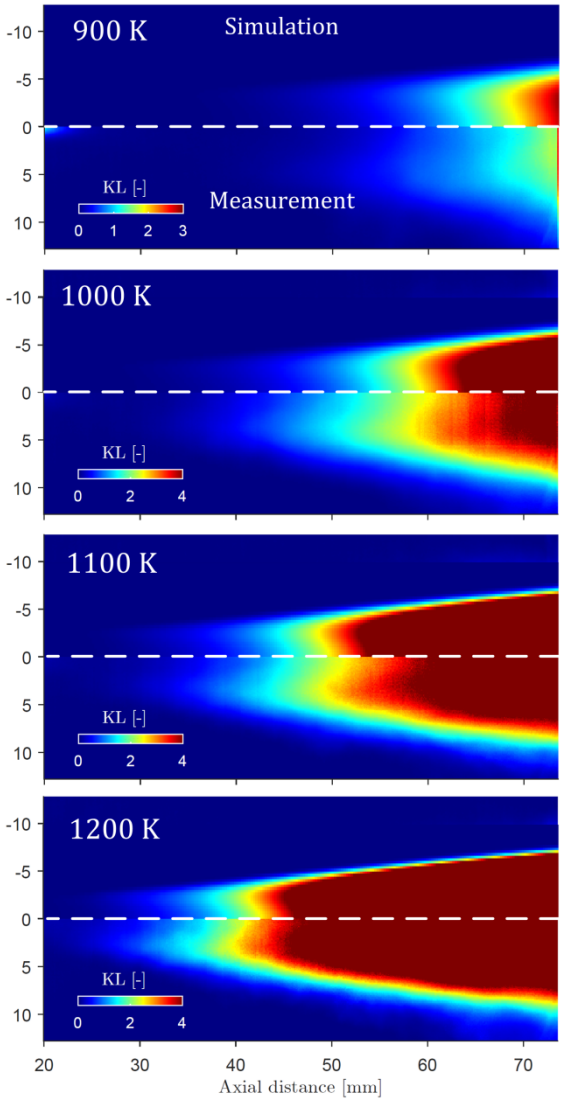

Figure 124: *Optical thickness at 635 nm of soot cloud from Spray D under reacting conditions with* $T_{\mathrm{amb}} = 900 \rightarrow 1200$ K, $\rho_{\mathrm{amb}} = 22.8\ \mathrm{kg \cdot m^{-3}}$ *and* $p_{\mathrm{inj}} = 1500$ bar *predicted by the CFD model with* $2 \cdot C_{\mathrm{g}}$, *and* $2 \cdot k_{\mathrm{O_2}}$ *compared to measurements.*

Further, the simulated soot volume fraction is compared with the measured soot volume fraction in Figure 125. Fairly good agreement is observed both in absolute concentration and spatial distribution. The measurements appear more "smeared" due to the transient movement of the flame during the averaging interval. The temperature field predicted by the CFD model is superimposed on the measured soot field. The contour of 1400 K is significant as past observations have shown that soot does not form under temperatures lower than this [81].It can be seen that the merging of the soot wings formed in the jet periphery is well predicted at lower ambient temperatures as also seen in the temperature contours. At ambient temperatures above 1000 K however, the merging occurs well within the 1400 K contour. This may be caused by the model not predicting the sooting tendency with ambient temperature perfectly, or by the predicted velocity field being slightly too higher in the central portion of the jet than causing a difference in the temperature field. On the other hand, it may also be artifacts in the measurements brought on by the tomographic reconstruction. Nevertheless, the simulations display satisfactory consistency with the measurements.

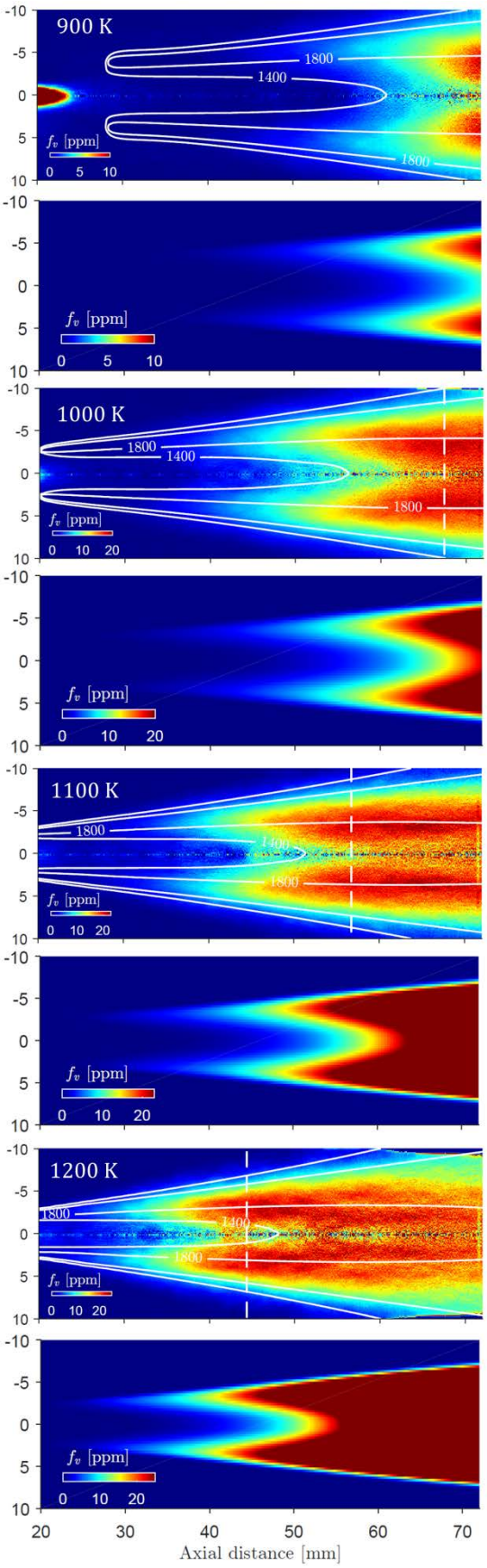

Figure 125: *Soot volume fraction from Spray D under reacting conditions with* $T_{\mathrm{amb}} = 900 \rightarrow 1200$ K, $\rho_{\mathrm{amb}} = 22.8\ \mathrm{kg \cdot m^{-3}}$ *and* $p_{\mathrm{inj}} = 1500$ bar *predicted by the CFD model compared to measurements. Temperature contours from the CFD model have been superimposed on the measured soot and the dashed lines*

indicate the axial location where the flame appears opaque in the measurements.

With the good agreement between measured and modelled soot volume fraction we can use the model results to get an idea of what the optical thickness may potentially be in the regions where the flame appears opaque in the measurements. The apparent optical thickness of the soot cloud at 1000-1200 K predicted by the CFD model can be seen in Figure 126.

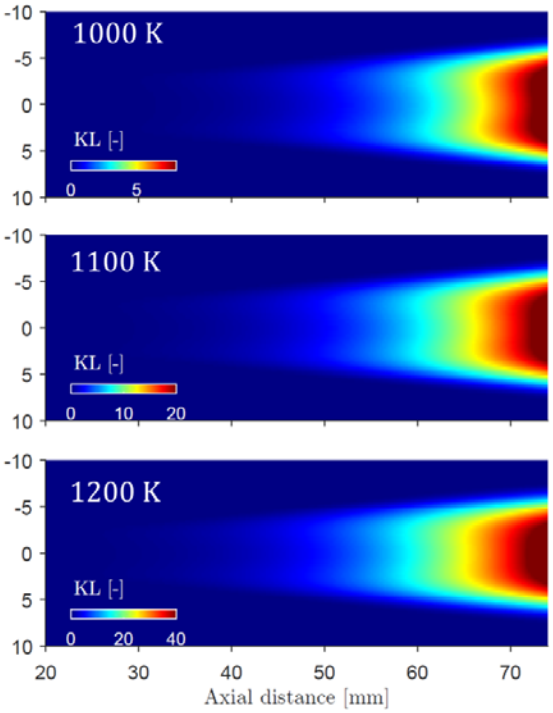

Figure 126: *Potential optical thickness at 635 nm of soot cloud from Spray D under reacting conditions with* $T_{\mathrm{amb}} = 1000 \rightarrow 1200$ K, $\rho_{\mathrm{amb}} = 22.8\ \mathrm{kg \cdot m^{-3}}$ *and* $p_{\mathrm{inj}} = 1500$ bar *based on CFD modeling of soot volume fraction.*

It can be seen that the optical thickness at 635 nm with 1200 K ambient temperature is potentially around 50 which is impossible to measure with current modern measurement devices. The only option is to go to longer wavelengths where the flame appears less optically thick.

Radiation model for spray flame

In this last section, all the aspects of spray combustion studied in this work is put together to provide a simple analysis of the radiative emission from these flames and its contribution to heat loss. Previous studies, and the experimental evidence presented in this work, suggest that the quasi-steady spray flame can be considered to behave with self-similar scaling [46,57,73]. The radiation observed through one line of sight in the spray flame can then be considered fairly similar throughout the spray. Upstream of the soot inception zone the flame emission is dominated by molecular emission from the hot gases. The length of this region depends on the ambient conditions. Higher ambient temperature and density will reduce this length [81]. The flame considered here ($T_{\mathrm{amb}} = 1000$ K and $\rho_{\mathrm{amb}} = 22.8\ \mathrm{kg/m^3}$) has a very short distance from the lift-off length to the soot inception zone so only the sooting region of the flame is considered here.

The concentration profiles of CO_2, H_2O and soot have been separated into a sequence of gas cells, indicated in Figure 127, in order to simplify the radiant transfer calculations for the gas phase. The hottest region of the flame is in the wings where the fuel/air mixture is close to stoichiometric and is consequently where the highest concentration of CO_2 and H_2O is located. The soot cloud is located closer to the center of the spray axis and is therefore at a lower temperature. It is assumed that the soot radiation is confined to the outer shell due as the cool core radiates insignificantly compared to the hot soot at the wings and due to self-absorption through the cool core such that the radiation reaching the wall only passes through cell 4 and 5.

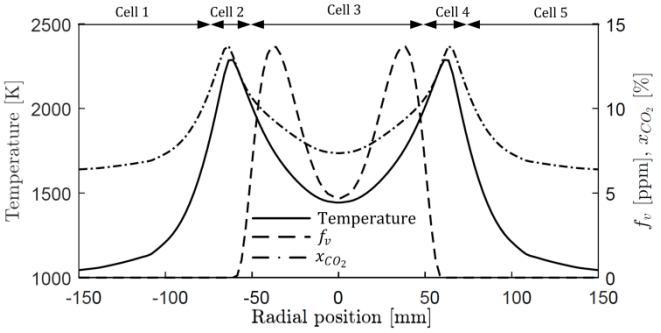

Figure 127: *Temperature profile and concentration profiles of soot and* CO_2 *in the self-similar part of the flame 60 mm downstream of the injector tip from the simulations presented in the previous section.*

Table 9: *Properties of the cells that describe the flame cross-section. The ambient gas resemble conditions with EGR corresponding to* $x_{\mathrm{O_2}} = 0.15$.

HITEMP2010	Cell 1	Cell 2	Cell 3	Cell 4	Cell 5
L [mm]	42	2	12	2	42
p_{amb} [bar]	60	60	60	60	60
T_{amb} [K]	1000	2200	1800	2200	1000
$x_{\mathrm{H_2O}}$ [−]	0.036	0.11	0.085	0.11	0.036
$x_{\mathrm{CO_2}}$ [−]	0.062	0.13	0.1	0.13	0.062

The flame emission through the line of sight through cell 1-4 can be seen in Figure 128. There is significant radiation from CO_2 between 4 and 5 µm where there is very little soot emission. This is due to the high emissivity of the 4.3 µm band of CO_2 while the soot emissivity is very low as can be seen in Figure 17. In addition the soot is at a lower temperature than the hottest part of the flame where the CO_2 and H_2O concentration is highest. Water vapor is more erratic radiating across the majority of the spectrum. Of special significance at high pressure is the band at 2.7 µm which is not that significant at atmospheric pressures as observed by Gore and Faeth [110]. The pressure broadening significantly increases the emissivity of this band.

The total radiance from the soot and gas through the flame cross-section can be calculated by integrating the spectrum in Figure 128 wrt wavelength.

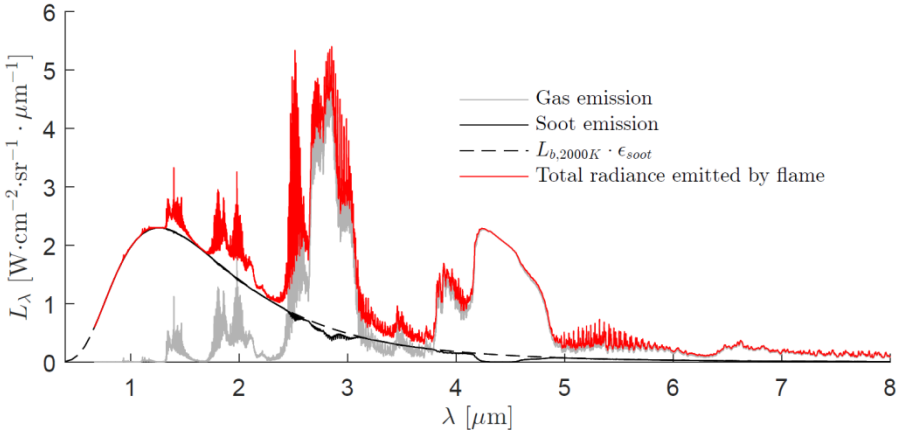

Figure 128: *Spectral radiance emitted by an n-dodecane spray flame at* $p_{\text{amb}} = 60$ bar, $T_{\text{amb}} = 1000$ K *and* $x_{O_2} = 0.15$ *(*$x_{H_2O} = 0.036$ *and* $x_{CO_2} = 0.062$*) calculated using molecular spectra from the HITEMP2010 database* **[9]** *and soot emissivity estimated from Eq. (27).*

The radiance from the gas is found to be $L_{\text{gas}} = 4.68\ \text{W} \cdot \text{cm}^{-2} \cdot \text{sr}^{-1}$ and $L_{\text{soot}} = 3.78\ \text{W} \cdot \text{cm}^{-2} \cdot \text{sr}^{-1}$, showing that the radiative emission from the gas and soot are comparable in magnitude. To get the total radiant flux from the flame, the flame geometry needs to be taken into account as seen in Eq. (69).

$$\Phi = A2\pi \int L_\lambda d\lambda \tag{69}$$

Where A is the area of the flame and 2π is the integral $\int d\Omega$ for a hemisphere. As seen in the profiles in Figure 127 and schlieren measurements under reacting conditions in Figure 119 a), the hottest part of the flame, where mixture conditions are close to stoichiometric, is located outside the soot in the flame. The area from which the majority of the gas radiation is emitted is then larger than the area from which the majority of soot radiation is emitted. In addition, the flame upstream of the soot inception zone is completely dominated by gas radiation. These observations suggest that the majority of the radiative heat loss will stem from gas radiation.

However, the radiance observed at the wall depends largely upon the amount of EGR as a very large portion of the gas emission is absorbed by the bulk gas before reaching the wall due to the high concentrations of CO_2 and H_2O. It is mostly hot lines that reach the wall because the bulk gas has a lower temperature and therefore a lower emissivity in the spectral regions where the hot lines appear. This is especially apparent in the CO_2 band at 4.3 µm where the tightly spaced lines close to the band origin are essentially opaque, leading to the wall seeing black body radiation at 1000 K, while the hot lines resulting from a broader population of states are not absorbed and appear further away from the band origin on either side. Hot lines from H_2O are more erratic and appear all over the spectrum.

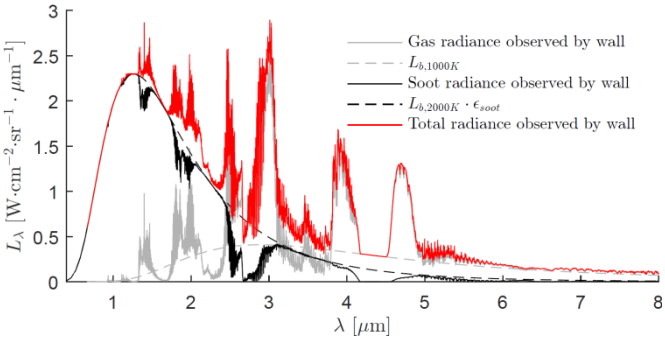

Figure 129: *Spectral radiance observed by the wall from a from an n-dodecane spray flame at* $p_{\text{amb}} = 60$ bar, $T_{\text{amb}} = 1000$ K *and* $x_{O_2} = 0.15$ *(*$x_{H_2O} = 0.036$ *and* $x_{CO_2} = 0.062$*) calculated using molecular spectra from the HITEMP2010 database* **[9]** *and soot emissivity estimated from Eq. (27).*

With no EGR the ambient gas only contains trace amounts of H_2O and CO_2 ($x_{H_2O} = 0.0014$ and $x_{CO_2} = 0.0004$) in a lot more of the gas radiation reaching the wall. It can be seen that the CO_2 emission band at 4.3 µm is well above the Planck curve at 1000 K and that the H_2O band at 2.7 µm is significant. Thus, the radiative heat loss will be larger with no EGR due to the radiative emission from the gas not being absorbed in the bulk gas.

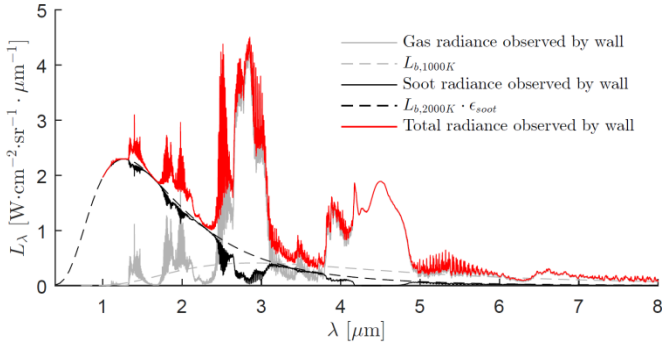

Figure 130: *Spectral radiance observed by the wall from a from an n-dodecane spray flame at* $p_{\text{amb}} = 60$ bar, $T_{\text{amb}} = 1000$ K *and* $x_{O_2} = 0.21$ *(*$x_{H_2O} = 0.0014$ *and* $x_{CO_2} = 0.0004$*) calculated using molecular spectra from the HITEMP2010 database* **[9]** *and soot emissivity estimated from Eq. (27).*

Conclusions

The outline of this work starts by building a foundation of the physiochemical and electromagnetic interactions in flames of which optical combustion diagnostic methods are based. First-hand practical examples of baseline diagnostics are reviewed to show how these optical methods can isolate and measure certain physical properties of the flames. Consequently, the experimental and interpretative complexities involved are implicit. The properties of liquid spray flames, the type of flame studied in this work, have also been discussed leading to the motivation for the choice of diagnostic methods to apply.

Experiments have been carried out in a constant volume combustion chamber located at Sandia's combustion research facility. The vessel is optically accessible and able to generate environments with well-defined boundary conditions and high reproducibility, in which to inject a fuel spray. The environments generated are designed to resemble those inside a diesel engine combustion chamber.

An experimental setup for preforming extinction based imaging measurements with high temporal resolution in optically harsh environments has been developed. The general illumination characteristics needed to isolate attenuation of light by scattering and absorption from light displaced due to gradients in the refractive index through the combustion chamber, have been identified. The optical setup maximizes the light throughput, thereby enhancing high temporal resolution capabilities, while still fulfilling these illumination criteria. Practical considerations concerning corrections for camera behavior, filtering induced artifacts and post processing methods that arise when applying this diagnostic have been addressed. The setup was a large improvement of previous extinction imaging setups applied to spray flames and is to be introduced as the standard optical setup for extinction imaging within the Engine Combustion Network.

This diagnostic, in combination with others, were applied to measure spray and combustion characteristics of two nozzles specifically machined to isolate the effects from in-nozzle cavitation. The experimental results reveal that there are differences in the spray immediately outside the injector when cavitation interactions occur inside the nozzle. The difference in the break-up process is discernable in the liquid boundary measurements where the spray from the cavitating nozzle has a wider dispersion angle immediately outside the nozzle. However, few millimeters downstream the dispersion angles become very similar and remain fairly constant, indicating flow with self-similar scaling. Comparison of many distinguishing features of the two sprays show consistency when referenced to where the sprays attain a fully developed self-similar flow. Liquid length, lift-off length, and the jet outer boundary all collapse.

The mixture field and liquid boundary modelled using a steady jet assumption and mixing limited vaporization based on measured vapor/liquid boundaries predicts that in fact the difference in liquid penetration distance is 4 mm. The higher entrainment rate immediately outside the cavitating nozzle affects the mixture field such that the lift-off location shifts closer to the nozzle, discernable from modelled stoichiometric mixture contours and observed in measurements. The enhanced spray break-up induced by cavitation does not seem to have a radical effect then. Rather a shortening of the break-up length such that the spray/jet attains a fully developed flow closer to the nozzle. The fully developed spray however does show consistency and is therefore easier to tackle from a modelling point of view, while the physics in the break-up zone may be most challenging.

The soot cloud from these wide bore nozzles is so optically thick that the flame appears opaque to the image acquisition at temperatures above 1000 K. At temperatures above 1000 K the optical thickness is measureable in the initial formation stage (soot inception zone). The soot volume fraction has been determined in these regions. From combining chemiluminescence and soot volume fraction measurements information of the flame structure can be deducted. The flame structure agrees well with Pickett and Siebers's adaptation of Flynn et. al.'s conceptual model where a soot precursor formation zone separates the rich partially premixed flame at the lift-off location from the soot inception zone. The soot inception zone forms soot wings that merge further downstream. The shape of the wings and the length to where they merge is largely dependent on the mixing and temperature distribution governed by the local velocity profile. The soot volume fraction is very high, >20 ppm, and the optical path length is long when the soot wings merge. Thus, it is not surprising that the flame appears opaque to an acquisition system able to measure an optical thickness of up to 4.

The soot inception zone is generally located closer to the nozzle for Spray C and the merging of the soot wings occur over shorter distances indicating higher axial velocities and poorer mixing along the central axis for Spray D. This is mostly due to the cavitating nature of Spray C and partly due to that the spray momentum for Spray D is slightly higher.

Spray D has been modelled with CFD showing good agreement between flow, penetration characteristics, lift-off length and soot formation. The measured optical thickness and soot volume fraction in regions with no measurement saturation was used to compare model with experiments. The translation of modelled soot volume fraction to optical thickness reveals a potential optical thickness of the flame at 635 nm of up to 50, which is impossible to measure.

A simple analysis of the radiative emission from a spray flame, based on the simulation of Spray D, reveals that the majority of emission from the flame comes from H_2O and CO_2. However, the presence of these components in the bulk gas during EGR conditions significantly reduces the amount of gas radiation reaching the wall and contributing to heat loss. Under such conditions radiative emission from soot may dominate the radiative heat loss.

Overall, this work emphasizes the extreme complexities involved in applying optical measurements in complex,

transient, turbulent, multi-phase, spray flames in diesel engine-like environments. However, optical arrangement and filtering, processing methods, corrections for camera non-idealities and important acquisition considerations have been deliberated here showing that refinement of these elements increases accuracy of the measurements and provides a deeper understanding of the limitations of the techniques.

Future work

Through this work the extinction imaging diagnostic has been refined to the degree where new sources of measurement artifacts have come to light. The reflections seen in the measurements can be significantly reduced by applying absorptive rather than reflective filters. The diffuseness of the light however, increases the possibility for internal reflections in the camera objective. These reflections are extremely difficult to identify as they themselves are diffused and further work on a correction for these reflections is needed. The best suggestion is to use a ray tracing software like ZEMAX to get an idea of the magnitude and pattern of the diffused internal reflections such that a correction can be approximated. Further tests of the diagnostic with different geometrical constraints in different experimental facilities need to be investigated.

Perform spectral extinction analysis of laminar premixed and non-premixed flames from the UV to the infra-red to investigate the radiative properties of gases and particulates and the optical properties of soot.

The development of a stationary spray flame in atmospheric conditions has been initiated in this works. This type of flame will open up for long exposure measurements and the ability to analyze these flames in the infra-red.

Regarding the spray C and D injectors manufactured with the aim of isolating the influence of in-nozzle cavitation, non-reacting measurements of the liquid and vapor phase across a larger sweep of ambient conditions may reveal additional information as to the qualitative differences between the sprays. Microscopy or ballistics imaging resolving droplet size distributions could be of use to study the near nozzle differences and X-ray tomography can identify the penetration of the coherent liquid core. These results will aid in validating the fine LES simulations of the internal and near nozzle flow. This research is important in order to confidently model the break-up of sprays, thereby accurately predicting the transition to the fully developed flow which is seemingly fairly predictable.

As the optical thickness of the soot cloud from spray C and D is so high, the only hope of measuring it is to use a longer wavelength of illumination. The soot cloud appears optically thinner at longer wavelengths. However, the soot luminosity is significantly higher in the near-infrared.

As the soot luminosity is stronger, the illumination source also needs to be much more intense, which may be difficult. In addition, sensors at these wavelengths are slow and the combination of strong soot luminosity and low temporal resolution can lead to large local errors due to the movement of the flame. By moving further into the far-infrared the luminosity decreases again. At these wavelengths the challenge may be finding an illumination source that is significantly brighter than the flame.

More detailed modelling of the radiation in spray flames incorporating detailed estimates of the soot and molecular spectral emissivity. The increasing accuracy of predicative models will allow for calculating radiative heat transfer via the discrete radiative transfer equations.

Acknowledgements

I would like to acknowledge the Danish Strategic Research Council and MAN Diesel & Turbo for providing funding for this work. I would also like to acknowledge the Combustion Research Facility, Sandia National Laboratories, Livermore, CA. Support was provided by the U.S. Department of Energy, Office of Vehicle Technologies where the experimental work was carried out. Sandia is a multiprogram laboratory operated by Sandia Corporation, a Lockheed Martin Company, for the United States Department of Energy's National Nuclear Security Administration under contract DE-AC04- 94AL85000.

I would also like to thank my supervisors Anders Ivarsson and Jesper Schramm. Anders Ivarsson deserves special thanks for dedicating many hours to healthy discussion and providing me with guidance.

I would like to express my gratitude to Lyle Pickett, Scott Skeen, Julien Manin and Keith Penney from Sandia National Laboratories for hosting me during my stay in the US and for taking the time to provide me with guidance technical support and access to their broad competences. It has been a pleasure working with them and I look forward to a continuing cooperation.

I am grateful to Michele Battistoni from the University of Perugia for contributing with LES modelling of the internal flow in the investigated nozzles.

I am grateful to my colleague Kar Mun Pang from the Technical University of Denmark for providing me with RANS simulations of the spray/jet incorporating chemical kinetics and soot modelling.

Works Cited

[1] Ivarsson, A. and Schramm, J. *RADIADE.* http://www.radiade.mek.dtu.dk/.

[2] Sandia National Laboratories. 03 27, 2015. http://www.sandia.gov/ecn/.

[3] Modest, F. M. *Radiative heat transfer.* San Diego: Academic Press, 1993.

[4] Laboratory, National Renewable Energy. 2015. www.nrel.gov.

[5] Nordmann, Stephan. "Light absorption of atmospheric soot particles over central Europe." Dissertation, University of Leipzig, 1982, 102.

[6] Economist, The. "The melting north." *Special report*, June 16, 2012.

[7] Taine, J. and Soufiani, A. "Gas IR radiative properties: From spectroscopic data to approximate models." *Advances in Heat Transfer* (Academic Press) 33 (1999): 295-414.

[8] Herzberg, G. *Molecular spectra and molecular structure.* Vol. II. Princeton, NJ: Van Nostrand, 1950.

[9] Rothman, L. S., Gordon, I. E., Barber, R. J., Dothe, H., Gamacje, R. R., Goldman, A., Perevalov, V. I., Tashkun, S. A., Tennyson, J. "HITEMP, the high-temperature molecular spectroscopic database." *Journal of Quantitative Spectroscopy & Radiative Transfer* 111 (2010): 2139-2150.

[10] Hottel, H. C. and Sarofim, A. *Radiative Transfer.* McGraw Hill Book, 1967.

[11] Mie, G. "Beiträge zur Optik trüber Medien, speziell kolloidaler Metallösungen." *Annalen der Physik* 330, no. 3 (1908): 377–445.

[12] Bohren, C. F., and Huffman, D. R. *Absorption and Scattering of light by small particles.* John Wiley & Sons, Inc., 1983.

[13] Pugmire, R. J., Yan, S., Ma, Z., Solum, M. S., Jiang, Y. J., Eddings, E. G. "Soot Formation Process." University of Utah: Department of Chemical & Fuels Engineering, Department of Chemistry.

[14] Millikan, R. C. "Optical properties of soot." *Optical Society of America* 51, no. 6 (1961): 698-699.

[15] Skeen, S. A., Manin, J., Dalen, K., and Pickett, L. M. "Extinction-Based Imaging of Soot Processes over a Range of Diesel Operating Conditions." *8th US National Combustion Meeting.* Salt Lake City, Utah, 2013.

[16] Hovarth, H. "Atmospheric light absorption - a review." *Atmospheric Environment* 27A, no. 3 (1993): 293-317.

[17] K.C. Smyth and C.R. Shaddix. "The elusive history of m=1.57-0.56i for the refractive index of soot." *Combustion and Flame* 107, no. 3 (1996): 314-320.

[18] D'Alessio, A., Di Lorenzo, A., Berretta, F., and Venitozzi, C.,. "Optical and chemical investigations on fuel-rich methane-oxygen premixed flames at atmospheric pressure." *Symposium (International) on Combustion.* Pennsylvania: Elsevier Inc., 1972. 941-953.

[19] Santoro, R. J., Semerjian, H. G., and Dobbins, R. A.,. "Soot particle measurements in diffusion flames." *Combustion and Flame*, no. 51 (1983): 203-218.

[20] Ku, J. C. and Felske, J. D. "Determination of refractive indices of mie scatterers from Kramers-Kronig analysis of spectral extinction data." *The Optical Society of America* 3, no. 5 (1986): 617-623.

[21] Charalampopoulos, T. T., and Chang, H. "In situ optial peoperties of soot particles in the wavelength range from 340 nm to 600 nm." *Combustion Science and Technology* 59, no. 4-6 (1988): 401-421.

[22] Chang, H., and Charalampopoulos, T. T. "Determination of the wavelength dependence of refractive indices of flame soot." *Proceedings of the Royal Society A* 430, no. 1880 (1990): 577-591.

[23] Charalampopoulos, T. T., and Felske, J. D. "Refractive indices of soot particles deduced from in-situ laser light scattering measurements." *Combustion and Flame* 68, no. 3 (1987): 283-294.

[24] T.C. Williams, C.R. Shaddix, K.A. Jensen and J.M. Suo-Anttila. "Measurement of the dimensionless extinction coefficient of soot within laminar diffusion flames." *Internatianal Journal of Heat and Mass Transfer* 50, no. 7-8 (2006): 1616-1630.

[25] Farias, T. L., Köylü, Ü. Ö. and Carvalho, M. G. "Range of validity of the Rayleigh-Debye-Gans theory for optics of fractal aggregates." *Applied Optics* 35, no. 33 (1996): 6560-5667.

[26] Sorensen, C. M. "Light scattering by fractal aggregates: A review." *Aerosol Science and*

Technology 35, no. 2 (2001): 648-687.

[27] Charalampopoulos, T. T. and Chang, H. "Agglomerate parameters and fractal dimensions of soot using light scattering - effects on surfrace growth." *Combustion and Flame* 87, no. 1 (1991): 89-99.

[28] Samson, R. J., Mulholland, G. W. and Gentry, J. W. "Structural analysis of soot aggregates." *Langmuir* 3, no. 2 (1987): 272-281.

[29] Kerker, M. *The scattering of light and other electromagnetic radiaiton. Physical chemistry: A series of monographs.* Edited by E. M. Loebl. Vol. 16. New York, 1969.

[30] Goulay, F., Schrader, P. E. and Michelsen, H. A. "Effect of the wavelength dependence of the emissivity on the inferred soot temperatures measured by spectrally resolved laser-induced incandescence." *Appl. Phys. B* 100 (2010): 655-663.

[31] Musculus, M. P. B., Singh, S. and Reitz, R. D. "Gradient effects on two-color soot optical pyrometry in a heavy-duty DI diesel engine." *Combustion and Flame* 153 (2008): 216-227.

[32] Skeen, S. A., Manin, J., Pickett, L. M., Dalen, K. and Ivarsson, A. "Quantitative spatially resolved measurements of total radiation in high-pressure spray flames." *SAE Technical Paper 2014-01-1252*, 2014.

[33] Rothman, L. S., Gordon, I. E., Babikov, Y., Barbe, A., Benner, D. C., Bernath, P. F., Birk, M., Bizzocchi, L., Boudon, V., Brown, L. R. et. al. "The HITRAN2012 molecular spectroscopic database." *Journal of Quantitative Spectroscopy & Radiative Transfer* 130 (2013): 4-50.

[34] Alberti, M., Weber, R., Mancini, M., Fateev, A. and Clausen, S. "Validation of HITEMP-2012 for carbon dioxide and water vapour at high temperatures and atmospheric pressures in 450-7600 cm-1 spectral range." *Journal of Quantitative Spectroscopy & Radiative Transfer* 157 (2015): 14-33.

[35] Stull, V. R. and Plass, G. N. "Emissivity of dispersed carbon particles." *Journal of the Optical Society of America* 50, no. 2 (1960): 121-129.

[36] Griffitths, P. R. *Fourier transform infrared spectroscopy.* Wiley & Sons Inc., 1986.

[37] Raspollini, P., Ade, P., Carli, B., and Ridolfi, M. "Corretion of instrument line-shape distortions in Fourier transform spectroscopy." *Applied Optics* 37, no. 17 (1998): 3697-3704.

[38] Ivarsson, A. *Modeling of heat release and emissions from droplet combustion of multi component fuels in compression ignition engines.* Ph. D. thesis, Kgs. Lyngby, Denmark: Technical University of Denmark (DTU), 2010, 111.

[39] Solomon, P. R., Best, P. E., Carangelo, R. M., Markham, J. R., Chien, P. L., Santoro, R. J., and Semerjian H. G. "FT-IR emission/transmission spectroscopy for in situ combustion diagnostics." *Symposium (Internatinal) on Combustion* (Symposium (International) on Combustion) 21, no. 1 (1988): 1763-1771.

[40] Best, P.E., Chien, P.L.a, Carangelo, R.M., Solomon, P.R., Danchak, M., and Ilovici, I. "Tomographic reconstruction of FT-IR emission and transmission spectra in a sooting laminar diffusion flame: Species concentrations and temperatures." *Combustion and Flame* 85, no. 3-4 (1991): 309-314.

[41] Musculus, M., and Pickett, L. M. "Diagnostic considerations for optical laser-extinction measurements of soot in high-pressure transient combustion environments." *Combustion and flame 141, Issue 4*, 2005: 371-391.

[42] Dobbins, R. A., Fletcher, R. A. and Chang, H. -C. "The evolution of soot precursor particles in adiffusion flame." *Combustion and Flame* 115 (1998): 285-298.

[43] Gaydon, A. G. and Wolfhard, H. G. *Flames - Their structure, radiation and temperature.* 3. London: Chapman and Hall ltd., 1970.

[44] Harathger, M. J., and Settles, G. S. "A comparison of three quatitative schlieren techniques." *Optics ans Lasers in Engineering*, no. 50 (2012): 8-17.

[45] Espey, C., Dec, J. E., Litzinger, T. A. and Santavicca, D. A. "Planar laser Rayleigh scattering for quantitative vapor-fuel imaging in a diesel jet." *Combusiton and flame* 109, no. 1-2 (1997): 79-86.

[46] Pickett, L. M., Manin, J., Genzale, C. L., Siebers, D. L., Musculus, M. P. B., and Idicheria, C. A. "Relationship Between Diesel Fule Spray Vapor Penetration/Dispersion and Local Fuel Mixture Fraction." *SAE Int. J. Engines 2011-01-0686* 4, no. 1 (2011): 764-799.

[47] Zetterberg, J., Li, Z., Afzelius, M. and Aldèn, M. "Two-dimensional temperature measurements in flames using filtered rayleigh scattering." *Applied spectroscopy* 62, no. 7 (2008): 778-783.

[48] Eckberth, A. C. *Laser diagnostics for combustion temperature and species.* 2nd. Amsterdam: CRC Press, 1996 (1988).

[49] Collin, R., Nygren, J., Richter, M. and Aldèn, M. "Simultaneous OH- and Formaldehyde-LIF measurements in an HCCI engine." *SAE Technical paper 2003-01-3218*, 2003.

[50] Bladh, H. and Bengtson, P.-E. "Characteristics of laser-induced incandescnce from soot in studies of a time-dependent heat- and mass-tranfer mode." *Applied Physics B* 78 (2004): 241-248.

[51] Axelsson, B., Collin, R. and Bengtson, P. -E. "Laser-induced incandescence for soot particle measuremetns in premixed flames." *Applied Optics* 39, no. 21 (2000): 3683-3690.

[52] Siebers, D. L. and Pickett, L. M. "Injection pressure and orifice diamter effects on soot in DI diesel fuel jets." Chap. 3 in *Thermo- and Fluid Dynamic Processes in Diesel Engines 2*, edited by J. H., Payri, F., Arcoumanis, C. and Desantes, J. M. Whitelaw, 109-132. Berlin, Heidelberg: Springer Berlin Heidelberg, 2002.

[53] Ohnesorge, W. "Die bildung von tropfen an Düsen und die auflösung flüssinger strahlen." *Zeitschift für angewandte Mathematik und Mechanik* 16, no. 6 (1931): 355-358.

[54] Baumgarten, C. *Mixture formation in internal combustion engines.* Springer Berlin Heidelberg, 2006.

[55] Kuo, K. K., and Acharya R. *Fundamentals of turbulent and multi-phase combustion.* Hoboken, New Jersey: John Wiley & Sons, Inc., 2012.

[56] Faeth, G. M., Hsiang, L. P., and Wu, P. K. "Structure and breakup properties pf sprays." *Int. J. Multiphase Flow* 21 (1995): 99-127.

[57] Westlye, F. R., Battistoni, M., Skeen, S., Manin, J., Pickett, L. M. "Penetration and combustion characterization of cavitating and non-cavitating fuel injectors under diesel engine conditions." *SAE Technical Paper 2016-01-0860*, 2016.

[58] Tamaki, N., Shimizu, M., Nishida, K., and Hiroyasu, H. "Effects of Cavitation and Internal Flow on Atomization of a Liquid Jet." *Atomization and Sprays* 8 (1998): 179-197.

[59] Saito, K., and Sato, Y. "Unstable Cavitation Behaviour in a Circular-Cylindrical Orifice Flow." *JSME International Journal* Series B, 45, no. 3 (2002): 638-645.

[60] Sou, A., Hosokawa, S., and Tomiyama, A. "Effects of Cavitation In a Nozzle on Liquid Jet Atomization." *International Journal of Heat and Mass Transfer*, 2007: 3575-3582.

[61] Schmidt, D. P., and Corradini, M. L. "The Internal Flow of Diesel Fuel Injector Nozzles: A Review." *International Journal of Engine Research* 2, no. 1 (2001): 1-22.

[62] Chaves, H., Knapp, M., Kubitzek, A., Obermeier, F., and Schneider, T. "Experimental Study of Cavitation in the Nozzle Hole of Diesel Injectors Using Transparent Nozzles." *SAE Technical Paper 950290*, 1995.

[63] Suh, H. K., and Lee, C. S. "Effect of Cavitation in Nozzle Orifice on the Diesel Fuel Atomization Charactereistics." *International Journal of Heat and Fluid Flow* 29 (2008): 1001-1009.

[64] Soteriou, C., Andrews, R., and Smith, M. "Direct Injection Diesel Sprays and the Effect of Cavitation and Hydraulic Flip on Atomization." *SAE Technical Paper 950080*, 1995.

[65] Nishiwaki, N. "Kinetics of liquid combustion process: Evaporation and ignition lag of fuel droplets." *5th Symposium (International) on Combustion.* NewYork: Reinhold, 1955. 148-158.

[66] Siebers, D. L. "Scaling Liquid-Phase Fuel Penetration in Diesel based on mixing-limited vaporization." *SAE Technical Paper 1999-01-0528*, 1999.

[67] Faeth, G. M. "Current status of droplet and liquid combusiton." *Progress in Energy and Combustion Science* 3, no. 4 (1977): 191-224.

[68] Belland, J. and Harstad, K. "The details of convective evaporation of dense and dilute clustersof droplets." *International Journal of Heat and Mass Transfer* 30, no. 6 (1987): 1083-1093.

[69] Chehroudi, B., Cohn, R., Talley, D. "Cryogenic shear layers: Experiments and phenomenological modelling of the initial growth rate under subcritical and supercritical conditions." *Heat and Fluid Flow*, no. 23 (2002): 554-563.

[70] Woodward, R. D. and Talley, D. G. "Raman imaging of transcritical cryogenic propellants." *American Institute of Aeronautics and Astronautics, Paper 96-0468*, 1996.

[71] Siebers, D.L. "Liquid-phase fuel penetration in diesel sprays." *SAE Technical Paper Series 980809*, 1998.

[72] Westlye, F. *Review and modelling of diesel spray.* Report in partial fullfillment for the degree of PhD, DTU, 2016.

[73] Musculus, M. P. B., and Kattke, K. "Entrainment waves in diesel jets." *SAE Int.J.Engines 2009-01-1355* 2, no. 1 (2009): 1170-1193.

[74] Naber, J. D., and Siebers, D. L. "Effects of Gas Density and Vaporization on Penetration and Dispersion of Diesel Sprays." *SAE Technical Paper 960034*, 1996.

[75] Hiroyasu, H. and Arai, M. "Structures of fuel spray in diesel engines." *SAE 9000475*, 1990.

[76] Payri, R., Gimeno, J., Cuisano, J. and Arco, J. "Hydraulic characterization of diesel engine single-hole injectors." *Fuel* 180 (2016): 357-366.

[77] Kastengren, A. L., Powell, C. F., Wang, Y. J., Im, K. S. and Wang, J. "X-ray radiography measurements of diesel spray structure at engine-like ambient density." *Atomization and Sprays* 19 (2009): 1031-1044.

[78] Westlye, F. R. "Review and modelling of diesel spray." 7.5 ECTS special course for partial fulfillment of the degree of Pd. D., Kgs. Lyngby, 2016.

[79] Flynn, P. F., Durett, R. P., Hunter, G. L., Akinyemi, O. C., Dec, J. E., and Westbrook, C. K. "Diesel combustion: An integrated view combining laser diagnostics, chemical kinetics and empirical validation." *SAE Technical Paper 1999-01-0509*, 1999.

[80] Siebers, D. L., Higgins, B. "Flame Lift-off on Direct-Injection Diesel Sprays Under Quiescent Conditions." *SAE Technical paper 2001-01-0530*, 2001.

[81] Pickett, L. M. and Siebers, D. L. "Soot formation in diesel fuel jets near the lift-off length." *Int. J. Engine Res.* 7 (2005): 103-130.

[82] Skeen, S. A., Manin, J. and Pickett, L. M. "Simultaneous formaldehyde PLIF and high-speed schlieren imaging for ignition visualization in high-pressure spray flames." *Proceedings of the Combustion Institute* 35 (2015): 3167-3174.

[83] C. Crua, D.A. Kennaird and M.R. Heikal. "Laser-induced incandescence study of diesel soot formation in a rapid compression machine at elevated pressures." *Combustion and Flame* 135 (2003): 475-488.

[84] Pickett, L. M. and Siebers, D. L. "Soot in fuel jets: Effects of ambient temperature, ambient density, and injection pressure." *Combustion and Flame* 138 (2004): 114-135.

[85] inside, LED. *LEDinside.* 09 01, 2016. http://www.ledinside.com/knowledge/2015/9/sandia_led_pulser_delivers_laser_like_performance_at_a_fraction_of_the_cost (accessed 04 01, 2016).

[86] Westlye, F. R., Penney, K., Skeen, S., Manin, J., Pickett, L.M., and Ivarsson, A. "Experimental Setup for High Temporal Diffuse Back-Illumination Measurements." *Applied Optics (submitted)*, 2016.

[87] McCluney, W.R. *Introduction to Radiometry and Photometry, 2nd Edition.* Artech House, Inc., 2014.

[88] Carlen, C. USA Patent application number 14/998,101. 2015.

[89] Kook, S. and Pickett, L. "Soot volume fraction and morphilogy of conventional, Fischer-Tropsch, coal-derived and surrogate fuel at diesel conditions." *SAE Int. J. Fuels & Lubr.* 2, no. 5 (2012): 647-664.

[90] Ghandhi, J.B. and Heim, D. M. "An optimized optical system for backlit imaging." *Review of Scientific Instruments*, 2009.

[91] Manin, J., Pickett, L. M., and Skeen, S. A. "Two-Color Diffused Back-Illumination Imaging as a Diagnostic for Time-Resolved Measurements in Recting Sprays." *SAE Int. J. Engines* 6, no. 4 (2013): 1908-1921.

[92] Pickett, L. M., Genzale, C. L., Manin, J., and Malbec, L. M. "Measurement uncertainty of liquid penetration in evaporating diesel sprays." *23rd Annual Conference on Liquid Atomization and Spray Systems*, 2011.

[93] Manin, J., Bardi, M., and Pickett, L. M. "Evaluation of the liquid length via diffused back-illumination imaging in vaporizing diesel sprays." *COMODIA*, 2012.

[94] Facility, Sandia National Laboratories: Combustion Research. *Combustion Research Facility.* Department of Energy Office of Science. 2016. http://crf.sandia.gov/.

[95] Bardi, M., Brunaux, G. and Malbec, L. M. "Study of eCN injectors' behavior repeatability with focus on aging effects and soot fluctuations." *SAE Technical*

Paper 2016-01-0845, 2016.

[96] Davidson, J. A., Cantrell, C. A., McDaniel, A. H., Shetter, R. E., Madronich, S. and Calvert, J. G. "Visible-ultraviolet absorption cross sections for NO2 as a function of temperature." *Journal of Geophysical Research* 93, no. D6 (1988): 7102-7112.

[97] Kastengren, A. L., Tilocco, F. Z., Powell, C. F., Manin, J., Pickett, L. M., Payri, R., and Bazyn, T. "Engine Combustion Network (ECN): Measurements of Nozzle Geometry and Hydraulic Behavior." *Atomization and Sprays* 22, no. 12 (2012): 1011-1052.

[98] Wiener, N. *Extrapolation, Interpolation and Smoothing of Stationary Time Series Vol. 2.* Cambridge, MA: MIT press, 1949.

[99] Higgins, B., and Siebers, D. L. "Measurement of the Flame Lift-off Location on DI Diesel Sprays Using OH Chemiluminescence." *SAE Technical Paper 2001-01-0918*, 2001.

[100] Lillo, P. M., Pickett, L. M., Persson, H., Andersson, O., Kook, S. "Diesel Spray Ignition Detection and Spatial/Temporal Correction." *SAE Int. J. Engines 2012-01-1239* 5, no. 3 (2012): 1330-1346.

[101] Lopez, J., and Pickett, L. M. "Jet/wall interaction effects on soot formation in a diesel fuel jet." *COMODIA.* Yokohama, Japan, 2004.

[102] D. Sun, S. Roth and M.J. Black. "Secrets of optical flow estimation and their principles." *IEEE Conference on Computer Vision and Pattern Recognition (CVPR).* San Francisco, CA, 2010.

[103] Zhang, A., Montanaro, A., Allocca, L., Naber, J. and Lee, S. Y. "Measurement of Diesel Spray Formation and Combustion upon Different Nozzle Geometry using Hybrid Imaging Technique." *SAE Int.J.Engines 2014-01-1410* 7, no. 2 (2014): 1034-1043.

[104] Abramovich, G. N. *The theory of turbulent jets.* Cambridge: M. I. T. Press, 1963.

[105] Lemmon, E. W., Huber, M. L., McLinden, M. O. "NIST Standard Reference Database 23: Reference Fluid Thermodynamic and Transport Properties-REFPROP, Version 9.1." 2013.

[106] Som, S., Longman, D. E., Luo, Z., Plomer, M. and Lu, T. "Tree dimensional simulations of diese sprays using n-dodecane as a surrogate." *Fall technical meeting of the eastern states section of the combustion institute. 2011.* 2011.

[107] Pang, K. M., Jangi, M., Bai, X. S. and Schramm, J. "Evaluation and optimization of phenomenological multi-step soot model for spray combusiton under diesel engine-like operating conditions." *Combustion Theory and Modelling* 19, no. 3 (2015): 279-308.

[108] Pang, K. M., Karvounis, N., Walther, J. H. and Schramm, J. "Numerical investigation of soot formation and oxidation processes under large two-stroke marine diesel engine-like conditions using integrated CFD-chemical kinetics." *Applied Energy* 169 (2016): 874-887.

[109] S. A. Skeen, J. Manin, L. M. Pickett, E. Cenker, G. Bruneaux, K. Kondo, T. Aizawa, F. R Westlye, K. Dalen, A. Ivarsson, et. al. "A progress review on soot experiments and modelling in the engine combustion network (ECN)." *SAE Technical Paper 2016-01-0734*, 2016.

[110] Gore, J. P. and Faeth, G. M. "Structure and spectral radiation properties of turbulent ethylene/air diffusion flames." *21st Symposium (International) on Combustion*, 1986: 1521-1531.

Appendix

Review and modelling of diesel spray

By

Fredrik Westlye

Report submitted in partial fulfillment of the degree of Ph. D.

Department of Mechanical Engineering
Technical University of Denmark
DK-2800, Kgs. Lyngby
Denmark

Kgs. Lyngby June 2016

Introduction

The properties of liquid fuel sprays are governed by nozzle geometry, fuel and flow properties. This report is a parametrical investigation of liquid fuel sprays with the goal of designing a stationary fuel spray injected into an atmospheric ambient. The fuel spray should resemble that of a diesel fuel spray at high ambient pressure and temperature. A typical diesel injection event spans over a few milliseconds. Performing measurements on these types of flames requires high speed diagnostics. This requirement excludes various diagnostic methods, e. g. methods based in the infra-red wavelength range as these diagnostics are limited to relatively low temporal resolution. A stationary fuel spray will enable diagnostic flexibility in the form of long integration times, averaging over turbulent fluctuations.

Spray break-up

A liquid spray injected into a gaseous environment will experience shear forces acting upon the liquid interface, causing surface instabilities eventually causing the liquid core to break-up into ligaments and droplets. This process is governed by the relative velocity between the liquid and surrounding gas, fuel properties and nozzle geometry. Ohnesorge showed that the break-up process of liquid injected into a gaseous environment can be described by the Reynolds number and Weber number [1], Eq. (1) and (2) respectively.

$$Re = \frac{U \cdot d}{\nu} \tag{1}$$

$$We = \frac{U^2 \cdot d \cdot \rho}{\gamma} \tag{2}$$

To remove the velocity dependence, Ohnesorge defined the Ohnesorge number as Eq. (3) and mapped the different break-up processes of liquid sprays in a diagram of Oh vs. Re as seen in Figure 1.

$$Oh = \frac{\sqrt{We}}{Re} = \frac{\nu \cdot \sqrt{\rho}}{\sqrt{\gamma \cdot d}} \tag{3}$$

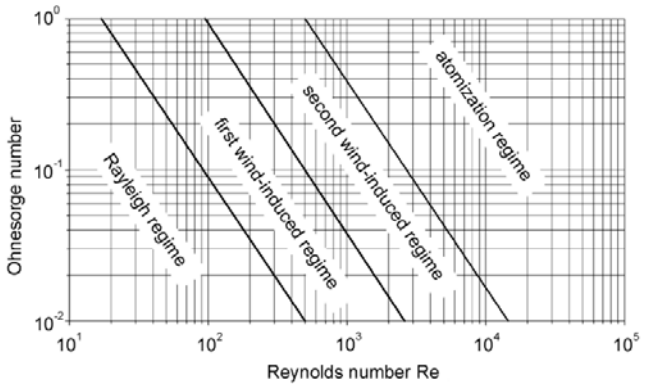

Figure 1: *Ohnesorge diagram mapping different spray break-up regimes through various nozzle, flow and fluid properties* **[2]**.

The break-up regimes identified in the diagram are illustrated in Figure 2.

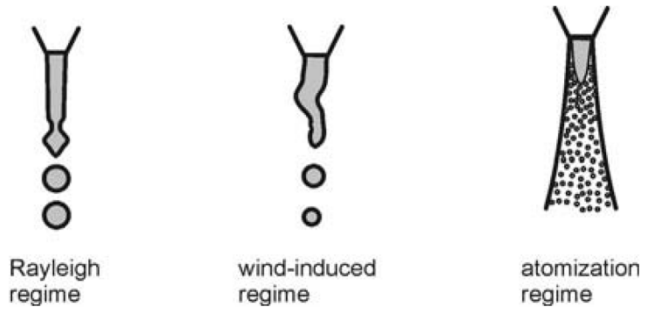

Figure 2: *Illustrations of different spray break-up regimes* **[2]**.

In the Rayleigh breakup regime surface tension forces are dominant and no fine spray is formed. A laminar liquid stream issues from the injector which perturbs a ways downstream. The perturbations grow, eventually forming a large droplet that breaks off at the tip. In the wind-induced regime the flow is turbulent and aerodynamic forces play a larger role. Interfacial shear forces overcome the surface tension of the fuel, deforming the liquid boundary causing small droplets to break-off until the liquid core disintegrates. In the atomization regime the break-up process starts at the immediate nozzle exit. The shear forces acting on the liquid/gas interface are much greater leading to the formation of ligaments and droplets along the liquid core. This process is commonly referred to as primary breakup. Similarly, the further breakup of these ligaments into smaller spherical droplets is referred to as secondary breakup, indicated in the illustration in Figure 3. The formation of smaller droplets enhances the evaporation process as the liquid/gas interface area drastically increases.

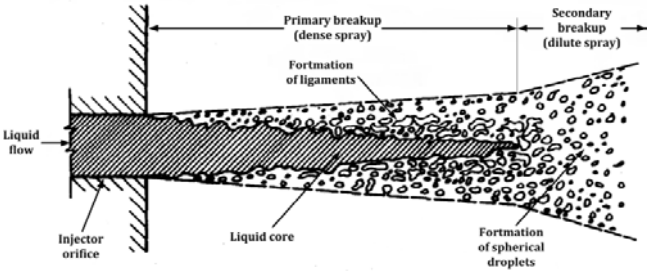

Figure 3: *Illustration of near-nozzle primary and secondary breakup processes* [3].

In spray combustion applications the spray is atomized as the chemical reaction times are orders of magnitude shorter than the evaporation and mixing processes. The characteristics of the spray then govern the combustion process.

As can be seen by the parameters defining the Ohnesorge and Reynolds number, the regime in which the break-up will reside is defined by the fuel properties and the nozzle geometry.

Atomizing stationary fuel spray

The isolated effect of the various properties governing the Ohnesorge and Reynolds number on the break-up process can be intuitively analyzed. As $Oh \propto \gamma^{-1/2}$, a lower surface tension will promote atomization. The kinematic viscosity affects both the dimensionless numbers, $Oh \propto \nu$ and $Re \propto \nu^{-1}$. Thus, a lower kinematic viscosity of the fuel increases the Reynolds number, promoting atomization, while the Ohnesorge number decreases, impeding atomization. However, the regime transition lines identified

by Ohnesorge are proportional to $Re^{-4/3}$ such that a lower kinematic viscosity will collectively promote atomization.

The fuel density only affects the Ohensorge number, $Oh \propto \rho^{-1/2}$, indicating that a high density fuel promotes atomization. However, for a constant mass flow the velocity U is proportional to ρ^{-1}, thereby a lower fuel density will promote atomization. Similarly, for a constant mass flow the velocity U is proportional to d^{-2}. Thus, $Re \propto d^{-1}$ while $Oh \propto d^{-1/2}$ indicating that the nozzle orifice is the most influential parameter promoting atomization.

In dimensioning a stationary spray flame it makes sense to dimension according to the heating value of the fuel. Experiments with a steady laminar flat flame burner revealed that a flame releasing 3.8 kW of heat was the limit to where a continuous flame was feasible [4]. The lower heating value of the fuel also becomes an important dimensioning criterion. The conditions for generating an atomized spray in an atmospheric ambient without exceeding a 3.8 kW heat release rate have been analyzed for a range of fuels. The fuels with their respective properties are listed in Table 1 in order of ascending kinematic viscosity.

Table 1: *Properties from the NIST standard reference database* **[5]** *for selected fuels at* $\boldsymbol{T_f = 20°C}$.

Prop. / Fuel	$\rho\left[\frac{kg}{m^3}\right]$	$\nu\left[\frac{m^2}{s}\right]$	$\gamma\left[\frac{J}{m^2}\right]$	$LHV\left[\frac{MJ}{kg}\right]$
Dimethyl ether (C_2H_6O)	669.7	1.96E-7	1.16E-3	2.888
Propane (C_3H_8)	500.3	2.05E-7	0.76E-3	4.634
Butane (C_4H_{10})	578.8	2.88E-7	1.24E-3	4.572
Pentane (C_5H_{12})	625.8	3.64E-7	1.60E-3	4.535
Hexane (C_6H_{14})	659.4	4.74E-7	1.85E-3	4.510
Heptane (C_7H_{16})	683.8	6.12E-7	2.06E-3	4.493
Octane (C_8H_{18})	702.3	7.72E-7	2.17E-3	4.479
n-Dodecane ($C_{12}H_{26}$)	749.5	19.9E-7	2.54E-3	4.415

With the boundary condition $\dot{Q} < 3.8\ kW$ the mass flow, $\dot{m}$, is defined by Eq. (4).

$$\dot{m} = \dot{Q}/LHV \tag{4}$$

The fluid velocity is related to the mass flow through Eq. (5)

$$U = \frac{\dot{m}\cdot\rho}{C_a\cdot 4\cdot\pi\cdot d^2} \tag{5}$$

Where C_a, the area contraction coefficient, is defined as the ratio between the geometric orifice area and the effective orifice area [6], and is taken to be 0.8 in this study. The injection pressure needed to generate the desired flow conditions is calculated through the Bernoulli equation Eq. (6).

$$\Delta p = \frac{U^2\cdot\rho}{2} \tag{6}$$

The break-up characteristics for the fuels listed in Table 1 with an orifice diameter of $50\mu m$ and $30\mu m$ have been mapped in an Ohnesorge diagram in Figure 4

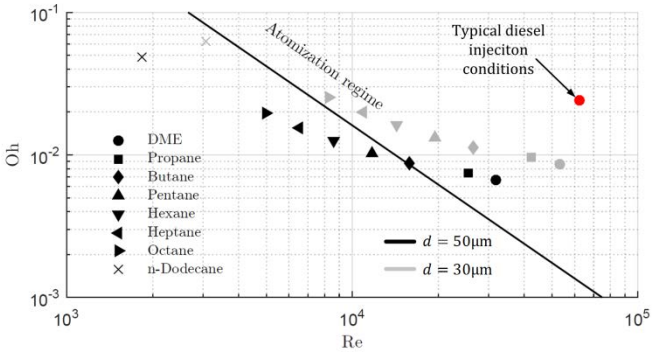

Figure 4: *Ohnesorge diagram for various fuels with the boundary condition that* $\boldsymbol{\dot{Q} < 3.8\ kW}$. *The effect of the nozzle diameter is shown. Also indicated is a typical diesel engine condition with a diesel like fuel (n-Dodecane),* $\boldsymbol{p_{inj} = 1500\ bar}$, $\boldsymbol{d = 100\mu m}$.

The injection parameters achieving the conditions mapped out in Figure 4 are listed in Table 2 and Table 3 for orifice diameter of $50\mu m$ and $30\mu m$ respectively.

Table 2: *Injection parameters through a* $\boldsymbol{50\mu m}$ *orifice with constant mass flow corresponding to a heat release rate of 3.8 kW.*

Fuel	$U\left[\frac{m}{s}\right]$	$\Delta p[bar]$	$\dot{m}\left[\frac{mg}{s}\right]$
DME	125.07	25.9	131.57
Propane	104.36	19.3	82.01
Butane	91.42	22.4	83.11
Pentane	85.24	24.2	83.80
Hexane	81.33	25.5	84.25
Heptane	78.74	26.4	84.59
Octane	76.91	27.1	84.85
n-Dodecane	73.11	29.0	86.08

Table 3: *Injection parameters through a* $\boldsymbol{30\mu m}$ *orifice with constant mass flow corresponding to a heat release rate of 3.8 kW.*

Fuel	$U\left[\frac{m}{s}\right]$	$\Delta p[bar]$	$\dot{m}\left[\frac{mg}{s}\right]$
DME	347.43	199.7	131.57
Propane	289.88	149.2	82.01
Butane	253.94	172.6	83.11
Pentane	236.77	186.6	83.80
Hexane	225.93	196.6	84.25
Heptane	218.73	203.9	84.59
Octane	213.64	209.4	84.85
n-Dodecane	203.10	223.5	86.08

It can be seen that the orifice diameter needs to be very small in order to achieve atomization of the spray with the low mass flow rate. The kinematic viscosity of the fuel is the most influential fuel property promoting atomization. The mapping of the different fuels in order of ascending kinematic viscosity clearly shows this trend. This means that increasing the fuel temperature will promote atomization. Consequently the

surface tension of the fuel also decreases with higher temperature, further promoting atomization as seen in Figure 5.

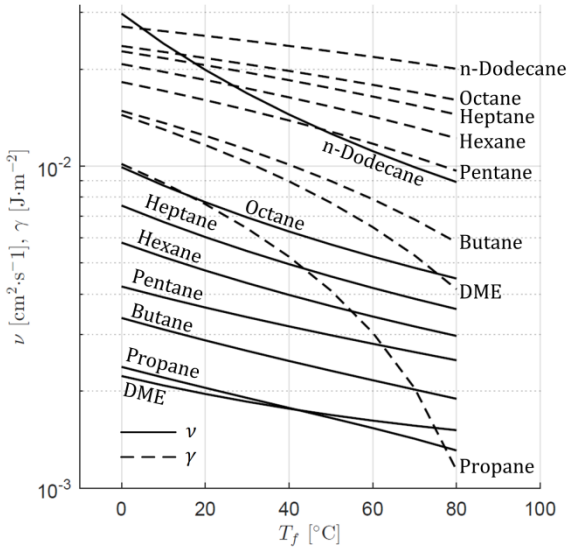

Figure 5: *Kinematic viscosity, $\boldsymbol{\nu}$, and surface tension, $\boldsymbol{\gamma}$, of the respective fuels as function of fuel temperature, $\boldsymbol{T_f}$* **[5]**.

It should be noted that DME is an exotic fuel containing an oxygen atom giving it slightly different properties than the other conventional hydrocarbons. In addition, the heating value is significantly lower, allowing larger mass flow and consequently higher velocity. This fuel might not be suitable for recreating a diesel like flame due to the chemical composition altering the combustion characteristics. The ideal fuel that can achieve atomization is propane which is able to atomize even with a nozzle diameter of $50\,\mu m$. This is important as machining micro orifice nozzles is not a trivial task and larger orifices are easier to manufacture. It can be seen in Table 2 and Table 3 that the injection pressures are moderate and can be achieved with conventional pumps.

Stationary fuel spray/jet

The classic fluid mechanical representation of a turbulent free jet is illustrated in Figure 6.

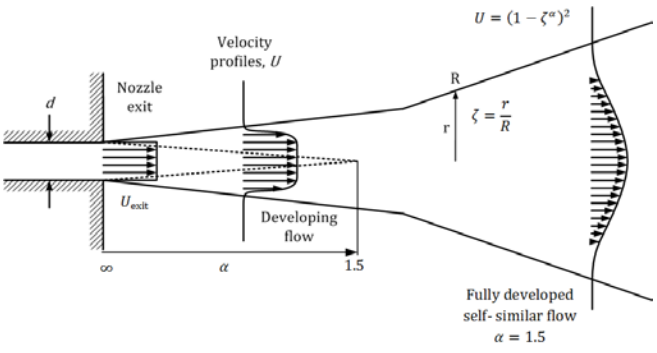

Figure 6: *Classical representation of the early development of a turbulent free jet modified from* **[7]**.

The velocity profile issuing from the orifice is assumed to be uniform. Outside the nozzle, mixing layers grow as ambient gas entrains and mixes with the injectant. This results in a widened velocity profile with softer edges. As the velocity profile develops downstream the exit velocity, U_{exit}, is maintained as the maximum velocity, as indicated by the dashed lines. This region is often referred to as the potential core. The potential core ends where the central maximum velocity starts to decay. Beyond this point the jet is self-similar, meaning that the velocity profile maintains the same shape [7]. Abramovich [8] described the velocity and concentration profiles as Eqs. (7) and (8).

$$\frac{U}{U_c} = (1-\zeta^\alpha)^2 \tag{7}$$

$$\frac{\chi_f}{\chi_{f,c}} = (1-\zeta^\alpha)^2 \tag{8}$$

Where ζ is the dimensionless radius (r/R), U/U_c is the velocity profile normalized by the center axial velocity. The exponent α describes the shape of the velocity profile and is therefore constant in the self-similar part of the jet. For the uniform velocity profile at the nozzle exit, α is ∞.

Musculus and Kattke [9] expanded on the steady-jet development model by Naber and Siebers [10], solving transient transport equations for fuel mass and total jet momentum assuming a non-vaporizing, inviscid, incompressible self-similar jet (assuming the velocity profiles proposed by Abramovich) with a constant dispersion angle. Further simplifications and implications are detailed in [9]. The assumption of a non-vaporizing jet essentially means that the model treats the liquid fuel injection as a variable density gas jet. The model has however been able to predict penetration of vaporizing sprays quite well [10].

The spray model requires the dispersion angle of the jet as an input. α in the transition region is then found using the boundary conditions that the momentum flux is constant and the maximum velocity not exceed the exit velocity. Once a value of $\alpha = 1.5$ the flow is fully developed and the velocity distribution is taken to be self-similar such that α remains constant further downstream.

When an atomized liquid spray is injected into a gaseous environment, the liquid phase can only penetrate a certain distance before the mixing with ambient gases leads to complete evaporation as seen in Figure 7.

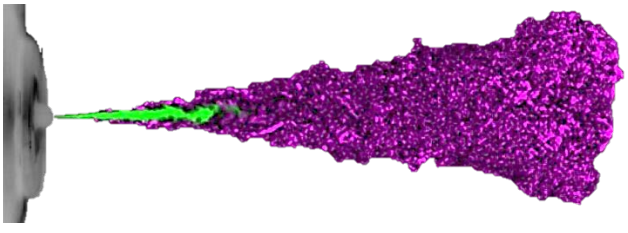

Figure 7: *Superimposed simultaneous snapshots of the liquid (green) and vapor (magenta) phase of a fuel spray injected into a high temperature high pressure environment. The images have been acquired with extinction- and schlieren imaging of the liquid and vapor phase respecively.*

Siebers [11] predicted liquid penetration length of vaporizing fuel spray based on a mixing-limited vaporization assumption. His method can be used to

evaluate the liquid penetration even with the assumption of non-vaporizing jet. Mass and energy conservation leads to Eq. (9) relating the energy required and the energy transferred from the entrained ambient gas to heat and vaporize the fuel at the location, L, of complete vaporization.

$$\frac{\dot{m}_\mathrm{f}(L)}{\dot{m}_\mathrm{a}(L)} = \frac{h_\mathrm{a}(T_\mathrm{amb},p_\mathrm{amb}) - h_\mathrm{a}(T_\mathrm{s},p_\mathrm{amb}-p_\mathrm{s})}{h_\mathrm{f}(T_\mathrm{s}) - h_\mathrm{f}(T_\mathrm{f},p_\mathrm{amb})} \tag{9}$$

Where the subscript amb refers to the ambient gas conditions, f refers to the fuel and s refers to the saturation conditions of the fuel. The difference $p_\mathrm{amb} - p_\mathrm{s}$ is the partial pressure of the ambient gas in the spray. The mass flows at L can be written as Eqs. (10) and (11).

$$\dot{m}_\mathrm{f}(L) = \rho_\mathrm{f}(L) \cdot A(L) \cdot U(L) \tag{10}$$

$$\dot{m}_\mathrm{a}(L) = \rho_\mathrm{a}(L) \cdot A(L) \cdot U(L) \tag{11}$$

This shows that $\dot{m}_\mathrm{f}(L)/\dot{m}_\mathrm{a}(L) = \rho_\mathrm{f}(L)/\rho_\mathrm{a}(L)$ which when inserted into the real gas equation of state yields the equality in Eq. (12).

$$\frac{Z_\mathrm{a}(T_\mathrm{s},p_\mathrm{amb}-p_\mathrm{s})\cdot p_\mathrm{s}\cdot M_\mathrm{f}}{Z_\mathrm{f}(T_\mathrm{s},p_\mathrm{s})\cdot(p_\mathrm{amb}-p_\mathrm{s})\cdot M_\mathrm{a}} = \frac{h_\mathrm{a}(T_\mathrm{amb},p_\mathrm{amb}) - h_\mathrm{a}(T_\mathrm{s},p_\mathrm{amb}-p_\mathrm{s})}{h_\mathrm{f}(T_\mathrm{s}) - h_\mathrm{f}(T_\mathrm{f},p_\mathrm{amb})} \tag{12}$$

The only unknown in Eq. (12) is T_s as in saturated conditions T_s also defines p_s. T_s must be solved iteratively given the fuel and ambient gas properties and their initial conditions. This method is analogous to determining the surface temperature of a vaporizing liquid droplet and the quantity $\dot{m}_\mathrm{f}(L)/\dot{m}_\mathrm{a}(L)$ analogous to the Spalding heat and mass transfer numbers. Siebers further developed Eq. (13) for determining the liquid penetration length

$$L = \frac{b}{a} \cdot \sqrt{\frac{\rho_\mathrm{f}}{\rho_\mathrm{a}}} \cdot \frac{\sqrt{C_\mathrm{a}}\cdot d}{\tan(\theta/2)} \cdot \sqrt{\left(\frac{2}{\dot{m}_\mathrm{f}(L)/\dot{m}_\mathrm{a}(L)} + 1\right)^2 - 1} \tag{13}$$

Where the constants a and b have a value of 0.66 and 0.41 respectively, derived from a best fit of the liquid length based on hexadecane and heptamethylnonane (HMN) measurements. The jet dispersion angle θ is primarily affected by the ambient density and Eq. (13) applies an empirical correlation to account for the ambient density in the form of Eq. (14).

$$\tan\theta/2 = c\left[\left(\rho_a/\rho_f\right)^{0.19} - 0.0043\sqrt{\rho_f/\rho_a}\right] \tag{14}$$

Where the constant c is 0.26. An example of the liquid penetration equations from Siebers [11] showing the effects of ambient density and temperature on the liquid penetration length can be seen in Figure 8.

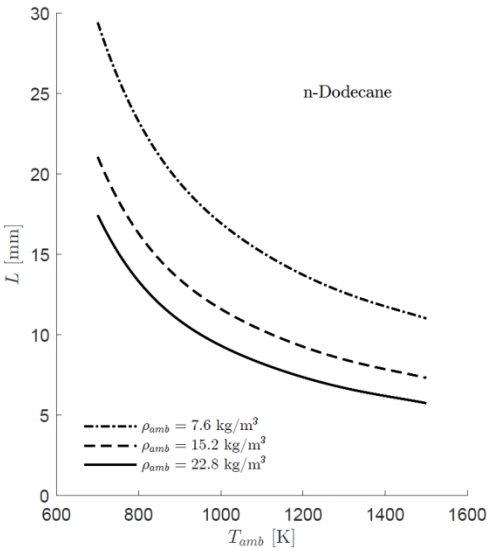

Figure 8: *Liquid penetration length predicted by the model of Siebers at various ambient densities as function of ambient temperature for n-dodecane fuel with* $\boldsymbol{T_f = 363\ K}$ *injected from a nozzle orifice* $\boldsymbol{d = 90\ \mu m}$ *with* $\boldsymbol{C_a = 0.95}$.

The fuel air ratio can be predicted by the jet model through Eq. (15).

$$\frac{F}{A} = \frac{\rho_\mathrm{f}\cdot\chi_\mathrm{f}}{\rho_\mathrm{a}\cdot(1-\chi_\mathrm{f})} \tag{15}$$

Thereby the liquid boundary can be determined by applying the fuel air ratio at L determined with Eq. (12) as a threshold. The model predicts accurately the effects of ambient temperature and density on the liquid penetration length. However, the absolute liquid penetration length is uncertain as it is dependent on the dispersion angle which is typically measured via schlieren imaging of the vapor phase [10]. An demonstration of the model can be seen in Figure 9.

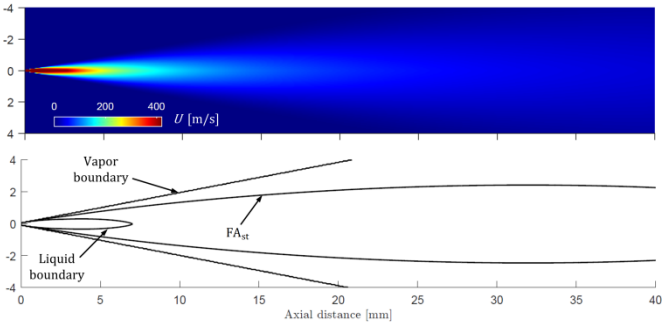

Figure 9: *Output from steady jet model with n-dodecane at* $\boldsymbol{T_f = 363\ K}$ *injected through a nozzle with* $\boldsymbol{d = 90\ \mu m}$, $\boldsymbol{C_d = 0.8}$, $\boldsymbol{C_a = 0.9}$ *into an ambient with* $\boldsymbol{\rho_{amb} = 22.8\ kg/m^3}$ *and* $\boldsymbol{T_{amb} = 900\ K}$. *The dispersion angle is taken to be* $\boldsymbol{21.5°}$ *full angle and constant. The velocity distribution (above) and contour of fuel air ratio are shown with liquid, vapor and stoichiometric boundaries indicated.*

Investigations have however found that a narrower dispersion angle of the jet is needed as an input to the model in order to match the predicted liquid length to measurements [12,9]. This transition from a narrow dispersion angle at the nozzle exit has been observed in actual measurements as well [13,14]. This phenomena is

also the reason for the constants a, b and c in Siebers's liquid scaling equations in order to match with experiments. Amielh et. al. [15] found that a turbulent gas jet with higher ρ_f/ρ_a lengthened the potential core, reduced the axial velocity decay and led to slower mixing. As the model treats the jet as a variable density gas jet, the details of liquid break-up and evaporation must be the cause for the deviation of the model from reality. The author speculates that the findings of Amielh et. al. [15] are enhanced in two phase jets due to the local high density in the break-up and evaporation zone. The length of the transition zone, and consequently the rest of the flame, is then governed by the break-up and vaporization process. If this is the case, a longer liquid penetration will lead to a longer transition region with a narrow dispersion angle and poor mixing before the spray evaporates and mixes sufficiently with the ambient. It is therefore beneficial to have as short a liquid length as possible in the. Pickett et. al. [12] found that the transition region with narrow dispersion angle became shorter with higher ambient density. For our case of a stationary spray flame at atmospheric pressure, factors reducing the liquid penetration length are important.

The vaporization process is dependent upon the break-up process and the properties of the fuel. An important fuel property is its volatility. The fuel is pressurized and is injected into an ambient with lower pressure. If the initial temperature of the fuel is above its boiling temperature at the ambient pressure, flash boiling will occur. For these conditions Eq. (12) is ill defined as the specific enthalpy difference in the denominator becomes negative due to $T_f > T_s$ and the fuel is in gaseous state at T_f and p_{amb}. Under these circumstances Eq. (12) can be modified to Eq. (16).

$$\frac{\dot{m}_f(L)}{\dot{m}_a(L)} = \frac{h_a(T_{amb},p_{amb}) - h_a(T_s,p_{amb}-p_s)}{h_f(T_s) - h_f(T_f,q=0)} \qquad (16)$$

The saturation temperature for the selected fuels can be seen in Figure 10 as function of the partial pressure of the fuel.

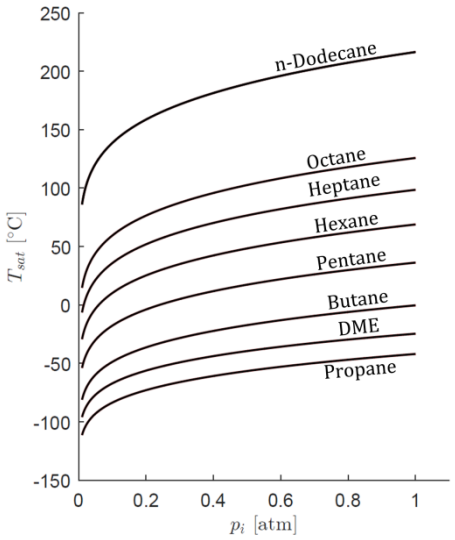

Figure 10: *Saturation temperature, T_{sat}, of the selected fuels as function of the partial pressure, p_i.*

Most of the fuels will be under flash boiling conditions when injected into atmospheric ambient and that propane has the lowest saturation temperature and thus evaporates fastest.

Eq. (16), using Newton Raphson iteration incorporating the NIST standard reference database, has been used together with the spray model in order to evaluate the effect of fuel volatility on the liquid penetration length. The fuel is injected into an ambient with atmospheric pressure. The ambient temperature can be however be adjusted with a co-annular hydrogen flat flame. This flame will also be able to adjust the oxygen content in the ambient gases, simulating EGR. The lack of knowledge of the resulting dispersion angle from such a spray means that only the relative effect of the fuel volatility can be evaluated. A constant dispersion angle of 15° full angle has been input to the model. Orifice diameters of 50 μm and 30μm have been evaluated.

The effect of the fuel volatility, orifice diameter and ambient temperature can be seen in Figure 11.

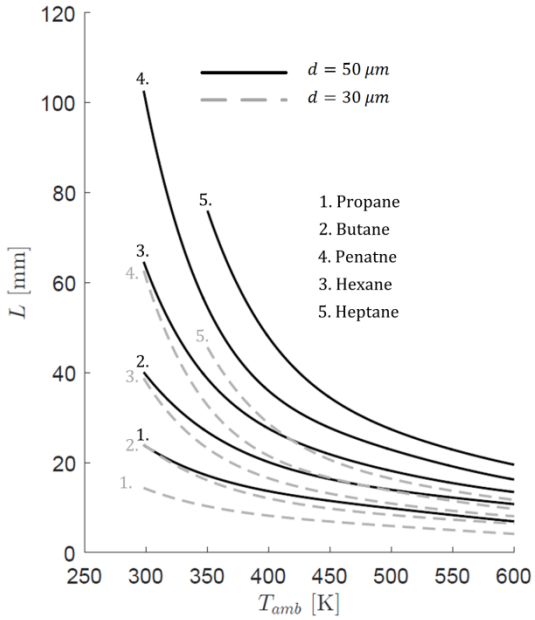

Figure 11: *Liquid penetration length for a range of fuels with varying volatility evaluated with the spray model with Eq. (16) incorporated. The effect of ambient temperature and orifice diameter is also shown.*

It can be seen that the fuel volatility has a major effect under low ambient temperature. At high ambient temperatures the effect of fuel volatility are quite small. A higher ambient density would also reduce the effect. The effect of fuel volatility is then not important at high ambient temperature and pressure as concluded by Kook et. al. [16]. At atmospheric conditions however, the effects of fuel volatility are large. Propane is the fuel with the lowest boiling temperature and thus has the shortest liquid penetration length. Propane was also the easiest fuel to atomize. Propane is then the clear choice of fuel for the atmospheric stationary spray flame due to its low kinematic viscosity and low boiling temperature. The orifice diameter should be as small as possible, preferably not larger than 50 μm.

Conclusion

An investigation of the various parameters governing fuel atomization and the resulting spray/jet has been performed. The investigation has the goal of dimensioning a stationary diesel-like fuel spray at atmospheric conditions. It has been found that the kinematic viscosity and orifice diameter are the most influential parameters governing the break-up of the fuel. A small orifice and low kinematic viscosity promote atomization with the requirement of low mass flow rate. The resulting fuel spray/jet is influenced by the break-up and vaporization of the fuel, extending the liquid phase of the spray, thus resulting in a very long spray. The fuel volatility is a key property reducing the liquid penetration length under low ambient pressure and temperature. It was found that the orifice diameter should be $< 50\ \mu m$ and that the most suitable fuel in all aspects was propane.

Works Cited

[1] Ohnesorge, W. "Die bildung von tropfen an Düsen und die auflösung flüssinger strahlen." *Zeitschift für angewandte Mathematik und Mechanik* 16, no. 6 (1931): 355-358.

[2] Baumgarten, C. *Mixture formation in internal combustion engines.* Springer Berlin Heidelberg, 2006.

[3] Faeth, G. M., Hsiang, L. P., and Wu, P. K. "Structure and breakup properties pf sprays." *Int. J. Multiphase Flow* 21 (1995): 99-127.

[4] Ivarsson, A & Schramm, J. *Modeling of heat release and emissions from droplet combustion of multi component fuels in compression ignition engines.* Ph. D. thesis, Kgs. Lyngby, Denmark: Technical University of Denmark (DTU), 2010, 111.

[5] Lemmon, E. W., Huber, M. L., McLinden, M. O. "NIST Standard Reference Database 23: Reference Fluid Thermodynamic and Transport Properties-REFPROP, Version 9.1." 2013.

[6] Payri, R., Garcia, J. M., Salvador, F. J., and Gimeno, J. "Using Spray Momentum Flux Measurements to Understand the Influence of Diesel Nozzle Geometry on Spray Characteristics." *Fuel* 80 (2005): 551-561.

[7] White, F. M. *Viscous fluid flow.* 3. New York: Mcgraw Hill, 2006.

[8] Abramovich, G. N. *The theory of turbulent jets.* Cambridge: M. I. T. Press, 1963.

[9] Musculus, M. P. B., and Kattke, K. "Entrainment waves in diesel jets." *SAE Int.J.Engines 2009-01-1355* 2, no. 1 (2009): 1170-1193.

[10] Naber, J. D., and Siebers, D. L. "Effects of Gas Density and Vaporization on Penetration and Dispersion of Diesel Sprays." *SAE Technical Paper 960034*, 1996.

[11] Siebers, D. L. "Scaling Liquid-Phase Fuel Penetration in Diesel based on mixing-limited vaporization." *SAE Technical Paper 1999-01-0528*, 1999.

[12] Pickett, L. M., Siebers, D., and Idicheria, C. "Relationship Between Ignition Processes and Lift-Off Length of Diesel Fuel Jets." *SAE Technical Paper 2005-01-3843*, 2005.

[13] Kastengren, A. L., Powell, C. F., Wang, Y. J., Im, K. S. and Wang, J. "X-ray radiography measurements of diesel spray structure at engine-like ambient density." *Atomization and Sprays* 19 (2009): 1031-1044.

[14] Westlye, F. R., Battistoni, M., Skeen, S., Manin, J., Pickett, L. M. "Penetration and combustion characterization of cavitating and non-cavitating fuel injectors under diesel engine conditions." *SAE Technical Paper 2016-01-0860*, 2016.

[15] Amielh, M., Djeridane, T., Anselmet and Fulachier. "Velocity near-field of variable density turbulent jets." *Journal of Heat and Mass Transfer* 39, no. 10 (1996): 2149-2164.

[16] Kook, S. and Pickett, L. M. "Liquid length and vapor penetration of conventional, Fischer-Tropsch, coal-derived, and surrogate fuel sprays at high-pressure ambient conditions." *Fuel* 93 (2012): 539-548.

Publications

SAE INTERNATIONAL®

Penetration and Combustion Characterization of Cavitating and Non-Cavitating Fuel Injectors under Diesel Engine Conditions

2016-01-0860
Published 04/05/2016

Fredrik R. Westlye
Technical University of Denmark

Michele Battistoni
Universita degli Studi di Perugia

Scott A. Skeen, Julien Manin, and Lyle M. Pickett
Sandia National Laboratories

Anders Ivarsson
Technical University of Denmark

CITATION: Westlye, F., Battistoni, M., Skeen, S., Manin, J. et al., "Penetration and Combustion Characterization of Cavitating and Non-Cavitating Fuel Injectors under Diesel Engine Conditions," SAE Technical Paper 2016-01-0860, 2016, doi:10.4271/2016-01-0860.

Abstract

This work investigates the effects of cavitation on spray characteristics by comparing measurements of liquid and vapor penetration as well as ignition delay and lift-off length. A smoothed-inlet, converging nozzle (nominal KS1.5) was compared to a sharp-edged nozzle (nominal K0) in a constant-volume combustion vessel under thermodynamic conditions consistent with modern compression ignition engines. Within the near-nozzle region, the K0 nozzle displayed larger radial dispersion of the liquid as compared to the KS1.5 nozzle, and shorter axial liquid penetration. Moving downstream, the KS1.5 jet growth rate increased, eventually reaching a growth rate similar to the K0 nozzle while maintaining a smaller radial width. The increasing spreading angle in the far field creates a virtual origin, or mixing offset, several millimeters downstream for the KS1.5 nozzle. Remarkably, this mixing offset appeared to globally influence the liquid penetration and lift-off stabilization location over a wide range of operating conditions. When this offset was removed, OH chemiluminescence-derived lift-off lengths for the two nozzles essentially collapsed. An Eulerian multiphase mixture model, with Large-Eddy Simulations (LES) combining internal and external flow predicted the trends in spreading angle in the region close to the injector. The K0 simulation showed cavitation zones along walls downstream of the nozzle inlet with some dispersion into the center of the jet before the nozzle exit. With a slightly diverging nozzle (as measured), the K0 simulation also indicated that low pressure zones draw ambient gas just inside the nozzle exit, which, combined with cavitation dynamics, should be considered as a potential contributor to the initial growth rate.

Diffuse back-illumination setup for high temporally resolved extinction imaging

FREDRIK R. WESTLYE[1,*], KEITH PENNEY[2], ANDERS IVARSSON[1], SCOTT SKEEN[2], JULIEN MANIN[2], AND LYLE PICKETT[2]

[1]*Department of Mechanical Engineering, Technical University of Denmark, Nils Koppels Allé Bld. 403, 2800 Kgs. Lyngby*
[2]*Sandia National Laboratories, P.O. Box 969, Livermore, CA 94550, USA*
**Corresponding author: frrwe@mek.dtu.dk*

To be submitted to Journal of applied Optics

An optical setup has been developed for quantitative line of sight extinction imaging with high temporal resolution capabilities. It has been specifically optimized to detect attenuation by absorption/scattering and minimize perceived attenuation caused by refractive gradients along the optical path. The design criteria have been determined from a theoretical stand point. A conceptual description of refractive steering occurrences and the lighting criteria needed to eliminate their effect on light collection has been demonstrated using simple ray tracing. These criteria are used to optimize the optical system with regards to light throughput in order to achieve high temporal resolution capabilities. The setup uses an engineered diffuser to transmit a constant radiance within a limited angular range in order to maximize the radiant intensity while fulfilling the lighting criteria for optimal beam-steering suppression. Methods of which to completely characterize the optical system are detailed. The application is specifically aimed at extinction imaging of automotive fuel sprays in high ambient temperature and pressure environments relevant to modern compression ignition engines. The current optical setup effectively reduces the attenuation caused by refractive index gradients by an order of magnitude compared to previous setups. This yields improved contrast for more accurate determination of liquid-vapor boundaries and reduces uncertainties in determining the soot volume fraction.

OCIS codes: *(110.0113) Imaging through turbid media, (110.0115) Imaging through turbulent media, (350.4990) Particles.*

http://dx.doi.org/10.1364/AO.99.09999

2016-01-0734
Published 04/05/2016

doi:10.4271/2016-01-0734
saeeng.saejournals.org

A Progress Review on Soot Experiments and Modeling in the Engine Combustion Network (ECN)

Scott A. Skeen, Julien Manin, and Lyle M. Pickett
Sandia National Laboratories

Emre Cenker
King Abdullah University of Science and Technology

Gilles Bruneaux
IFPEN

Katsufumi Kondo and Tets Aizawa
Meiji University

Fredrik Westlye, Kristine Dalen, and Anders Ivarsson
Technical University of Denmark

Tiemin Xuan and Jose M Garcia-Oliver
Universitat Politecnica de Valencia

Yuanjiang Pei and Sibendu Som
Argonne National Laboratory

Wang Hu and Rolf D. Reitz
University of Wisconsin

Tommaso Lucchini and Gianluca D'Errico
Politecnico di Milano

Daniele Farrace, Sushant S. Pandurangi, and Yuri M. Wright
ETH Zurich

Muhammad Aqib Chishty, Michele Bolla, and Evatt Hawkes
University of New South Wales

ABSTRACT

The 4th Workshop of the Engine Combustion Network (ECN) was held September 5-6, 2015 in Kyoto, Japan. This manuscript presents a summary of the progress in experiments and modeling among ECN contributors leading to a better understanding of soot formation under the ECN “Spray A” configuration and some parametric variants. Relevant published and unpublished work from prior ECN workshops is reviewed. Experiments measuring soot particle size and morphology, soot volume fraction (f_v), and transient soot mass have been conducted at various international institutions providing target data for improvements to computational models. Multiple modeling contributions using both the Reynolds Averaged Navier-Stokes (RANS) Equations approach and the Large-Eddy Simulation (LES) approach have been submitted. Among these, various chemical mechanisms, soot models, and turbulence-chemistry interaction (TCI) methodologies have been considered.

CITATION: Skeen, S., Manin, J., Pickett, L., Cenker, E. et al., "A Progress Review on Soot Experiments and Modeling in the Engine Combustion Network (ECN)," *SAE Int. J. Engines* 9(2):2016, doi:10.4271/2016-01-0734.